High-performance integrated photonics with amorphous silicon carbide

Lopez Rodriguez, B.

DOI
10.4233/uuid:6323b810-0baa-4e2c-8a72-e26137ddc35d

Publication date
2025

Document Version
Final published version

Citation (APA)
Lopez Rodriguez, B. (2025). *High-performance integrated photonics with amorphous silicon carbide*. [Dissertation (TU Delft), Delft University of Technology]. https://doi.org/10.4233/uuid:6323b810-0baa-4e2c-8a72-e26137ddc35d

Important note
To cite this publication, please use the final published version (if applicable).
Please check the document version above.

High-performance integrated photonics with amorphous silicon carbide

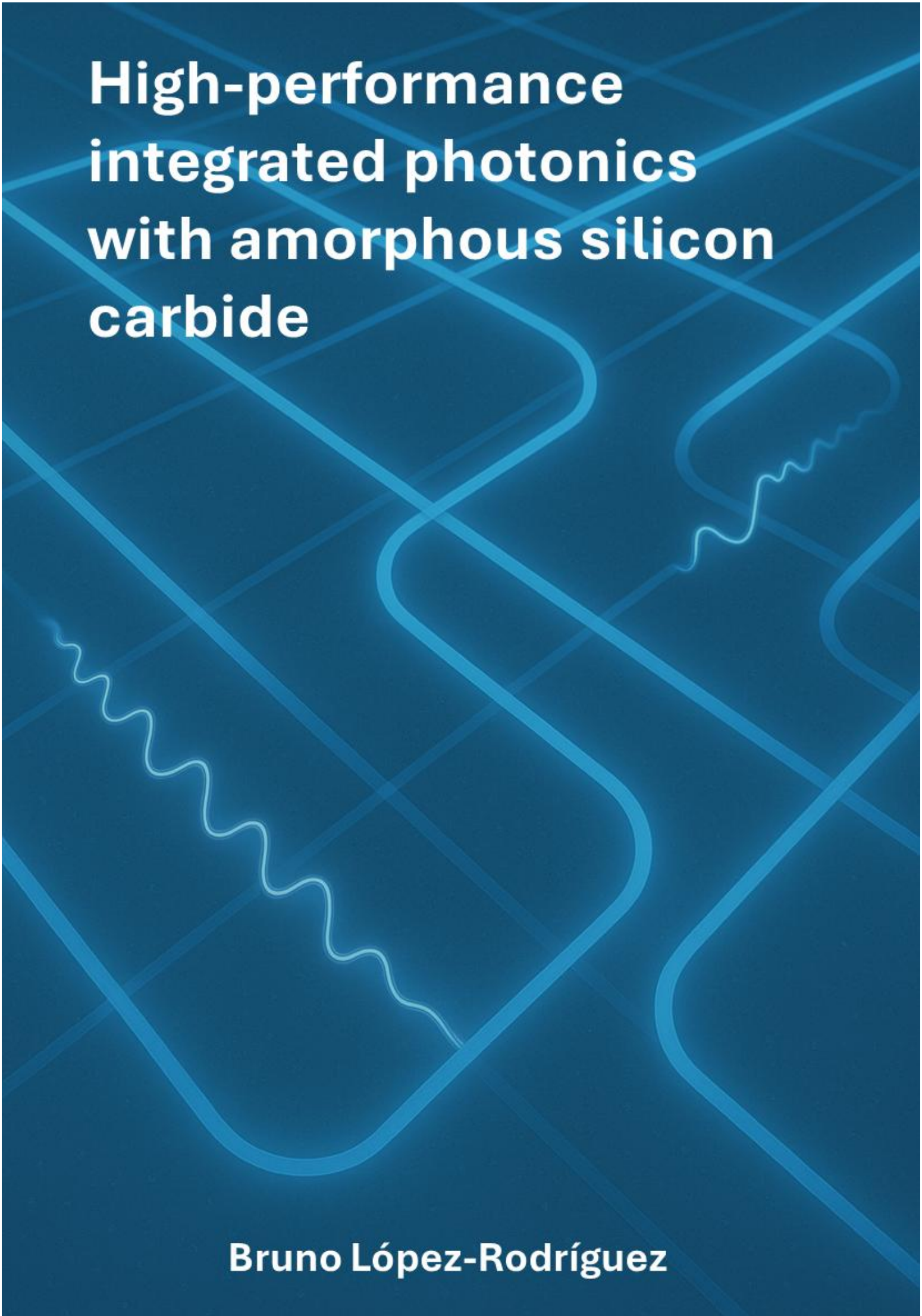

Bruno López-Rodríguez

High-Performance Integrated Photonics With Amorphous Silicon Carbide

HIGH-PERFORMANCE INTEGRATED PHOTONICS WITH AMORPHOUS SILICON CARBIDE

Dissertation

for the purpose of obtaining the degree of doctor
at Delft University of Technology
by the authority of the Rector Magnificus, prof. dr. ir. T.H.J.J. van der Hagen,
chair of the Board for Doctorates
to be defended publicly on
5th of December 2025 at 10:00 am

Bruno LOPEZ-RODRIGUEZ

Master in Nanotechnology at KTH Royal Institute of Technology in Stockholm, Sweden
born in Madrid, Spain

This dissertation has been approved by the promotors.

Composition of the doctoral committee:

Rector Magnificus,	chairperson
Dr.ir. S. F. Pereira	Delft University of Technology, *promotor*
Dr. I. Esmaeil Zadeh	Delft University of Technology, *copromotor*
Independent members:	
Prof. dr. P. Steeneken	Delft University of Technology
Dr. A. W. Elshaari	KTH Royal Institute of Technology, Sweden
Dr. Q. Cheng	University of Cambridge, United Kingdom
Prof. dr. P.W.H. Pinkse	University of Twente, the Netherlands
Dr. M. Versteegh	De Haagse Hogeschool, the Netherlands
Reserve member:	
Prof.dr. Stefan Witte	Delft University of Technology, the Netherlands

Printed by: Ridderprint B.V

ISBN 978-94-6518-156-1

An electronic copy of this dissertation is available at
https://repository.tudelft.nl/.

A mis padres, Ana y Arturo, mi hermana Paula y el resto de mi familia

Bruno Lopez-Rodriguez

CONTENTS

ABBREVIATIONS

PIC	Photonic Integrated Circuit
CMOS	Complementary Metal-Oxide Semiconductor
SiC	Silicon Carbide
SiCOI	Silicon Carbide On Insulator
a-SiC	Amorphous Silicon Carbide
CVD	Chemical Vapor Deposition
PECVD	Plasma-Enhanced CVD
ICPCVD	Inductively-Coupled Plasma-Enhanced CVD
FWHM	Full-Width at Half-Maximum
TOC	Thermo-optic Coefficient
RIU	Refractive Index Units
LN	Lithium Niobate, $LiNbO_3$
LNOI	Lithium Niobate on Insulator
SNSPD	Superconducting Nanowire Single Photon Detector
SOI	Silicon-on-Insulator
MMI	Multi-mode Interferometer
MZI	Mach-Zehnder Interferometer
MEMS	Micro-electro-mechanical systems
QKD	Quantum Key Distribution
LIDAR	Light Detection and Ranging
OPA	Optical Phase Array
FMCW	Frequency Modulated Continuous Wave
FWM	Four-Wave Mixing
RIE	Reactive Ion Etching

PCB	Printed Circuit Board
SMP	Subminiature push-on
RF	Radio-Frequency
DC	Direct Current
GUI	Guided User Interface
CCD	Charge-Coupled Device
LED	Light Emitting Diode
SMA	Subminiature version A
BNC	Bayonet Neill-Concelman
CROW	Coupled Ring Optical Waveguide
AFM	Atomic Force Microscopy
SEM	Scanning Electron Microscopy
TFLN	Thin-film Lithium Niobate
FSR	Free Spectral Range

SUMMARY

Over the past decades, integrated photonic circuits have revolutionized the field of optics by enabling on-chip generation, manipulation, and detection of light with unprecedented scalability and precision. By leveraging advances in material platforms and nanofabrication tools and techniques, integrated photonics supports an ever-expanding range of applications, from high-speed optical communications and on-chip sensing to photonic quantum computing and signal processing. In this work, we showcase fundamental device designs and advanced nanofabrication techniques to improve their performance. We also address critical challenges—such as integrating active components, managing losses, and achieving high thermal tunability and discuss future directions for ultra-compact, energy-efficient, and multifunctional integrated photonic devices.

As a start, **chapter 2** treats the conventionally used material platforms for integrated photonics, emphasizing their advantages and drawbacks, including fundamental building blocks for integrated photonic circuits, tuning mechanisms to achieve reconfigurability in integrated photonics, combination with superconducting nanowire single photon detectors and applications of integrated photonic circuits.

Chapter 3 demonstrates how these devices are fabricated using advanced nanofabrication tools and techniques, and shows the optical setups that are needed to be build to characterize them, both at room temperature and at cryogenics.

To optimize the material platform, **chapter 4** explores the current chemical vapor deposition (CVD) techniques for a-SiC, emphasizing the use of more advanced tools to improve the thin film quality for the use in the fabrication of optical devices with low waveguide propagation losses. Using inductively-coupled plasma enhanced CVD (ICPCVD), We achieved three times lower propagation losses (0.78 dB/cm) than the current state-of-the-art (3 dB/cm) at half the deposition temperature (150°C) and provided a route to do hybrid integration with the silicon nitride platform.

To further enhance these devices, **chapter 5** highlights, using the ICPCVD technique with silicon dioxide claddings the tuning of the thermo-optic thermal shift in ring resonators. We demonstrate up to a tenfold improvement in the thermal tunability, athermal devices and bidirectional thermal tunability on amorphous silicon carbide, silicon nitride and silicon-on-insulator.

Based on the previous demonstrations, **chapter 6** demonstrates the integration of this material platform with superconducting nanowire single photon detectors for quantum photonic applications.

To finalize this dissertation, **chapter 7** overviews three main collaborations done during the project related to hybrid photonics of a-SiC with polymers, lithium niobate and silicon nitride photonic platforms and summarizes the main results of the thesis, reflecting on current challenges and future opportunities using this platform.

SAMENVATTING

In de afgelopen decennia hebben geïntegreerde fotonische circuits het vakgebied van de optica getransformeerd door het mogelijk te maken om licht op een chip te genereren, manipuleren en detecteren met ongekende schaalbaarheid en precisie. Door gebruik te maken van vooruitgang in materiaalsystemen en nanofabricagetechnieken ondersteunt geïntegreerde fotonica een steeds breder scala aan toepassingen, van snelle optische communicatie en on-chip sensing tot fotonische kwantumcomputing en signaalverwerking. In dit werk tonen we fundamentele apparaatontwerpen en geavanceerde nanofabricagetechnieken om hun prestaties te verbeteren. We bespreken ook kritieke uitdagingen—zoals het integreren van actieve componenten, het beheersen van verliezen en het bereiken van hoge thermische afstembaarheid—en bespreken toekomstige richtingen voor ultracompacte, energie-efficiënte en multifunctionele geïntegreerde fotonische apparaten.

Als begin behandelt **hoofdstuk 2** de conventioneel gebruikte materiaalsystemen voor geïntegreerde fotonica, met nadruk op hun voordelen en nadelen, inclusief fundamentele bouwstenen voor geïntegreerde fotonische circuits, afstemmechanismen om herconfigureerbaarheid te bereiken in geïntegreerde fotonica, combinaties met supergeleidende nanodraad enkel-foton detectoren en toepassingen van geïntegreerde fotonische circuits.

Hoofdstuk 3 toont hoe deze apparaten worden vervaardigd met behulp van geavanceerde nanofabricagetools en -technieken, en laat de optische opstellingen zien die nodig zijn om ze te karakteriseren, zowel bij kamertemperatuur als bij cryogene temperaturen.

Om het materiaalsysteem te optimaliseren verkent **hoofdstuk 4** de huidige technieken voor chemische dampafzetting (CVD) voor a-SiC, met nadruk op het gebruik van meer geavanceerde tools om de dunnefilmkwaliteit te verbeteren voor de fabricage van optische apparaten met lage golfgeleiderverliezen. Met behulp van inductief gekoppelde plasma-geactiveerde CVD (ICPCVD) bereikten we drie keer lagere voortplantingsverliezen (0,78 dB/cm) dan de huidige stand van de techniek (3 dB/cm) bij de helft van de afzettemperatuur (150°C) en boden we een route aan voor hybride integratie met het silicium-nitrideplatform.

Om deze apparaten verder te verbeteren benadrukt **hoofdstuk 5**, met gebruik van de ICPCVD-techniek en siliciumdioxide claddings, het afstemmen van de thermo-optische verschuiving in ringresonatoren. We tonen tot een tienvoudige verbetering in thermische afstembaarheid, athermische apparaten en bidirectionele thermische afstembaarheid aan in amorf siliciumcarbide, silicium-nitride en silicon-on-insulator.

Op basis van de voorgaande demonstraties toont **hoofdstuk 6** de integratie van dit materiaalsysteem met supergeleidende nanodraad enkel-foton detectoren voor kwantumfotonische toepassingen.

Ter afronding van dit proefschrift geeft **hoofdstuk 7** een overzicht van drie belangrijke samenwerkingen tijdens het project, gerelateerd aan hybride fotonica van a-SiC met polymeren, lithiumniobaat en silicium-nitride fotonische platformen, en vat het de belangrijkste resultaten van het proefschrift samen, waarbij wordt gereflecteerd op de huidige uitdagingen en toekomstige mogelijkheden met dit platform.

RESUMEN

Durante las últimas décadas, los circuitos fotónicos integrados han revolucionado el campo de la óptica al permitir la generación, manipulación y detección de luz en chip con una escalabilidad y precisión sin precedentes. Aprovechando los avances en plataformas de materiales y herramientas y técnicas de nanofabricación, la fotónica integrada respalda una gama cada vez mayor de aplicaciones, desde comunicaciones ópticas de alta velocidad y sensores integrados hasta computación cuántica fotónica y procesamiento de señales. En este trabajo, mostramos diseños fundamentales de dispositivos y técnicas avanzadas de nanofabricación para mejorar su rendimiento. También abordamos desafíos críticos—como la integración de componentes activos, la gestión de pérdidas y la obtención de alta sintonización térmica—y discutimos las futuras direcciones hacia dispositivos fotónicos integrados ultracompactos, energéticamente eficientes y multifuncionales.

Como inicio, el **capítulo 2** trata las plataformas de materiales comúnmente utilizadas en fotónica integrada, haciendo énfasis en sus ventajas y desventajas, incluyendo bloques de construcción fundamentales para circuitos fotónicos integrados, mecanismos de sintonización para lograr reconfigurabilidad, la combinación con detectores superconductores de un solo fotón basados en nanohilos, y aplicaciones de los circuitos fotónicos integrados.

El **capítulo 3** demuestra cómo se fabrican estos dispositivos utilizando herramientas y técnicas avanzadas de nanofabricación, y muestra los montajes ópticos necesarios para caracterizarlos, tanto a temperatura ambiente como a temperaturas criogénicas.

Para optimizar la plataforma de materiales, el **capítulo 4** explora las técnicas actuales de deposición química de vapor (CVD) para a-SiC, destacando el uso de herramientas más avanzadas para mejorar la calidad de la película delgada en la fabricación de dispositivos ópticos con bajas pérdidas de propagación en la guía de onda. Usando CVD mejorado con plasma inductivamente acoplado (ICPCVD), logramos pérdidas de propagación tres veces menores (0.78 dB/cm) que el estado del arte actual (3 dB/cm) a la mitad de la temperatura de deposición (150°C), y proporcionamos una vía para la integración híbrida con la plataforma de nitruro de silicio.

Para mejorar aún más estos dispositivos, el **capítulo 5** destaca, utilizando la técnica ICPCVD con recubrimientos de dióxido de silicio, el ajuste del desplazamiento termoóptico en resonadores de anillo. Demostramos hasta una mejora de diez veces en la sintonización térmica, dispositivos atérmicos y sintonización térmica bidireccional en silicio carburo amorfo, nitruro de silicio y silicio sobre aislante.

Basado en las demostraciones anteriores, el **capítulo 6** muestra la integración de esta plataforma de materiales con detectores superconductores de un solo fotón basados en nanohilos para aplicaciones fotónicas cuánticas.

Para finalizar esta disertación, el **capítulo 7** presenta una visión general de tres colaboraciones principales realizadas durante el proyecto, relacionadas con la fotónica

híbrida de a-SiC con polímeros, niobato de litio y plataformas fotónicas de nitruro de silicio, y resume los principales resultados de la tesis, reflexionando sobre los desafíos actuales y las oportunidades futuras utilizando esta plataforma.

1

INTRODUCTION

Bruno LOPEZ-RODRIGUEZ

The world as we have created it is a process of our thinking. It cannot be changed without changing our thinking.

Albert Einstein

1

1.1. FROM BULK TO A SINGLE CHIP

In the era of the digital revolution, where global data consumption and the demand for ultra-high-speed communication are increasing, the limitations of conventional electronic systems are becoming clear. The quest for faster, more efficient, and scalable technologies has placed photonics at the forefront to surpass the boundaries of traditional electronics. Integrated photonics emerges as a transformative solution, integrating optical components such as lasers, modulators, and waveguides onto compact, chip-scale platforms. This evolution is comparable to the development of electronic integrated circuits, promising to revolutionize industries by enabling dense, low-power, and high-performance photonic systems.

Traditional optics and photonic setups rely on discrete bulk elements (mirrors, lenses, beamsplitter crystal blocks, ...) and present evident problems in scalability, cost, and robustness, hindering their deployment in next-generation applications [1]. Integrated photonics addresses these issues by enabling complex optical functions onto single substrates, making use of advanced fabrication techniques to achieve miniaturization and mass production. The implications are profound and cover many application fields such as telecommunications, where photonic integrated circuits (PICs) enhance fiber-optic networks, data centers and artificial intelligence [2–4]; biomedical sensing, enabling portable diagnostic devices [5–7]; and quantum technologies, where precise light control is critical [8]. Furthermore, the synergy of photonics with electronics opens avenues for hybrid systems, combining the computational power of current computers with fast and high bandwidth optical data transfer.

Despite its promise, the field has some challenges. Efficient light manipulation demands innovative waveguide architectures and materials compatible with existing complementary metal-oxide-semiconductor (CMOS) fabrication processes. On the other hand, nonlinear effects, waveguide propagation losses, and reduced coupling efficiencies between components require novel design strategies.

1.2. HYBRID PHOTONICS

Hybrid photonic systems rely on the synergy of different materials used in integrated photonics such as silicon, III-V semiconductors, polymers, and two-dimensional materials, combining their specific advantages to overcome the inherent limitations of monolithic designs [9, 10]. By integrating components like high-efficiency III-V lasers with low-loss silicon nitride waveguides or coupling nonlinear optical polymers to silicon photonic circuits, these systems exploit the unique optical, electronic, and mechanical properties of each material to achieve functionalities that would be unachievable within a single substrate. Such architectures enable enhanced light-matter interactions, improved tuning, and extended operational bandwidths, critical for applications ranging from ultra-dense optical interconnects in data centers to chip-scale quantum light sources. However, the realization of hybrid systems demands innovative solutions for material compatibility, material interface engineering, and scalable fabrication, as mismatches in lattice constants, thermal expansion coefficients, and matching of optical mode profiles pose significant challenges. Recent advances in heterogeneous integration techniques, such as transfer printing, wafer bonding, and selective epitaxial growth,

have enabled precise alignment and robust coupling between components, paving the way for next-generation devices [11–14].

1.3. MOTIVATION OF THE THESIS

With the diverse range of materials available in the integrated photonics landscape, it is challenging to choose a specific platform. However, in this thesis, I aim to convince the reader that amorphous silicon carbide (a-SiC), with further advancements, has the potential to be a game changer in integrated photonics.

Silicon carbide (SiC) exists in numerous crystalline forms, known as polytypes, though only a few are commonly used for integrated photonic devices, primarily 4H-SiC (hexagonal) and 3C-SiC (cubic) (see fig.1.1a). The state-of-the-art developments in photonic devices made on this platform will be discussed in **Chapter 2**, but a key advantage is their ability to achieve low optical losses and support various nonlinear photonic applications. However, they come with a significant drawback: to be optically compatible, they require transfer bonding, a process that is time-consuming, expensive and imprecise in controlling layer thickness (as depicted in fig.1.1b). Furthermore, integrating crystalline SiC (c-SiC) with other materials for heterogeneous photonic systems poses additional challenges. The processing temperatures needed during annealing and chemical interactions between the different materials lead to compatibility issues. Another limitation of crystalline SiC is the difficulty in tailoring its intrinsic properties such as refractive index and composition during crystal growth.

In contrast, a-SiC overcomes these challenges by offering fabrication flexibility. Unlike its crystalline counterpart, a-SiC can be deposited using chemical vapor deposition (CVD) techniques at relatively low temperatures (<300°C) and with tunable composition, allowing seamless integration with standard CMOS processes. The technique explored in this thesis, Inductively Coupled Plasma-Enhanced CVD (ICPCVD), enables the deposition of a-SiC at just 150°C. Therefore, significantly expanding the range of materials compatible with a-SiC without thermal degradation, paving the way for broader adoption in integrated photonic technologies.

Reducing power consumption in photonic devices is critical, especially as integrated photonics becomes part of more demanding applications. This thesis also tackles the problem of achieving highly efficient, low-power thermo-optic tuning in PICs. The amount of thermo-optic tuning that one can achieve is intrinsic to the material platform and unless the composition is altered, it cannot be easily tuned. We address this issue by engineering the silicon dioxide cladding, with a low refractive index and the most common material in photonics. It is the first demonstration that this material can modify the thermo-optic tunability with athermal, positive and negative thermo-optic responses that can be implemented deterministically on a single chip. Consequently, it also addresses biosensing applications and enables novel photonic architectures.

1

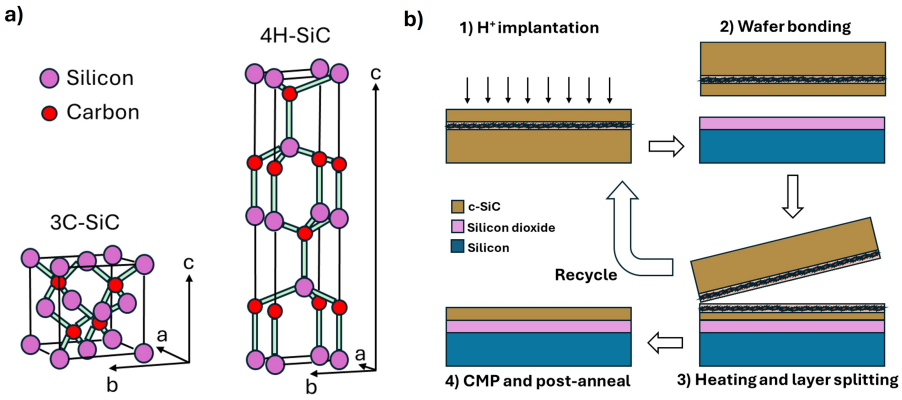

Figure 1.1: a) Crystalline structure of the most common polytypes of silicon carbide, with cubic or hexagonal arrangement of the lattice (reproduced with permission from Henan Superior Abrasives) and b) transfer bonding process flow to achieve crystalline silicon carbide on insulator (reproduced with permission from Elsevier [15]).

1.4. UNDERSTANDING A PHOTONIC DEVICE

To understand the chapters that follow, we will briefly introduce some important parameters in photonic platforms and that are used to characterize optical devices. These terms span linear optics (refractive index, propagation losses), resonant systems (Q factor), thermal effects (thermo-optic coefficient), and nonlinear phenomena (second-order and third-order), each playing key roles in photonic device design and functionality and in this entire thesis.

- **Refractive index (n):** is a dimensionless number that indicates how much light slows down and refracts in the interface between a material and vacuum. In optical devices, a higher refractive index is preferred since it enhances the optical confinement and reduces the bending losses, increasing the integration density.

- **Quality factor (Q):** is a measure of the energy storage efficiency in resonant systems. For optical devices, higher quality factors are associated to narrower filtering and lower propagation losses of the platform. In the literature, the loaded quality factor is usually given as the ratio of the resonant wavelength (λ) and the full-width at half maximum (FWHM). Intrinsic quality factors indicate the inherent material properties of the platform without considering the device geometry. These parameters are related to each other in the equation below, where T_b is the normalized transmission factor in the bus waveguide.

$$Q_{loaded} = \frac{\lambda}{FWHM} \qquad Q_{intrinsic} = \frac{2Q_{loaded}}{1+\sqrt{T_b}} \tag{1.1}$$

- **Waveguide propagation losses:** measured in dB/cm, represents the attenuation of light as it travels through a waveguide. Propagation losses are usually caused by material absorption, scattering due to sidewall roughness or bending losses. The losses can be estimated from the intrinsic quality factors using the relations below where the group index (n_g) is determined from the free spectral range (FSR) (separation between adjacent resonant dips) as is discussed in **Chapter 4**:

$$\alpha(cm^{-1}) = \frac{2\pi n_g}{Q_{int}\lambda} \quad ; \quad \alpha(dBcm^{-1}) = 4.3429 \cdot \alpha(cm^{-1}) \tag{1.2}$$

- **Thermo-optic coefficient (dn/dT):** is the rate of change of refractive index as a function of temperature. Achieving high values enables low power thermal tuning of photonic devices, with the benchmark established in silicon on insulator platform (1.8 x 10^{-4}RIU/°C) [16]. It is intrinsic to the platform, but can be modified by changing the stoichiometry or introducing optical claddings [17, 18]. **Chapter 5** overviews the thermo-optic effect but as a general introduction, it depends on the expansion coefficients of core, cladding and substrate and the mismatches between them, creating additional strain.

  With high power photon sources, the relationship between the polarization in the material and the electric field is non-linear. Particularly, the polarization can be expressed as a sum of several terms [19]:

$$P = \varepsilon_o \chi^{(1)} \xi + \varepsilon_o \chi^{(2)} \xi^2 + \varepsilon_o \chi^{(3)} \xi^3 + ... \tag{1.3}$$

- **Second order non-linear coefficient ($\chi^{(2)}$):** describes the non-linear response of a material to light where the interaction is proportional to the square of the electromagnetic field. It is responsible for second harmonic generation processes (frequency doubling) [20]. When defined in pm/V, the value determines how efficiently the material responds when applied to an electric field and with higher values, less voltage needs to be applied for electro-optic tuning of photonic devices [21]. It occurs in materials that lack inversion symmetry and a commonly used material for electro-optic devices is lithium niobate ($LiNbO_3$ or LN). In **Chapter 6** it is shown the hybrid integration of lithium niobate with amorphous silicon carbide.

- **Third-order non-linear coefficient ($\chi^{(3)}$):** describes the interaction of the electromagnetic field with a material with the third-order term and it is present in all materials. It is a critical parameter for supercontinuum generation, four-wave mixing and frequency combs, being high in materials such as silicon and amorphous silicon carbide [22–24].

1

1.5. OUTLINE OF THE THESIS

The scope of this thesis includes:

Chapter 2 gives an overview of different integrated photonic platforms, the most common photonic components used as building blocks and main tuning mechanisms to achieve reconfigurability, providing representative applications in the field of integrated photonics. It also presents the current state of the art for silicon carbide photonic devices.

Chapter 3 reviews all the experimental techniques and gives detailed information and schematics about the deposition tools, the fabrication process for photonic devices and superconducting detectors and the main optical measurement setups used during this thesis, both for cryogenics and room temperature.

Chapter 4 shows the development of high quality amorphous silicon carbide thin films using ICPCVD technique (see fig.1.2a) and compares it with conventional plasma-enhanced CVD (PECVD) devices. We fabricate standard waveguides and ring resonators with a high-quality factor (beyond $5x10^5$) corresponding to three times lower losses (0.78 dB/cm) than the current state-of-the-art for a-SiC (3 dB/cm) [25] (fig.1.2b). Most importantly, due to the deposition at low temperatures, we discuss its suitability for hybrid integrated photonics in SiN and temperature-sensitive platforms.

Chapter 5 studies the thermal tunability of photonic devices using engineered silicon dioxide claddings (deposited using ICPCVD). We discuss the influence of deposition temperature and chamber pressure (fig.1.2c) on the performance of the cladding. We achieve large thermo-optic shifts, athermal devices, and bi-directional thermal response deterministically and on a single chip (fig.1.2d). We also demonstrate basic device configurations exploiting these properties and a configuration using cladding lift-off to reduce the thermal crosstalk between photonic devices.

Chapter 6 shows the integration of superconducting nanowire single photon detectors saturating at 950 nm with amorphous silicon carbide photonic components for future quantum photonic experiments (fig.1.2e).

Chapter 7 reviews the additional studies that have been performed with this platform in the field of integrated photonics, mainly the hybrid integration with polymers, lithium niobate and silicon nitride (fig.1.2f). It also summarizes the results obtained in the thesis, highlights the challenges and provides future opportunities for this platform.

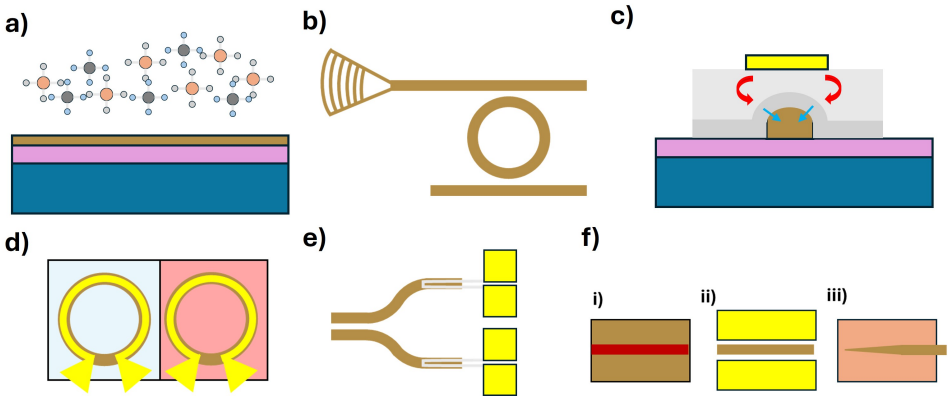

Figure 1.2: Pictorial view of the subjects treated in this thesis: a) the deposition of a-SiC films via CVD techniques, b) the fabrication of high quality photonic devices, c) the tuning of the thermo-optic tunability of photonic devices with silicon dioxide claddings, d) the use of these claddings deterministically for passive and active ring resonators, e) the integration of a-SiC with SNSPDs and f) the hybrid integration of a-SiC with i) polymers, ii) lithium niobate and iii) silicon nitride.

REFERENCES

[1] H.-S. Zhong, H. Wang, Y.-H. Deng, M.-C. Chen, L.-C. Peng, Y.-H. Luo, J. Qin, D. Wu, X. Ding, Y. Hu, *et al.*, *Quantum computational advantage using photons,* Science **370**, 1460 (2020).

[2] W. Bogaerts, D. Pérez, J. Capmany, D. A. Miller, J. Poon, D. Englund, F. Morichetti, and A. Melloni, *Programmable photonic circuits,* Nature **586**, 207 (2020).

[3] S. Bandyopadhyay, A. Sludds, S. Krastanov, R. Hamerly, N. Harris, D. Bunandar, M. Streshinsky, M. Hochberg, and D. Englund, *Single-chip photonic deep neural network with forward-only training,* Nature Photonics **18**, 1335 (2024).

[4] D. Pérez-López, A. López, P. DasMahapatra, and J. Capmany, *Multipurpose self-configuration of programmable photonic circuits,* Nature communications **11**, 6359 (2020).

[5] M. C. Estevez, M. Alvarez, and L. M. Lechuga, *Integrated optical devices for lab-on-a-chip biosensing applications,* Laser & Photonics Reviews **6**, 463 (2012).

[6] J. Wang, M. M. Sanchez, Y. Yin, R. Herzer, L. Ma, and O. G. Schmidt, *Silicon-based integrated label-free optofluidic biosensors: latest advances and roadmap,* Advanced Materials Technologies **5**, 1901138 (2020).

[7] Y.-T. Chen, Y.-C. Lee, Y.-H. Lai, J.-C. Lim, N.-T. Huang, C.-T. Lin, and J.-J. Huang, *Review of integrated optical biosensors for point-of-care applications,* Biosensors **10**, 209 (2020).

[8] E. Pelucchi, G. Fagas, I. Aharonovich, D. Englund, E. Figueroa, Q. Gong, H. Hannes, J. Liu, C.-Y. Lu, N. Matsuda, *et al., The potential and global outlook of integrated photonics for quantum technologies,* Nature Reviews Physics **4**, 194 (2022).

[9] A. W. Elshaari, W. Pernice, K. Srinivasan, O. Benson, and V. Zwiller, *Hybrid integrated quantum photonic circuits,* Nature photonics **14**, 285 (2020).

[10] M. Turunen, M. Brotons-Gisbert, Y. Dai, Y. Wang, E. Scerri, C. Bonato, K. D. Jöns, Z. Sun, and B. D. Gerardot, *Quantum photonics with layered 2d materials,* Nature Reviews Physics **4**, 219 (2022).

[11] W. Xie, C. Xiang, L. Chang, W. Jin, J. Peters, and J. E. Bowers, *Silicon-integrated nonlinear iii-v photonics,* Photonics Research **10**, 535 (2022).

[12] I. Marinkovic, M. Drimmer, B. Hensen, and S. Gro¨blacher, *Hybrid integration of silicon photonic devices on lithium niobate for optomechanical wavelength conversion,* Nano letters **21**, 529 (2021).

[13] J. Smith, D. Jevtics, B. Guilhabert, M. Dawson, and M. Strain, *Hybrid integration of chipscale photonic devices using accurate transfer printing methods,* Applied Physics Reviews **9, 4** (2022).

[14] P. Kaur, A. Boes, G. Ren, T. G. Nguyen, G. Roelkens, and A. Mitchell, *Hybrid and heterogeneous photonic integration,* APL Photonics **6, 6** (2021).

[15] A. Yi, Y. Zheng, H. Huang, J. Lin, Y. Yan, T. You, K. Huang, S. Zhang, C. Shen, M. Zhou, *et al., Wafer-scale 4h-silicon carbide-on-insulator (4h–sicoi) platform for nonlinear integrated optical devices,* Optical Materials **107**, 109990 (2020).

[16] J. Komma, C. Schwarz, G. Hofmann, D. Heinert, and R. Nawrodt, *Thermo-optic coefficient of silicon at 1550 nm and cryogenic temperatures,* Applied physics letters **101** (2012).

[17] L.-Y. S. Chang, S. Pappert, and P. K. Yu, *High thermo-optic tunability in pecvd silicon-rich amorphous silicon carbide,* Optics letters **48**, 1188 (2023).

[18] F. A. Memon, F. Morichetti, and A. Melloni, *High thermo-optic coefficient of silicon oxycarbide photonic waveguides,* ACS Photonics **5**, 2755 (2018).

[19] A. M. Fox, *Quantum optics: an introduction*, Vol. 15 (Oxford university press, 2006).

[20] R. Luo, Y. He, H. Liang, M. Li, and Q. Lin, *Highly tunable efficient second-harmonic generation in a lithium niobate nanophotonic waveguide,* Optica **5**, 1006 (2018).

[21] Y. Hu, D. Zhu, S. Lu, X. Zhu, Y. Song, D. Renaud, D. Assumpcao, R. Cheng, C. Xin, M. Yeh, *et al., Integrated electro-optics on thin-film lithium niobate,* Nature Reviews Physics , 1 (2025).

[22] N. K. Hon, R. Soref, and B. Jalali, *The third-order nonlinear optical coefficients of Si, Ge, and* $Si_{1-x}Ge_x$ in the midwave and longwave infrared, Journal of Applied Physics **110** (2011).

[23] Y. Lu, X. Shi, A. Ali Afridi, Y. Wang, V. Tabouret, D. Chaussende, K. Rottwitt, and H. Ou, *Strong third-order nonlinearity in amorphous silicon carbide waveguides,* Optics Letters **49**, 4389 (2024).

[24] P. Xing, D. Ma, L. C. Kimerling, A. M. Agarwal, and D. T. Tan, *High efficiency four wave mixing and optical bistability in amorphous silicon carbide ring resonators,* APL Photonics **5** (2020).

[25] P. Xing, D. Ma, K. J. Ooi, J. W. Choi, A. M. Agarwal, and D. Tan, *Cmos-compatible pecvd silicon carbide platform for linear and nonlinear optics,* ACS Photonics **6**, 1162 (2019).

2

INTEGRATED PHOTONICS: CONTROLLING LIGHT ON A CHIP

This chapter provides an overview of the primary material platforms used in integrated photonic devices, highlighting their key characteristics for various applications. We explore the fundamental components of an integrated photonic circuit, including elements for coupling, filtering, routing, and modulating light. Additionally, we examine the main tuning mechanisms for photonic devices and discuss waveguide-integrated superconducting detectors across different platforms. The applications of integrated photonic circuits in quantum information processing, communications, LiDAR, biosensing, and quantum technologies are also reviewed. Finally, we summarize the latest advancements in silicon carbide-based photonic platforms.

2.1. INTEGRATED PHOTONIC DEVICES

2.1.1. MATERIAL PLATFORMS

The choice of material platform is important in integrated photonics, since it dictates the device performance, fabrication complexity, and specific application. **Silicon-on-insulator (SOI)** is a dominant platform due to several key properties. Silicon's high refractive index contrast with the silica cladding permits ultracompact photonic devices. The reduced footprint reduces the power consumption in active configurations. Most importantly, this platform is compatible with mature CMOS processes, which enable dense, low-loss waveguides and tunable circuits [1–6]. An important disadvantage is that at telecommunication wavelengths silicon presents two-photon absorption which limits the efficiency of Kerr non-linearities. On the other hand, this platform lacks transparency in the visible part of the spectrum, has high sensitivity to temperature variations and susceptibility to sidewall roughness due to the reduced dimensions. All of these made platforms like **silicon nitride (SiN)** more appealing, offering broader wavelength coverage, deposition processes enabling to combine it with other photonic platforms, benefits from lower propagation losses, and have gathered attention for various linear and non-linear applications due to the absence of non-linear absorption losses [7–14]. Nevertheless, both SOI and SiN platforms lack the presence of intrinsic photon sources unless they are integrated with light sources made from III-V materials [15, 16]. For active functionalities such as light emission, amplification and detection, **III-V semiconductors** (e.g., indium phosphide (InP) and gallium arsenide (GaAs)) enable integrated lasers, photodetectors, and optical amplifiers. However, their integration with silicon often requires hybrid or heterogeneous approaches to address lattice mismatch and thermal challenges with reduced scalability and CMOS compatibility [17, 18]. Emerging platforms like **lithium niobate-on-insulator (LNOI)** have gained popularity for their exceptional electro-optic coefficients, enabling ultra-fast modulators and efficient wavelength conversion [19–23], while **polymers** offer flexibility, cost-effective fabrication and potential for scalability [24–29]. Due to the increasing demand for more complex applications, the field is slowly shifting toward **hybrid systems**, combining materials with single photon sources on InP waveguides with silicon photonics [30] or LNOI modulators made together with SiN [31, 32], silicon [33] or even silicon carbide [34, 35], exploiting synergies between platforms. The table below summarizes some of the platforms together with several parameters of interest such as refractive index, quality factor, thermo-optic coefficient, second order non-linear coefficient and non-linear refractive index. Specific

explanations of each property can be found in the introductory chapter.

Material	Index (n)	Q (x10^6)	TOC (RIU/C)	χ_2 (pm/V)	n_2 (m^2/W)	ref.
SOI	3.48	22	1.8×10^{-4}	—	5 x 10^{-18}	[36, 37]
SiN	1.9-2.1	420	2.4×10^{-5}	—	2.6 x 10^{-19}	[38, 39]
InP	3.16	0.045	2.01×10^{-5}	287	1.5 x 10^{-16}	[40–42]
GaAs	3.4	3.2	2.67×10^{-5}	170*	1.6 x 10^{-17}	[36, 43]
LNOI	2.21	80	3.95×10^{-5}	27	9.1 x 10^{-20}	[36, 44]
4H-SiCOI	2.56	5.6	4.94×10^{-5}	18	9.6 x 10^{-19}	[45–47]
PECVD a-SiC	2.45	0.16	2.77×10^{-5}	—	4.8 x 10^{-18}	[48]
ICPCVD a-SiC	2.55	0.57	7.3×10^{-5}	—	-	[49]
AlN	2.12	1	2.32×10^{-5}	4.7	2.3 x 10^{-19}	[50–52]

Table 2.1: Summary of optical and nonlinear parameters for various photonic materials at a wavelength of 1550 nm. The values for quality factor are given for loaded. Table inspired by [36]. *Value at 1064 nm.

.

2.1.2. BASIC BUILDING BLOCKS

Integrated photonic circuits should be able to couple light coming from outside or generate it on chip, route, filter and manipulate the photons and finally, detect these photons. For more comprehensive information about the specific components listed here and more advanced concepts, L. Chrostowski et.al [53] provide a guide for silicon photonics design. Below are introduced the most basic building blocks that we can find on integrated photonics:

Waveguides are the simplest elements of integrated photonic systems, enabling the confinement and guided propagation of light at the micro- and nanoscale. Typically fabricated from high-refractive-index materials like silicon nitride, silicon-on-insulator, silicon carbide or polymers, waveguides operate by total internal reflection, channeling light through a core surrounded by lower-index cladding layers [54, 55].

Grating couplers (fig.2.1a) are critical interfaces between optical fibers and on-chip waveguides. Their traditional configuration consists of a periodic array of nanostructures (grating) to couple light vertically. Their design flexibility and compatibility with wafer-scale testing make them an indispensable component of modern industrial photonic circuits. However, wavelength sensitivity and polarization dependence require careful optimization [56, 57]. **Edge-tapered couplers** (fig.2.1b) are made by adiabatically tapering waveguide widths at chip edges to match the mode profile of optical fibers, achieving low-loss, polarization-insensitive coupling ideal for high-power or broadband applications [58, 59].

For compact filtering, modulation and sensing one can use **ring resonators** [60]. These devices consist of a closed-loop waveguide coupled to one or more straight bus waveguides (fig.2.1c). When the optical path length of the ring matches an integer multiple of the wavelength, constructive interference occurs, resonantly enhancing specific wavelengths while suppressing others. The quality factor (Q-factor), free spectral range (FSR), and extinction ratio of the resonator depend on the coupling strength, ring circumference, and waveguide loss. These parameters are discussed more in detail in **chap-**

ter 4. In a similar way, **photonic crystal cavities** (fig.2.1d) engineered with periodic nanostructures, confine light in ultra-small volumes reaching quality factors of $Q > 10^6$ [61].

Passive light splitting and routing can be achieved by using **y-splitters** (fig.2.1e)[62] and **multi-mode interferometers (MMI)** (fig.2.1f) [63].

Phase modulators dynamically control light by altering the refractive index primarily through electro-optic and thermo-optic effects. In combination with them, **Mach-Zehnder interferometers (MZIs)** exploit light interference to modulate, switch, or sense optical signals. A basic MZI consists of two parallel waveguides connected by a pair of optical couplers, forming two arms of equal or unequal length (fig.2.1g). By introducing a phase difference between the arms—via thermo-optic (fig.2.1h), electro-optic (fig.2.1i), or strain-induced refractive index change—the output intensity in the ports can be modulated [64, 65].

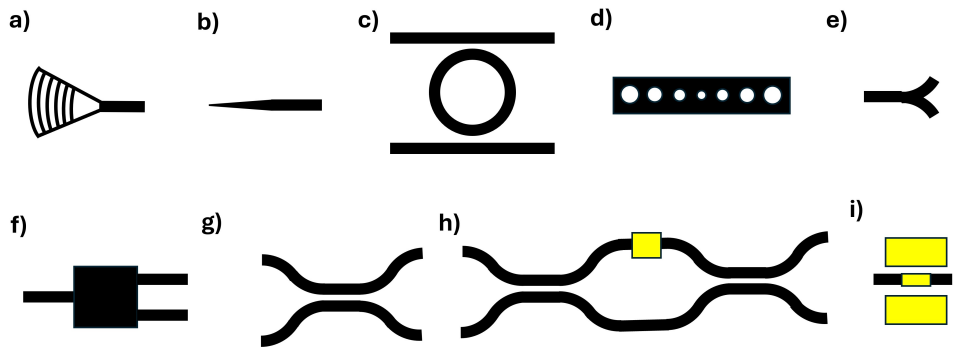

Figure 2.1: Basic photonic elements that are used for purposes such as coupling light vertically via a) grating couplers or horizontally with b) edge couplers. Some of the most common filtering elements are c) a ring resonator and d) a photonic crystal cavity. To route and split the light one can use e) a y-splitter, f) a multimo-mode interferometer, g) a passive beam-splitter, h) a Mach-Zehnder interferometer which uses i) a phase shifter achieved with electro-optics (gold pads on the side) or thermo-optics (micro-heater on top).

2.1.3. TUNING OF PHOTONIC DEVICES

Tunable components are essential for dynamically controlling light in integrated photonic systems, enabling reconfigurable optical circuits and precise wavelength shifts. The most utilized approach to accomplish this task is via **thermal tuning** using the thermo-optic effect. In this configuration, integrated metallic microheaters modify the refractive index of the waveguide material by inducing heat with a current (fig.2.2a), enabling phase shifts and resonance wavelength adjustments in devices like ring resonators and Mach-Zehnder interferometers [39, 66], following the general equation:

$$\Delta\Phi = \frac{2\pi L}{\lambda_0}\frac{dn(\lambda)}{dT}\Delta T \tag{2.1}$$

where L is the length of the thermo-optically tunable section, λ_0 is the wavelength of the light in vacuum, dn/dT is the thermo-optic coefficient of the material and ΔT is the temperature change. **Chapter 5** dives into the mechanisms of the thermo-optic effect and tackles one of the challenges present in integrated photonic platforms, achieving small and large thermal tunabilities with opposite signs on the sample platform. While simple to implement and highly stable, thermal tuning suffers from slow response times (milliseconds) and high power consumption. In contrast, **electro-optic tuning** exploits electric-field-induced refractive index changes using contact pads in-plane (or out-of-plane depending on the polarizability) in between the waveguides in materials like lithium niobate or III-V semiconductors (fig.2.2b), achieving up to 500 GHz modulation with minimal power dissipation [67, 68]. The phase difference in this case is related to the electric field applied between electrodes with the relation:

$$\Delta\Phi = -\frac{\pi L}{\lambda_0} n^3 r E \tag{2.2}$$

In this equation, n is the refractive index, r the electro-optic coefficient of the material and E is the applied electric field. This approach, critical for high-speed optical modulators and switches, benefits from materials with strong Pockels effect, though challenges remain in integrating such materials with CMOS platforms. With this purpose, **Chapter 6** shows the successful integration and application of amorphous silicon carbide with lithium niobate [35].

Despite this not being covered in the thesis, **mechanical tuning** of photonic devices have gathered attention recently. This method is enabled by micro-electro-mechanical systems (MEMS), which physically adjust photonic components such as waveguide gaps or suspended ring resonators via piezoelectric actuation (2.2c). MEMS-based tuning offers sub-microsecond response times, low optical loss and non-thermal operation, making it ideal for reconfigurable photonic circuits [69–71].

2.2. PHOTONICS FOR QUANTUM APPLICATIONS

Photon sources and detectors are an essential aspect of current and future photonic applications. In this section we will discuss the different material platforms that host or can be used to generate single photons. Additionally, we will also review the integration of superconducting single photon detectors on standard photonic platforms using a variety of superconducting materials.

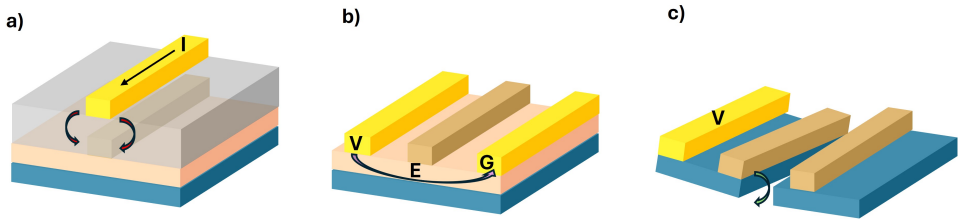

Figure 2.2: Concept scheme for a) thermal tuning using micro-heaters on the top of the waveguides, b) electro-optic tuning using in-plane contacts to create an electric field in the electro-optic material and c) mechanical tuning using piezoelectric materials.

2.2.1. PHOTON SOURCES

Until very recently, the inclusion of single photon emitters in SOI and SiN platforms required pick-and-place integration of emitters [72]. However, researchers demonstrated silicon nitride single-photon emitters that can be intrinsically generated, enabling efficient routing on the same platform [73, 74]. III–V semiconductor chips (e.g. GaAs or InP) can host **epitaxial quantum dots** within the photonic structure, yielding bright and deterministic single-photon emission [75]. While LN does not natively host quantum emitters, **periodically poled lithium niobate (PPLN)** can be used to generate entangled photon pairs through spontaneous parametric down conversion (SPDC)[76, 77]. Additionally, wide-bandgap materials such as **diamond and silicon carbide (SiC)** serve as both photonic platform and emitter host, with embedded color centers based on NV, SiV or divacancy centers with long spin coherence [78–80] or based on spontaneous four-wave mixing (SFWM) [81]. Another approach uses **two-dimensional materials** (like hBN or WSe_2) as single-photon emitters that can be layered onto photonic chips [82–86]; their atomic thickness allows tight coupling to underlying waveguide modes, but precise placement and emitter stability (often requiring cryogenic operation or post-processing to activate narrow-line emitters) are important considerations in integrating 2D sources.

2.2.2. WAVEGUIDE-INTEGRATED SNSPDS

Waveguide-integrated superconducting nanowire single-photon detectors (SNSPDs) combines the sensitivity and broad detection window of superconducting nanowires with the reconfigurability of integrated photonic circuits. These devices consist of ultrathin superconducting nanowires made of niobium nitride (NbN), niobium titanium nitride (NbTiN), tungsten silicide (WSi) or molybdenum silicide (MoSi) among others, patterned directly on photonic waveguides or deterministically embedded, enabling efficient coupling of guided optical modes to the active detection region. Waveguide-integrated SNSPDs achieve near-unity on-chip quantum detection efficiency [87], ultra-low dark count rates [88], and picosecond-level timing resolution [89, 90], making them indispensable for applications requiring single-photon sensitivity, such as quantum key distribution (QKD), light detection and ranging (LiDAR), and quantum computing [91, 92]. Their integration with photonic waveguides minimizes optical losses and alignment challenges inherent in free-space systems, while enabling scalable, on-chip architectures. SNSPDs have been successfully integrated in different photonic material platforms such

as Si [87, 93–97], SiN [98–105], GaAs [106–111], AlN [112], $LiNbO_3$ [113, 114], Ta_2O_5 [115] and diamond [116–118].

2.3. APPLICATIONS OF INTEGRATED PHOTONIC CIRCUITS

In this section we will explore some of the most relevant works highlighting the different application areas for integrated photonic circuits. Some of them are in very early stage, while others have gathered funding and consolidated into well known startup companies in the world.

2.3.1. QUANTUM INFORMATION PROCESSING AND COMMUNICATIONS

In quantum communications, photonic integrated circuits can ensure compact, chip-scale optical satellite links [119] and quantum key distribution systems, where entangled photon pairs, generated via nonlinear processes in waveguides or microring resonators, are routed through with minimal decoherence [120–122]. On-chip beam splitters, phase modulators, and superconducting nanowire single-photon detectors enable high-speed, fault-tolerant quantum networks, while resonant cavities could enhance photon-emitter interactions for efficient quantum light sources. For quantum computing, integrated photonics facilitates linear optical quantum processing using the KLM protocol [123] by controlling complex interferometric arrays with Mach-Zehnder interferometers and tunable phase shifters, enabling two-photon gates and boson sampling experiments [124–127]. Hybrid platforms, such as silicon carbide hosting silicon-vacancy centers or lithium niobate modulators for fast qubit control, further bridge photonic and solid-state quantum systems [128–130]. Integrated photonic platforms enable the generation of microcombs—compact frequency combs that offer high precision and stability for quantum applications. By harnessing second-order nonlinearities, one can achieve efficient frequency conversion processes critical for generating entangled photon pairs, while third-order nonlinear devices enable wavelength conversion, parametric amplification, signal regeneration or optical demultiplexing among others [131–137]. These advancements are essential for secure quantum communications, scalable quantum information processing and linear optical computing [138].

2.3.2. LIGHT DETECTION AND RANGING

Modern LiDAR systems use photonic integrated circuits to generate, steer, and detect laser pulses with unprecedented precision and speed. On-chip semiconductor lasers, such as those fabricated in indium phosphide or hybrid III-V/silicon platforms, emit coherent light at near-infrared wavelengths, while optical phased arrays (OPAs), composed of tunable phase shifters and grating antennas, enable solid-state beam steering without moving parts, enhancing reliability and scan rates [139–142]. Silicon nitride and silicon photonics further reduce propagation losses and enable dense integration of components like Mach-Zehnder modulators for frequency-modulated continuous-wave (FMCW) LiDAR, which improves depth resolution and reduce the impact of ambient light [143].

2.3.3. BIOSENSING

Integrated photonics is redefining biosensing by enabling ultra-sensitive, portable, and multiplexed platforms for real-time detection of biomolecules, pathogens, and cellular interactions. With the use of ring resonators and photonic crystal cavities it is possible to detect small changes in refractive index caused by molecular binding events on functionalized waveguides, achieving label-free sensing with sub-picomolar sensitivity. Advanced designs, such as plasmonic-photonic hybrid structures, enhance light-matter interaction for single-molecule detection [144] or broadband spectrometers on a lithium niobate platform [145]. Integrated microfluidics enable "lab-on-a-chip" systems for point-of-care diagnostics [146]. Photonic devices can also improve the current tomographic ultrasonic and photoacoustic techniques with optomechanical ultrasound sensors. These sensors have been successfully demonstrated to provide images of fast-moving objects, leaf veins and live zebrafish [147, 148].

2.4. STATE-OF-THE-ART FOR SILICON CARBIDE PHOTONIC PLATFORMS

The main goal of this thesis is to highlight current and new fabrication methods for high-performance optical devices made on silicon carbide. In this section, we will provide an overview of the state of the art for both crystalline and amorphous silicon carbide photonic platforms. The works provided here will extend the literature review shown and published in **chapter 4** with research that appeared later in the field.

2.4.1. CRYSTALLINE SILICON CARBIDE

Silicon carbide is a semiconductor commonly known in applications for high power electronics that has emerged as an attractive material platform for integrated photonics, with advantages over other materials like silicon or silicon nitride. With a wide bandgap, great thermal and chemical stability, a high refractive index, transparency in the visible and infrared wavelengths and strong second- and third-order nonlinearities, this material enables high-performance photonic devices [149]. From the several crystalline forms or polytypes, the most commonly used ones are 4H-SiC (hexagonal), 6H-SiC (hexagonal) and 3C-SiC (cubic). As stated in the introduction, to use this material for integrated photonic devices, the first step is transfer-bonding with silicon dioxide, a low refractive index material, to form silicon carbide on insulator (SiCOI). 4H-SiCOI ring resonators with waveguide width of 3 μm and thickness of 530 nm have been fabricated to perform optical parametric oscillators with quality factors of 1.1 x 10^6 [150]. In another article, researchers used the same platform to study soliton microcombs and achieving quality factors as high as 5.6 x 10^6 in ring resonators with waveguide width of 1.85 μm and thickness between 500 nm and 600 nm [151]. The highest values achieved in 4H-SiCOI platforms reached 7.1 x 10^6 (mean Q of 6.75 x 10^6) on whispering gallery mode resonators (not waveguide-based devices) [45]. For 3C-SiCOI platform, suspended devices have shown quality factors of 4.1 x 10^4 [152] while the highest reported was 1.42 x 10^5 with 40 μm ring radius, waveguide width of 1700 nm and thickness of 500 nm [153]. Recent progress in the integration of 3C-SiCOI with lithium niobate demonstrated optical devices with loaded quality factors of 1.4 x 10^3 and electro-optic tunability of 6.2 pm/V

[34]. These devices were made on films with 280 nm in thickness and had a waveguide width of 900 nm tapered down to 450 nm to enhance the mode interaction with lithium niobate. Other works have shown integration of silicon carbide with epitaxially grown AlGaAs quantum dot lasers [154] and embedded InGaAs QDs on GaAs waveguides [155].

2.4.2. AMORPHOUS SILICON CARBIDE

To avoid the need for transfer bonding, using chemical vapor deposition techniques it is possible to form amorphous SiC, a disordered variant. This material combines the benefits of SiC with CMOS-compatible low-temperature fabrication and the possibility to include it on a larger variety of substrate materials with precise thickness control. Most importantly, the CVD process allows to tune the composition, affecting the refractive index, the non-linear properties and the operation wavelength. In 2014, researchers showed PECVD a-SiC optical disk resonators with quality factors of 1.3 x 10^5 for optical Kerr non-linear experiments with a Kerr non-linearity of 5.9×10^{-15} cm^2/W [156]. A recent work fabricated PECVD a-SiC optical ring resonators achieving intrinsic quality factors of 1.6 x 10^5 being, at the time of publication (2019), the highest ever recorded among all SiC platforms with waveguide propagation losses of 3 dB/cm [48]. Most importantly, they used a reduced temperature of 300°C making it compatible with CMOS processes. Using these devices in a second work, the same researchers performed four-wave mixing (FWM) experiments. They recorded a third-order non-linear coefficient ten times higher (4.8×10^{-14} cm^2/W) than crystalline silicon carbide and silicon nitride [157]. Advances in deposition techniques made it possible to increase these quality factors exceeding 5 x 10^5 during this thesis [49] representing three times higher values and at half the deposition temperature (150°C), hence advancing heterogeneous integration with a wider variety of materials that were not compatible with the standard 300°C. During this time, another work showed that PECVD a-SiC could be tuned to achieve the highest thermal tunability in a platform with a TOC of 1.88 x 10^{-4}/°C comparable to Si [158]. The device geometry was a ring resonator with radius of 50 μm, gap between bus and ring waveguide varying between 100 nm and 400 nm, a waveguide width of 875 nm and a thickness of 320 nm. Nevertheless, the optical devices had quality factors of 10^3 hinting that this tuning mechanism could affect their performance. Recently, researchers used PECVD a-SiC films deposited with different recipes to achieve high third-order non-linearities [159]. The achieved a non-linear refractive index of 6.7 x 10^{-18} m^2/W for a refractive index of 2.80, comparable to silicon, a commonly used non-linear material. For hybrid integration, while there is a work based on simulations showing the combination of a-SiC with lithium niobate [160], the only experimental work showing this platform with electro-optic modulation is shown by Z.Li et. al [35]. Here it is demonstrated an electro-optic tunability of 3.4 pm/V and quality factors exceeding 10^5 in racetrack ring resonators with bending radius 120 μm, waveguide width of 800 nm and thickness of 280 nm.

2.5. CONCLUSION

This chapter lays the foundation for understanding the materials, components, and functionalities of integrated photonic devices, which are essential for the discussions in subsequent chapters. Furthermore, it expands on the literature presented in the main publications for state-of-the-art silicon carbide photonic devices within the scope of this thesis. The sections presented here will be particularly relevant when going through device geometry optimization, photonic device integration, and emerging applications in quantum and hybrid photonics.

REFERENCES

[1] S. Shekhar, W. Bogaerts, L. Chrostowski, J. E. Bowers, M. Hochberg, R. Soref, and B. J. Shastri, *Roadmapping the next generation of silicon photonics,* Nature Communications **15**, 751 (2024).

[2] W. Bogaerts, D. Taillaert, B. Luyssaert, P. Dumon, J. V. Campenhout, P. Bienstman, D. V. Thourhout, R. Baets, V. Wiaux, and S. Beckx, *Basic structures for photonic integrated circuits in silicon-on-insulator,* Optics Express **12**, 1583 (2004).

[3] J. Wang and Y. Long, *On-chip silicon photonic signaling and processing: a review,* Science Bulletin **63**, 1267 (2018).

[4] P. Steglich, M. Hülsemann, B. Dietzel, and A. Mai, *Optical biosensors based on silicon-on-insulator ring resonators: A review,* Molecules **24**, 519 (2019).

[5] C. Li, D. Liu, and D. Dai, *Multimode silicon photonics,* Nanophotonics **8**, 227 (2019).

[6] Y. Zhang, C. Husko, S. Lefrancois, I. H. Rey, T. F. Krauss, J. Schröder, and B. J. Eggleton, *Non-degenerate two-photon absorption in silicon waveguides: analytical and experimental study,* Optics express **23**, 17101 (2015).

[7] K. A. Buzaverov, A. S. Baburin, E. V. Sergeev, S. S. Avdeev, E. S. Lotkov, S. V. Bukatin, I. A. Stepanov, A. B. Kramarenko, A. S. Amiraslanov, D. V. Kushnev, *et al.*, *Silicon nitride integrated photonics from visible to mid-infrared spectra,* Laser & Photonics Reviews **18**, 2400508 (2024).

[8] C. Xiang, W. Jin, and J. E. Bowers, *Silicon nitride passive and active photonic integrated circuits: trends and prospects,* Photonics research **10**, A82 (2022).

[9] M. Corato-Zanarella, X. Ji, A. Mohanty, and M. Lipson, *Absorption and scattering limits of silicon nitride integrated photonics in the visible spectrum,* Optics Express **32**, 5718 (2024).

[10] X. Ji, Y. Okawachi, A. Gil-Molina, M. Corato-Zanarella, S. Roberts, A. L. Gaeta, and M. Lipson, *Ultra-low-loss silicon nitride photonics based on deposited films compatible with foundries,* Laser & Photonics Reviews **17**, 2200544 (2023).

[11] A. Dutt, C. Joshi, X. Ji, J. Cardenas, Y. Okawachi, K. Luke, A. L. Gaeta, and M. Lipson, *On-chip dual-comb source for spectroscopy,* Science advances **4**, e1701858 (2018).

[12] D. R. Carlson, D. D. Hickstein, A. Lind, S. Droste, D. Westly, N. Nader, I. Coddington, N. R. Newbury, K. Srinivasan, S. A. Diddams, *et al.*, *Self-referenced frequency combs using high-efficiency silicon-nitride waveguides,* Optics letters **42**, 2314 (2017).

[13] J. S. Levy, M. A. Foster, A. L. Gaeta, and M. Lipson, *Harmonic generation in silicon nitride ring resonators,* Optics express **19**, 11415 (2011).

[14] E. Nitiss, J. Hu, A. Stroganov, and C.-S. Brès, *Optically reconfigurable quasi-phase-matching in silicon nitride microresonators,* Nature Photonics **16**, 134 (2022).

[15] C. Xiang, J. Guo, W. Jin, L. Wu, J. Peters, W. Xie, L. Chang, B. Shen, H. Wang, Q.-F. Yang, *et al.*, *High-performance lasers for fully integrated silicon nitride photonics,* Nature communications **12**, 6650 (2021).

[16] C. Xiang, W. Jin, O. Terra, B. Dong, H. Wang, L. Wu, J. Guo, T. J. Morin, E. Hughes, J. Peters, *et al.*, *3d integration enables ultralow-noise isolator-free lasers in silicon photonics,* Nature **620**, 78 (2023).

[17] Y. Wang, Y. Jiao, and K. Williams, *Scaling photonic integrated circuits with inp technology: A perspective,* APL Photonics **9** (2024).

[18] C. P. Dietrich, A. Fiore, M. G. Thompson, M. Kamp, and S. Höfling, *Gaas integrated quantum photonics: towards compact and multi-functional quantum photonic integrated circuits,* Laser & Photonics Reviews **10**, 870 (2016).

[19] D. Zhu, L. Shao, M. Yu, R. Cheng, B. Desiatov, C. Xin, Y. Hu, J. Holzgrafe, S. Ghosh, A. Shams-Ansari, *et al.*, *Integrated photonics on thin-film lithium niobate,* Advances in Optics and Photonics **13**, 242 (2021).

[20] Z. Li, R. N. Wang, G. Lihachev, J. Zhang, Z. Tan, M. Churaev, N. Kuznetsov, A. Siddharth, M. J. Bereyhi, J. Riemensberger, *et al.*, *High density lithium niobate photonic integrated circuits,* Nature Communications **14**, 4856 (2023).

[21] K. Luke, P. Kharel, C. Reimer, L. He, M. Loncar, and M. Zhang, *Wafer-scale low-loss lithium niobate photonic integrated circuits,* Optics Express **28**, 24452 (2020).

[22] H. Feng, T. Ge, X. Guo, B. Wang, Y. Zhang, Z. Chen, S. Zhu, K. Zhang, W. Sun, C. Huang, *et al.*, *Integrated lithium niobate microwave photonic processing engine,* Nature **627**, 80 (2024).

[23] B. Pan, H. Liu, Y. Huang, Z. Yu, H. Li, Y. Shi, L. Liu, and D. Dai, *Perspective on lithium-niobate-on-insulator photonics utilizing the electro-optic and acousto-optic effects,* ACS Photonics **10**, 2078 (2023).

[24] Y. Huang, G. Li, T. Bai, Y. Shin, X. Wang, A. I. More, P. Boucher, C. Chandrasekaran, J. Liu, and H. Fang, *Flexible electronic-photonic 3d integration from ultrathin polymer chiplets,* npj flexible electronics **8**, 61 (2024).

[25] M. T. Khoshmehr, M. M. Dashtabi, H. Nikbakht, B. L. Rodriguez, N. Sharma, I. E. Zadeh, B. van Someren, and B. I. Akca, *Versatile hybrid optical waveguides in amorphous silicon carbide with enhanced functionality and performance,* Applied Physics Letters **125** (2024).

[26] E. Hack, I. Shorubalko, J. Graf, P. Zolliker, and E. Mavrona, *Fabrication of freestanding photonic devices combining polymer films with microfabrication techniques and 3d printing,* Optics Express **31**, 29968 (2023).

[27] X.-Y. Han, Z.-L. Wu, S.-C. Yang, F.-F. Shen, Y.-X. Liang, L.-H. Wang, J.-Y. Wang, J. Ren, L.-Y. Jia, H. Zhang, *et al.*, *Recent progress of imprinted polymer photonic waveguide devices and applications,* Polymers **10**, 603 (2018).

[28] H. Zuo, S. Yu, T. Gu, and J. Hu, *Low loss, flexible single-mode polymer photonics,* Optics Express **27**, 11152 (2019).

[29] M. Weis, *Organic semiconducting polymers in photonic devices: From fundamental properties to emerging applications,* Applied Sciences **15**, 4028 (2025).

[30] J.-H. Kim, S. Aghaeimeibodi, C. J. Richardson, R. P. Leavitt, D. Englund, and E. Waks, *Hybrid integration of solid-state quantum emitters on a silicon photonic chip,* Nano Letters **17**, 7394 (2017).

[31] M. Churaev, R. N. Wang, A. Riedhauser, V. Snigirev, T. Blésin, C. Möhl, M. H. Anderson, A. Siddharth, Y. Popoff, U. Drechsler, *et al.*, *A heterogeneously integrated lithium niobate-on-silicon nitride photonic platform,* Nature Communications **14**, 3499 (2023).

[32] Y. Jiang, X. Han, H. Huang, P. Zhang, A. Dubey, H. Xiao, M. Yuan, A. Frigg, T. G. Nguyen, A. Boes, *et al.*, *Monolithic photonic integrated circuit based on silicon nitride and lithium niobate on insulator hybrid platform,* Advanced Photonics Research **3**, 2200121 (2022).

[33] Z. Wang, G. Chen, Z. Ruan, R. Gan, P. Huang, Z. Zheng, L. Lu, J. Li, C. Guo, K. Chen, *et al.*, *Silicon–lithium niobate hybrid intensity and coherent modulators using a periodic capacitively loaded traveling-wave electrode,* Acs Photonics **9**, 2668 (2022).

[34] R. Krishna, T. Fan, A. H. Hosseinnia, X. Wu, Z. Peng, and A. Adibi, *Hybrid 3c-silicon carbide-lithium niobate integrated photonic platform,* Optics Express **32**, 14555 (2024).

[35] Z. Li, N. Sharma, B. Lopez-Rodriguez, R. van der Kolk, T. Scholte, H. Voncken, J. van der Boom, S. Gröblacher, and I. E. Zadeh, *Heterogeneous integration of amorphous silicon carbide on thin film lithium niobate,* APL Photonics **10, 1** (2025).

[36] Y. Wang, K. D. Jöns, and Z. Sun, *Integrated photon-pair sources with nonlinear optics,* Applied Physics Reviews **8, 1** (2021).

[37] J. Komma, C. Schwarz, G. Hofmann, D. Heinert, and R. Nawrodt, *Thermo-optic coefficient of silicon at 1550 nm and cryogenic temperatures,* Applied Physics Letters **101, 4** (2012).

[38] M. W. Puckett, K. Liu, N. Chauhan, Q. Zhao, N. Jin, H. Cheng, J. Wu, R. O. Behunin, P. T. Rakich, K. D. Nelson, *et al.*, *422 million intrinsic quality factor planar integrated all-waveguide resonator with sub-mhz linewidth,* Nature Communications **12**, 934 (2021).

[39] A. W. Elshaari, I. E. Zadeh, K. D. Jöns, and V. Zwiller, *Thermo-optic characterization of silicon nitride resonators for cryogenic photonic circuits,* IEEE Photonics Journal **8**, 1 (2016).

[40] R. W. Boyd, A. L. Gaeta, and E. Giese, *Nonlinear optics,* in *Springer Handbook of Atomic, Molecular, and Optical Physics* (Springer, 2008) pp. 1097–1110.

[41] M. Dvorak and B. Justus, *Z-scan studies of nonlinear absorption and refraction in bulk, undoped inp,* Optics Communications **114**, 147 (1995).

[42] F. G. Della Corte, G. Cocorullo, M. Iodice, and I. Rendina, *Temperature dependence of the thermo-optic coefficient of inp, gaas, and sic from room temperature to 600 k at the wavelength of 1.5 μm,* Applied Physics Letters **77**, 1614 (2000).

[43] J.-P. Koester, H. Wenzel, J. Fricke, M. Reggentin, P. Della Casa, P. Sammeta, O. Brox, M. Ekterai, M. Kohlbrenner, A. Renkewitz, *et al.*, *Gaas-based photonic integrated circuit platform enabling monolithic ring-resonator-coupled lasers,* APL Photonics **9, 10** (2024).

[44] R. Gao, N. Yao, J. Guan, L. Deng, J. Lin, M. Wang, L. Qiao, W. Fang, and Y. Cheng, *Lithium niobate microring with ultra-high q factor above 10ˆ 8,* Chinese Optics Letters **20**, 011902 (2022).

[45] C. Wang, Z. Fang, A. Yi, B. Yang, Z. Wang, L. Zhou, C. Shen, Y. Zhu, Y. Zhou, R. Bao, *et al.*, *High-q microresonators on 4h-silicon-carbide-on-insulator platform for nonlinear photonics,* Light: Science & Applications **10**, 139 (2021).

[46] S. Rao, E. D. Mallemace, G. Cocorullo, G. Faggio, G. Messina, and F. G. Della Corte, *Temperature dependence of the thermo-optic coefficient in 4h-sic and gan slabs at the wavelength of 1550 nm,* Scientific Reports **12**, 4809 (2022).

[47] H. Sato, M. Abe, I. Shoji, J. Suda, and T. Kondo, *Accurate measurements of second-order nonlinear optical coefficients of 6h and 4h silicon carbide,* Journal of the Optical Society of America B **26**, 1892 (2009).

[48] P. Xing, D. Ma, K. J. Ooi, J. W. Choi, A. M. Agarwal, and D. Tan, *Cmos-compatible pecvd silicon carbide platform for linear and nonlinear optics,* ACS Photonics **6**, 1162 (2019).

[49] B. Lopez-Rodriguez, R. Van Der Kolk, S. Aggarwal, N. Sharma, Z. Li, D. Van Der Plaats, T. Scholte, J. Chang, S. Groeblacher, S. F. Pereira, *et al.*, *High-quality amorphous silicon carbide for hybrid photonic integration deposited at a low temperature,* ACS Photonics **10**, 3748 (2023).

[50] A. S. Tong, W. W. Chung, C. Goh, L. Y. Tobing, L. W. Lim, Y. A. Akimov, Z. J. Quek, A. P. Anthur, J. S. Goh, H. Lin, *et al.*, *1 million intrinsic q-factor microring resonators from pvd aluminum nitride on sio 2-on-si substrate,* in *2024 Optical Fiber Communications Conference and Exhibition (OFC)* (IEEE, 2024) pp. 1–3.

[51] X. Liu, C. Sun, B. Xiong, L. Wang, J. Wang, Y. Han, Z. Hao, H. Li, Y. Luo, J. Yan, *et al.*, *Aluminum nitride-on-sapphire platform for integrated high-q microresonators,* Optics Express **25**, 587 (2017).

[52] N. Li, C. P. Ho, S. Zhu, Y. H. Fu, Y. Zhu, and L. Y. T. Lee, *Aluminium nitride integrated photonics: a review,* Nanophotonics **10**, 2347 (2021).

[53] L. Chrostowski and M. Hochberg, *Silicon photonics design: from devices to systems* (Cambridge University Press, 2015).

[54] D. Melati, A. Melloni, and F. Morichetti, *Real photonic waveguides: guiding light through imperfections,* Advances in Optics and Photonics **6**, 156 (2014).

[55] S. Irfan, J.-Y. Kim, and H. Kurt, *Ultra-compact and efficient photonic waveguide bends with different configurations designed by topology optimization,* Scientific Reports **14**, 6453 (2024).

[56] L. Su, R. Trivedi, N. V. Sapra, A. Y. Piggott, D. Vercruysse, and J. Vuckovic, *Fully-automated optimization of grating couplers,* Optics Express **26**, 4023 (2018).

[57] R. Marchetti, C. Lacava, A. Khokhar, X. Chen, I. Cristiani, D. J. Richardson, G. T. Reed, P. Petropoulos, and P. Minzioni, *High-efficiency grating-couplers: demonstration of a new design strategy,* Scientific Reports **7**, 16670 (2017).

[58] X. Mu, S. Wu, L. Cheng, and H. Fu, *Edge couplers in silicon photonic integrated circuits: A review,* Applied Sciences **10**, 1538 (2020).

[59] X. Li, S. Yu, and C. Gui, *Fiber-to-chip three-dimensional silicon-on-insulator edge couplers with high efficiency and tolerance,* Micromachines **14**, 1500 (2023).

[60] N. L. Kazanskiy, S. N. Khonina, and M. A. Butt, *A review of photonic sensors based on ring resonator structures: three widely used platforms and implications of sensing applications,* Micromachines **14**, 1080 (2023).

[61] S. Hu and S. M. Weiss, *Design of photonic crystal cavities for extreme light concentration,* ACS Photonics **3**, 1647 (2016).

[62] Z. Lin and W. Shi, *Broadband, low-loss silicon photonic y-junction with an arbitrary power splitting ratio,* Optics Express **27**, 14338 (2019).

[63] A. Maese-Novo, R. Halir, S. Romero-Garcia, D. Perez-Galacho, L. Zavargo-Peche, A. Ortega-Monux, I. Molina-Fernandez, J. Wanguemert-Perez, and P. Cheben, *Wavelength independent multimode interference coupler,* Optics Express **21**, 7033 (2013).

[64] H. Sun, Q. Qiao, Q. Guan, and G. Zhou, *Silicon photonic phase shifters and their applications: A review,* Micromachines **13**, 1509 (2022).

[65] A. W. Elshaari, E. Bu¨yu¨ko¨zer, I. E. Zadeh, T. Lettner, P. Zhao, E. Scho¨ll, S. Gyger, M. E. Reimer, D. Dalacu, P. J. Poole, *et al.*, *Strain-tunable quantum integrated photonics,* Nano Letters **18**, 7969 (2018).

[66] S. Liu, J. Feng, Y. Tian, H. Zhao, L. Jin, B. Ouyang, J. Zhu, and J. Guo, *Thermo-optic phase shifters based on silicon-on-insulator platform: state-of-the-art and a review,* Frontiers of Optoelectronics **15**, 9 (2022).

[67] G. Sinatkas, T. Christopoulos, O. Tsilipakos, and E. E. Kriezis, *Electro-optic modulation in integrated photonics,* Journal of Applied Physics **130, 1** (2021).

[68] S. Hou, H. Hu, Z. Liu, W. Xing, J. Zhang, and Y. Hao, *High-speed electro-optic modulators based on thin-film lithium niobate,* Nanomaterials **14**, 867 (2024).

[69] N. Quack, H. Sattari, A. Y. Takabayashi, Y. Zhang, P. Verheyen, W. Bogaerts, P. Edinger, C. Errando-Herranz, and K. B. Gylfason, *Mems-enabled silicon photonic integrated devices and circuits,* IEEE Journal of Quantum Electronics **56**, 1 (2019).

[70] C. Errando-Herranz, A. Y. Takabayashi, P. Edinger, H. Sattari, K. B. Gylfason, and N. Quack, *Mems for photonic integrated circuits,* IEEE Journal of Selected Topics in Quantum Electronics **26**, 1 (2019).

[71] S. Gyger, J. Zichi, L. Schweickert, A. W. Elshaari, S. Steinhauer, S. F. Covre da Silva, A. Rastelli, V. Zwiller, K. D. Jöns, and C. Errando-Herranz, *Reconfigurable photonics with on-chip single-photon detectors,* Nature Communications **12**, 1408 (2021).

[72] A. W. Elshaari, I. E. Zadeh, A. Fognini, M. E. Reimer, D. Dalacu, P. J. Poole, V. Zwiller, and K. D. Jöns, *On-chip single photon filtering and multiplexing in hybrid quantum photonic circuits,* Nature communications **8**, 379 (2017).

[73] A. Senichev, Z. O. Martin, S. Peana, D. Sychev, X. Xu, A. S. Lagutchev, A. Boltasseva, and V. M. Shalaev, *Room-temperature single-photon emitters in silicon nitride,* Science Advances **7**, eabj0627 (2021).

[74] A. Senichev, S. Peana, Z. O. Martin, O. Yesilyurt, D. Sychev, A. S. Lagutchev, A. Boltasseva, and V. M. Shalaev, *Silicon nitride waveguides with intrinsic single-photon emitters for integrated quantum photonics,* ACS Photonics **9**, 3357 (2022).

[75] S. F. C. da Silva, G. Undeutsch, B. Lehner, S. Manna, T. M. Krieger, M. Reindl, C. Schimpf, R. Trotta, and A. Rastelli, *Gaas quantum dots grown by droplet etching epitaxy as quantum light sources,* Applied Physics Letters **119** (2021).

[76] C. Wang, C. Langrock, A. Marandi, M. Jankowski, M. Zhang, B. Desiatov, M. M. Fejer, and M. Lončar, *Ultrahigh-efficiency wavelength conversion in nanophotonic periodically poled lithium niobate waveguides,* Optica **5**, 1438 (2018).

[77] X. Shi, S. S. Mohanraj, V. Dhyani, A. A. Baiju, S. Wang, J. Sun, L. Zhou, A. Paterova, V. Leong, and D. Zhu, *Efficient photon-pair generation in layer-poled lithium niobate nanophotonic waveguides,* Light: Science & Applications **13**, 282 (2024).

[78] Y. Yonezu, K. Wakui, K. Furusawa, M. Takeoka, K. Semba, and T. Aoki, *Efficient single-photon coupling from a nitrogen-vacancy center embedded in a diamond nanowire utilizing an optical nanofiber,* Scientific reports **7**, 12985 (2017).

[79] M. E. Bathen and L. Vines, *Manipulating single-photon emission from point defects in diamond and silicon carbide,* Advanced Quantum Technologies **4**, 2100003 (2021).

[80] S. Castelletto, *Silicon carbide single-photon sources: challenges and prospects,* Materials for Quantum Technology **1**, 023001 (2021).

[81] P. T. Ramírez, J. D. Gómez, G. R. Becerra, R. Ramírez-Alarcón, M. G. Robles, and R. Salas-Montiel, *Integrated photon pairs source in silicon carbide based on micro-ring resonators for quantum storage at telecom wavelengths,* Scientific Reports **14**, 17755 (2024).

[82] L. Zeng, S. Zhang, J. Meng, J. Chen, J. Jiang, Y. Shi, J. Huang, Z. Yin, J. Wu, and X. Zhang, *Single-photon emission from point defects in hexagonal boron nitride induced by plasma treatment,* ACS Applied Materials & Interfaces **16**, 24899 (2024).

[83] A. B. D.-a.-j.-w.-i. Shaik and P. Palla, *Optical quantum technologies with hexagonal boron nitride single photon sources,* Scientific reports **11**, 12285 (2021).

[84] G.-L. Liu, X.-Y. Wu, P.-T. Jing, Z. Cheng, D. Zhan, Y. Bao, J.-X. Yan, H. Xu, L.-G. Zhang, B.-H. Li, *et al.*, *Single photon emitters in hexagonal boron nitride fabricated by focused helium ion beam,* Advanced Optical Materials **12**, 2302083 (2024).

[85] C. Serati de Brito, B. L. Rosa, A. Chaves, C. Cavalini, C. R. Rabahi, D. F. Franco, M. Nalin, I. D. Barcelos, S. Reitzenstein, and Y. G. Gobato, *Probing the nature of single-photon emitters in a wse2 monolayer by magneto-photoluminescence spectroscopy,* Nano Letters **24**, 13300 (2024).

[86] C. Errando-Herranz, E. Scho¨ll, R. Picard, M. Laini, S. Gyger, A. W. Elshaari, A. Branny, U. Wennberg, S. Barbat, T. Renaud, *et al.*, *Resonance fluorescence from waveguide-coupled, strain-localized, two-dimensional quantum emitters,* ACS photonics **8**, 1069 (2021).

[87] M. K. Akhlaghi, E. Schelew, and J. F. Young, *Waveguide integrated superconducting single-photon detectors implemented as near-perfect absorbers of coherent radiation,* Nature communications **6**, 8233 (2015).

[88] F. Marsili, V. B. Verma, J. A. Stern, S. Harrington, A. E. Lita, T. Gerrits, I. Vayshenker, B. Baek, M. D. Shaw, R. P. Mirin, *et al.*, *Detecting single infrared photons with 93% system efficiency,* Nature Photonics **7**, 210 (2013).

[89] I. Esmaeil Zadeh, J. W. Los, R. B. Gourgues, J. Chang, A. W. Elshaari, J. R. Zichi, Y. J. Van Staaden, J. P. Swens, N. Kalhor, A. Guardiani, *et al.*, *Efficient single-photon detection with 7.7 ps time resolution for photon-correlation measurements,* Acs Photonics **7**, 1780 (2020).

[90] B. Korzh, Q.-Y. Zhao, J. P. Allmaras, S. Frasca, T. M. Autry, E. A. Bersin, A. D. Beyer, R. M. Briggs, B. Bumble, M. Colangelo, *et al.*, *Demonstration of sub-3 ps temporal resolution with a superconducting nanowire single-photon detector,* Nature Photonics **14**, 250 (2020).

[91] S. Ferrari, C. Schuck, and W. Pernice, *Waveguide-integrated superconducting nanowire single-photon detectors,* Nanophotonics **7**, 1725 (2018).

[92] I. Esmaeil Zadeh, J. Chang, J. W. Los, S. Gyger, A. W. Elshaari, S. Steinhauer, S. N. Dorenbos, and V. Zwiller, *Superconducting nanowire single-photon detectors: A perspective on evolution, state-of-the-art, future developments, and applications,* Applied Physics Letters **118, 19** (2021).

[93] W. H. Pernice, C. Schuck, O. Minaeva, M. Li, G. Goltsman, A. Sergienko, and H. Tang, *High-speed and high-efficiency travelling wave single-photon detectors embedded in nanophotonic circuits,* Nature Communications **3**, 1325 (2012).

[94] C. Schuck, W. H. Pernice, O. Minaeva, M. Li, G. Gol'Tsman, A. V. Sergienko, and H. X. Tang, *Matrix of integrated superconducting single-photon detectors with high timing resolution,* IEEE transactions On Applied Superconductivity **23, 3**, 2201007 (2013).

[95] A. Vetter, S. Ferrari, P. Rath, R. Alaee, O. Kahl, V. Kovalyuk, S. Diewald, G. N. Goltsman, A. Korneev, C. Rockstuhl, *et al.*, *Cavity-enhanced and ultrafast superconducting single-photon detectors,* Nano Letters **16**, 7085 (2016).

[96] S. Buckley, J. Chiles, A. N. McCaughan, G. Moody, K. L. Silverman, M. J. Stevens, R. P. Mirin, S. W. Nam, and J. M. Shainline, *All-silicon light-emitting diodes waveguide-integrated with superconducting single-photon detectors,* Applied Physics Letters **111, 14** (2017).

[97] J. Li, R. A. Kirkwood, L. J. Baker, D. Bosworth, K. Erotokritou, A. Banerjee, R. M. Heath, C. M. Natarajan, Z. H. Barber, M. Sorel, *et al.*, *Nano-optical single-photon response mapping of waveguide integrated molybdenum silicide (mosi) superconducting nanowires,* Optics Express **24**, 13931 (2016).

[98] O. Kahl, S. Ferrari, V. Kovalyuk, A. Vetter, G. Lewes-Malandrakis, C. Nebel, A. Korneev, G. Goltsman, and W. Pernice, *Spectrally multiplexed single-photon detection with hybrid superconducting nanophotonic circuits,* Optica **4**, 557 (2017).

[99] O. Kahl, S. Ferrari, V. Kovalyuk, G. N. Goltsman, A. Korneev, and W. H. Pernice, *Waveguide integrated superconducting single-photon detectors with high internal quantum efficiency at telecom wavelengths,* Scientific Reports **5**, 10941 (2015).

[100] S. Ferrari, O. Kahl, V. Kovalyuk, G. N. Goltsman, A. Korneev, and W. H. Pernice, *Waveguide-integrated single-and multi-photon detection at telecom wavelengths using superconducting nanowires,* Applied Physics Letters **106, 15** (2015).

[101] C. Schuck, W. H. Pernice, X. Ma, and H. X. Tang, *Optical time domain reflectometry with low noise waveguide-coupled superconducting nanowire single-photon detectors,* Applied Physics Letters **102, 19** (2013).

[102] C. Schuck, X. Guo, L. Fan, X. Ma, M. Poot, and H. X. Tang, *Quantum interference in heterogeneous superconducting-photonic circuits on a silicon chip,* Nature Communications **7**, 10352 (2016).

[103] C. Schuck, W. H. Pernice, and H. X. Tang, *Waveguide integrated low noise nbtin nanowire single-photon detectors with milli-hz dark count rate,* Scientific Reports **3**, 1893 (2013).

[104] A. D. Beyer, R. M. Briggs, F. Marsili, J. D. Cohen, S. M. Meenehan, O. J. Painter, and M. D. Shaw, *Waveguide-coupled superconducting nanowire single-photon detectors,* in *2015 Conference on Lasers and Electro-Optics (CLEO)* (IEEE, 2015) pp. 1–2.

[105] J. M. Shainline, S. M. Buckley, N. Nader, C. M. Gentry, K. C. Cossel, J. W. Cleary, M. Popović, N. R. Newbury, S. W. Nam, and R. P. Mirin, *Room-temperature-deposited dielectrics and superconductors for integrated photonics,* Optics Express **25**, 10322 (2017).

[106] J. Sprengers, A. Gaggero, D. Sahin, S. Jahanmirinejad, G. Frucci, F. Mattioli, R. Leoni, J. Beetz, M. Lermer, M. Kamp, *et al.*, *Waveguide superconducting single-photon detectors for integrated quantum photonic circuits,* Applied Physics Letters **99, 18** (2011).

[107] S. Jahanmirinejad, G. Frucci, F. Mattioli, D. Sahin, A. Gaggero, R. Leoni, and A. Fiore, *Photon-number resolving detector based on a series array of superconducting nanowires,* Applied Physics Letters **101, 7** (2012).

[108] D. Sahin, A. Gaggero, Z. Zhou, S. Jahanmirinejad, F. Mattioli, R. Leoni, J. Beetz, M. Lermer, M. Kamp, S. Höfling, *et al.*, *Waveguide photon-number-resolving detectors for quantum photonic integrated circuits,* Applied Physics Letters **103, 11** (2013).

[109] G. Reithmaier, M. Kaniber, F. Flassig, S. Lichtmannecker, K. Mu¨ller, A. Andrejew, J. Vuckovic, R. Gross, and J. Finley, *On-chip generation, routing, and detection of resonance fluorescence,* Nano Letters **15**, 5208 (2015).

[110] G. E. Digeronimo, M. Petruzzella, S. Birindelli, R. Gaudio, S. Fattah Poor, F. W. Van Otten, and A. Fiore, *Integration of single-photon sources and detectors on gaas,* in *Photonics*, Vol. 3 (MDPI, 2016) p. 55.

[111] M. Kaniber, F. Flassig, G. Reithmaier, R. Gross, and J. J. Finley, *Integrated superconducting detectors on semiconductors for quantum optics applications,* Applied Physics B **122**, 1 (2016).

[112] F. Najafi, J. Mower, N. C. Harris, F. Bellei, A. Dane, C. Lee, X. Hu, P. Kharel, F. Marsili, S. Assefa, *et al.*, *On-chip detection of non-classical light by scalable integration of single-photon detectors,* Nature Communications **6**, 5873 (2015).

[113] M. Tanner, L. S. E. Alvarez, W. Jiang, R. Warburton, Z. Barber, and R. Hadfield, *A superconducting nanowire single photon detector on lithium niobate,* Nanotechnology **23**, 505201 (2012).

[114] A. A. Sayem, R. Cheng, S. Wang, and H. X. Tang, *Lithium-niobate-on-insulator waveguide-integrated superconducting nanowire single-photon detectors,* Applied Physics Letters **116, 15** (2020).

[115] M. A. Wolff, S. Vogel, L. Splitthoff, and C. Schuck, *Superconducting nanowire single-photon detectors integrated with tantalum pentoxide waveguides,* Scientific Reports **10**, 17170 (2020).

[116] O. Kahl, S. Ferrari, P. Rath, A. Vetter, C. Nebel, and W. H. Pernice, *High efficiency on-chip single-photon detection for diamond nanophotonic circuits,* Journal of Lightwave Technology **34**, 249 (2016).

[117] P. Rath, O. Kahl, S. Ferrari, F. Sproll, G. Lewes-Malandrakis, D. Brink, K. Ilin, M. Siegel, C. Nebel, and W. Pernice, *Superconducting single-photon detectors integrated with diamond nanophotonic circuits,* Light: Science & Applications **4**, e338 (2015).

[118] H. A. Atikian, S. Meesala, M. J. Burek, Y.-I. Sohn, J. Israelian, A. S. Patri, N. Clarke, A. Sipahigil, R. E. Evans, D. Sukachev, *et al.*, *Novel fabrication of diamond nanophotonics coupled to single-photon detectors,* SPIE Newsroom (2017).

[119] G. Terrasanta, M. W. Ziarko, N. Bergamasco, M. Poot, and J. Poliak, *Photonic integrated circuits for optical satellite links: A review of the technology status and space effects,* International Journal of Satellite Communications and Networking (2025).

[120] P. Sibson, C. Erven, M. Godfrey, S. Miki, T. Yamashita, M. Fujiwara, M. Sasaki, H. Terai, M. G. Tanner, C. M. Natarajan, *et al.*, *Chip-based quantum key distribution,* Nature Communications **8**, 13984 (2017).

[121] F. Beutel, H. Gehring, M. A. Wolff, C. Schuck, and W. Pernice, *Detector-integrated on-chip qkd receiver for ghz clock rates,* npj Quantum Information **7**, 40 (2021).

[122] Q. Liu, Y. Huang, Y. Du, Z. Zhao, M. Geng, Z. Zhang, and K. Wei, *Advances in chip-based quantum key distribution,* Entropy **24**, 1334 (2022).

[123] E. Knill, R. Laflamme, and G. J. Milburn, *A scheme for efficient quantum computation with linear optics,* nature **409**, 46 (2001).

[124] A. Crespi, R. Ramponi, R. Osellame, L. Sansoni, I. Bongioanni, F. Sciarrino, G. Vallone, and P. Mataloni, *Integrated photonic quantum gates for polarization qubits,* Nature Communications **2**, 566 (2011).

[125] H. Aghaee Rad, T. Ainsworth, R. Alexander, B. Altieri, M. Askarani, R. Baby, L. Banchi, B. Baragiola, J. Bourassa, R. Chadwick, *et al.*, *Scaling and networking a modular photonic quantum computer,* Nature, 1-8 (2025).

[126] M. Moralis-Pegios, G. Giamougiannis, A. Tsakyridis, D. Lazovsky, and N. Pleros, *Perfect linear optics using silicon photonics,* Nature Communications **15**, 5468 (2024).

[127] S. Slussarenko and G. J. Pryde, *Photonic quantum information processing: A concise review,* Applied Physics Reviews **6, 4** (2019).

[128] R. Nagy, M. Niethammer, M. Widmann, Y.-C. Chen, P. Udvarhelyi, C. Bonato, J. U. Hassan, R. Karhu, I. G. Ivanov, N. T. Son, *et al.*, *High-fidelity spin and optical control of single silicon-vacancy centres in silicon carbide,* Nature Communications **10**, 1954 (2019).

[129] S. Ecker, M. Fink, T. Scheidl, P. Sohr, R. Ursin, M. J. Arshad, C. Bonato, P. Cilibrizzi, A. Gali, P. Udvarhelyi, *et al.*, *Quantum communication networks with defects in silicon carbide,* arXiv preprint arXiv:2403.03284 (2024).

[130] S. Saravi, T. Pertsch, and F. Setzpfandt, *Lithium niobate on insulator: an emerging platform for integrated quantum photonics,* Advanced Optical Materials **9**, 2100789 (2021).

[131] M. Clementi, F. A. Sabattoli, M. Borghi, L. Gianini, N. Tagliavacche, H. El Dirani, L. Youssef, N. Bergamasco, C. Petit-Etienne, E. Pargon, *et al.*, *Programmable frequency-bin quantum states in a nano-engineered silicon device,* Nature Communications **14**, 176 (2023).

[132] A. Mueller, S. I. Davis, B. Korzh, R. Valivarthi, A. D. Beyer, R. Youssef, N. Sinclair, C. Peña, M. D. Shaw, and M. Spiropulu, *High-rate multiplexed entanglement source based on time-bin qubits for advanced quantum networks,* Optica Quantum **2**, 64 (2024).

[133] T. P. McKenna, H. S. Stokowski, V. Ansari, J. Mishra, M. Jankowski, C. J. Sarabalis, J. F. Herrmann, C. Langrock, M. M. Fejer, and A. H. Safavi-Naeini, *Ultra-low-power second-order nonlinear optics on a chip,* Nature Communications **13**, 4532 (2022).

[134] S. Liu, Y. Zheng, and X. Chen, *Cascading second-order nonlinear processes in a lithium niobate-on-insulator microdisk,* Optics Letters **42**, 3626 (2017).

[135] J. Li, Q. Zhang, J. Wang, and A. W. Poon, *An integrated 3c-silicon carbide-on-insulator photonic platform for nonlinear and quantum light sources,* Communications Physics **7**, 125 (2024).

[136] J. Yang, M. Guidry, D. Lukin, K. Yang, and J. Vuckovic, *Inverse-designed silicon carbide quantum and nonlinear photonics light sci,* in *Appl*, Vol. 12 (2023) p. 201.

[137] A. A. Afridi, Y. Lu, X. Shi, R. Wang, J. Li, Q. Li, and H. Ou, *4h-sic microring resonators—opportunities for nonlinear integrated optics,* Applied Physics Letters **124, 17** (2024).

[138] K. Alexander, A. Bahgat, A. Benyamini, D. Black, D. Bonneau, S. Burgos, B. Burridge, G. Campbell, G. Catalano, A. Ceballos, *et al.*, *A manufacturable platform for photonic quantum computing,* arXiv preprint arXiv:2404.17570 (2024).

[139] C. V. Poulton, A. Yaacobi, D. B. Cole, M. J. Byrd, M. Raval, D. Vermeulen, and M. R. Watts, *Coherent solid-state lidar with silicon photonic optical phased arrays,* Optics Letters **42**, 4091 (2017).

[140] X. Zhang, K. Kwon, J. Henriksson, J. Luo, and M. C. Wu, *A large-scale microelectromechanical-systems-based silicon photonics lidar,* Nature **603**, 253 (2022).

[141] A. Lukashchuk, H. K. Yildirim, A. Bancora, G. Lihachev, Y. Liu, Z. Qiu, X. Ji, A. Voloshin, S. A. Bhave, E. Charbon, *et al.*, *Photonic-electronic integrated circuit-based coherent lidar engine,* Nature Communications **15**, 3134 (2024).

[142] M. Peyrou, *Design and testing of hybrid InP/Si photonic integrated components/circuits for LIDAR applications,* Ph.D. thesis, Université Grenoble Alpes [2020-2023] (2023).

[143] D. J. Lum, S. H. Knarr, and J. C. Howell, *Frequency-modulated continuous-wave lidar compressive depth-mapping,* Optics Express **26**, 15420 (2018).

[144] H. Altug, S.-H. Oh, S. A. Maier, and J. Homola, *Advances and applications of nanophotonic biosensors,* Nature Nanotechnology **17**, 5 (2022).

[145] D. Pohl, M. Reig Escale, M. Madi, F. Kaufmann, P. Brotzer, A. Sergeyev, B. Guldimann, P. Giaccari, E. Alberti, U. Meier, *et al.*, *An integrated broadband spectrometer on thin-film lithium niobate,* Nature Photonics **14**, 24 (2020).

[146] M. C. Estevez, M. Alvarez, and L. M. Lechuga, *Integrated optical devices for lab-on-a-chip biosensing applications,* Laser & Photonics Reviews **6**, 463 (2012).

[147] W. J. Westerveld, M. Mahmud-Ul-Hasan, R. Shnaiderman, V. Ntziachristos, X. Rottenberg, S. Severi, and V. Rochus, *Sensitive, small, broadband and scalable optomechanical ultrasound sensor in silicon photonics,* Nature Photonics **15**, 341 (2021).

[148] J. Pan, Q. Li, Y. Feng, R. Zhong, Z. Fu, S. Yang, W. Sun, B. Zhang, Q. Sui, J. Chen, *et al.*, *Parallel interrogation of the chalcogenide-based micro-ring sensor array for photoacoustic tomography,* Nature Communications **14**, 3250 (2023).

[149] A. Yi, C. Wang, L. Zhou, Y. Zhu, S. Zhang, T. You, J. Zhang, and X. Ou, *Silicon carbide for integrated photonics,* Applied Physics Reviews **9, 3** (2022).

[150] M. A. Guidry, K. Y. Yang, D. M. Lukin, A. Markosyan, J. Yang, M. M. Fejer, and J. Vučković, *Optical parametric oscillation in silicon carbide nanophotonics,* Optica **7**, 1139 (2020).

[151] M. A. Guidry, D. M. Lukin, K. Y. Yang, R. Trivedi, and J. Vučković, *Quantum optics of soliton microcombs,* Nature Photonics **16**, 52 (2022).

[152] K. Powell, A. Shams-Ansari, S. Desai, M. Austin, J. Deng, N. Sinclair, M. Lončar, and X. Yi, *High-q suspended optical resonators in 3c silicon carbide obtained by thermal annealing,* Optics Express **28**, 4938 (2020).

[153] T. Fan, H. Moradinejad, X. Wu, A. A. Eftekhar, and A. Adibi, *High-q integrated photonic microresonators on 3c-sic-on-insulator (sicoi) platform,* Optics Express **26**, 25814 (2018).

[154] R. Koscica, Y. Wan, W. He, M. Kennedy, and J. E. Bowers, *Heterogeneous integration of a iii–v quantum dot laser on high thermal conductivity silicon carbide,* Optics Letters **48**, 2539 (2023).

[155] Y. Zhu, W. Wei, A. Yi, T. Jin, C. Shen, X. Wang, L. Zhou, C. Wang, W. Ou, S. Song, *et al.*, *Hybrid integration of deterministic quantum dot-based single-photon sources with cmos-compatible silicon carbide photonics,* Laser & Photonics Reviews **16**, 2200172 (2022).

[156] X. Lu, J. Y. Lee, S. Rogers, and Q. Lin, *Optical kerr nonlinearity in a high-q silicon carbide microresonator,* Optics express **22**, 30826 (2014).

[157] P. Xing, D. Ma, L. C. Kimerling, A. M. Agarwal, and D. T. Tan, *High efficiency four wave mixing and optical bistability in amorphous silicon carbide ring resonators,* APL Photonics **5, 7** (2020).

[158] L.-Y. S. Chang, S. Pappert, and P. K. Yu, *High thermo-optic tunability in pecvd silicon-rich amorphous silicon carbide,* Optics Letters **48**, 1188 (2023).

[159] Y. Lu, X. Shi, A. Ali Afridi, Y. Wang, V. Tabouret, D. Chaussende, K. Rottwitt, and H. Ou, *Strong third-order nonlinearity in amorphous silicon carbide waveguides,* Optics Letters **49**, 4389 (2024).

[160] P. O. Weigel and S. Mookherjea, *Design of folded hybrid silicon carbide-lithium niobate waveguides for efficient second-harmonic generation,* Journal of the Optical Society of America B **35**, 593 (2018).

3

EXPERIMENTAL METHODS

This chapter will provide a more in detail and visual overview of the experimental methods that have been applied in this thesis. Specifically, the film deposition techniques, the fabrication processes for the photonic devices (ring resonators, waveguides and superconducting detectors) and the silicon dioxide lift-off processes. Additionally, a detailed explanation of the optical setups involved in the characterization experiments will be given, both at room temperature and cryogenic temperatures. The aim of this chapter is to serve as a manual for future students and researchers in the field.

3

3.1. DEPOSITION TECHNIQUES

In this thesis, we fabricate devices with two chemical vapor deposition techniques: PECVD and ICPCVD and, as a comparison, a schematic for the chambers of both systems is included below in fig.3.1. For PECVD, we used a Plasmalab 80+ while for the ICPCVD, we used a PlasmaPro100. PECVD has been utilized for silicon, silicon dioxide, silicon nitride and amorphous silicon carbide deposition [1–8], being the more conventional deposition technique for photonic devices. On the other hand, ICPCVD is a newer method to yield high quality and high density films with low hydrogen incorporation for similar materials [9–15].

ICPCVD offers a lower operation temperature than PECVD, allowing to integrate the silicon carbide films with CMOS processes and with III-V materials, which are very sensitive to higher temperatures. The films provided by ICPCVD present higher density and therefore higher refractive index with a lower deposition temperature, improving the light confinement together with low hydrogen incorporation that reduces optical losses. In PECVD (fig.3.1a), the bias between the parallel plates is coupled to the forward plasma power. On the other hand, ICPCVD (fig.3.1b) has a plasma that is inductively coupled, making it possible to achieve higher plasma densities without ion damage. As a result, the films obtained with ICPECVD present lower surface roughness than PECVD.

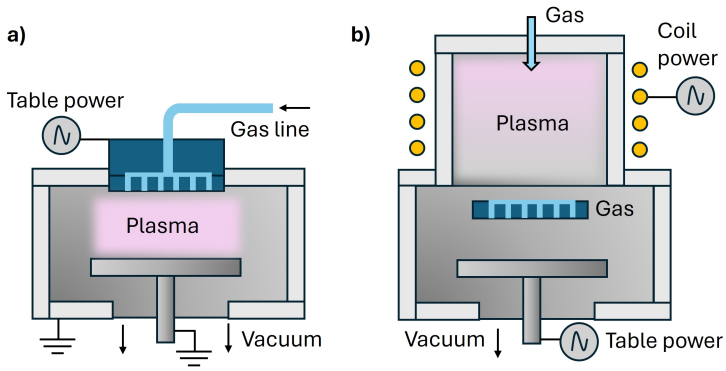

Figure 3.1: Chamber geometry in a a) PECVD and b) ICPCVD processes.

3.2. DEVICE FABRICATION

In the following chapters of the thesis that correspond to the different publications there are simplified fabrication flows that do not show specific processes. In this section, we will give an overview of the fabrication of photonic devices together with superconducting nanowire single photon detectors and the specific steps to achieve a high-quality silicon dioxide lift-off. Before giving the fabrication flow, there are some common concepts and recipes that we will describe below:

- **ICPCVD deposition of a-SiC:** the deposition is performed in a mixture of 15 sccm of silane (SiH_4), 10 sccm of methane (CH_4), 10 sccm of Argon (Ar) as carrier gas and 11 scmm of Ar close to the sample. The later is used to improve uniformity of the flows which directly impacts the film quality. The plasma power for the deposition is set to 750 W, the chamber pressure to 2 mTorr and the optimal deposition temperature is 150°C with 39 nm/min deposition rates.

- **ICPCVD deposition of SiO_2:** The deposition is performed in a mixture of 16 sccm of silane (SiH_4) and 60 sccm of nitrous oxide (N_2O). The plasma power for the deposition is set to 1300 W, the chamber pressure to 8 mTorr and the optimal deposition temperature is 150°C, achieving deposition rates of 60 nm/min.

- **Electron beam lithography:** this step is performed in a Raith EBPG 5200+ using an aperture of 400 μm and an acceleration voltage of 100 kV.

- **Reactive Ion Etching (RIE) in Sentech Etchlab 200:** for optical devices and SNSPDs we followed a similar ething recipe of 13.5 sccm of SF_6 and 3.5 sccm of O_2 at a RF power of 50W and chamber pressure of 8 μbar. Previous to the etching step, the chamber is cleaned using 200 sccm O_2 at 200W for 10 min and pre-conditioning the chamber for 5 min without the sample using the same etching recipe.

- **RIE descum in Sentech Etchlab 200:** only in the case of waveguide-based devices (not SNSPDs) and before depositing materials for lift-off processes, we remove the resist residues by performing an oxygen plasma cleaning step for 1 min with 200 sccm O_2 at 20 W of RF plasma power.

- **Markers, contact pads and heaters:** all three structures are patterned using the same positive resist PMMA 950K A6 spin-coated at 3000 rpm/min to achieve a thickness of around 600 nm and baked at 175°C for 1 min. An electron beam lithography step is followed with a dose of 1100-1300 $\mu C/cm^2$ to expose the patterns with a resolution and a beam step size of 64 nm and a beam spot size of around 100 nm. The development is performed in MBIK:IPA (1:3) for 1 min and IPA for 1 min and later the sample is dried using a nitrogen gun.

- **Lift-off:** is a step used to remove the material deposited on top of the resist and leave the gold markers, contact pads, micro-heaters or silicon dioxide. This step is performed in PRS3000 at 80°C overnight leaving the sample vertically in a holder and a magnetic stirrer.

- **Sample cleaning:** to remove chemical residues or particles from resist and redeposition, we always immerse the sample in acetone and IPA and dry it with a nitrogen gun. For the normal samples without SNSPDs, this is done 5 min for each in a sonication bath at power level of 9 (out of 9). For the SNSPD samples, we only immersed the samples since sonication can potentially harm the devices.

3.2.1. PHOTONIC DEVICES

During this thesis, we followed two approaches for the fabrication of photonic devices. The simpler one that gave us higher quality optical devices is described in **Chapter 4** and also used in **Chapter 5**. These devices are fabricated using a one-step lithography fabrication approach. We start by thermally oxidizing a silicon wafer to achieve a thickness of 2.5 μm SiO_2 and depositing 280 nm a-SiC using ICPCVD at 150°C. ARP-6200-09 positive resist is spin-coated at 2500 rpm-min and baked at 165°C for 1 min to remove the solvent. To define the pattern, we exposed the resist in an electron beam lithography tool. The design has a resolution and beam step size of 2 nm with a beam spot size of 3 nm. The optimal dose for this resist was found to be 280 $\mu C/cm^2$. To reveal the exposed region, the sample was developed 1 min in pentylacetate, 1 min in MBIK:IPA (1:1), 1 min in IPA and dried using a nitrogen gun. To transfer the pattern to the film, a RIE step was followed for 120 s. To remove the remaining resist residues, we performed a descum step for 500 s. As a final step, we spin coated PMMA 950K A7 resist to achieve a thickness of 1 μm or deposited a PECVD SiO_2. The devices are fabricated for both grating coupling configuration (fig.3.2a) and for a side coupling configuration (fig.3.2b) which will be discussed in the section **Device characterization**.

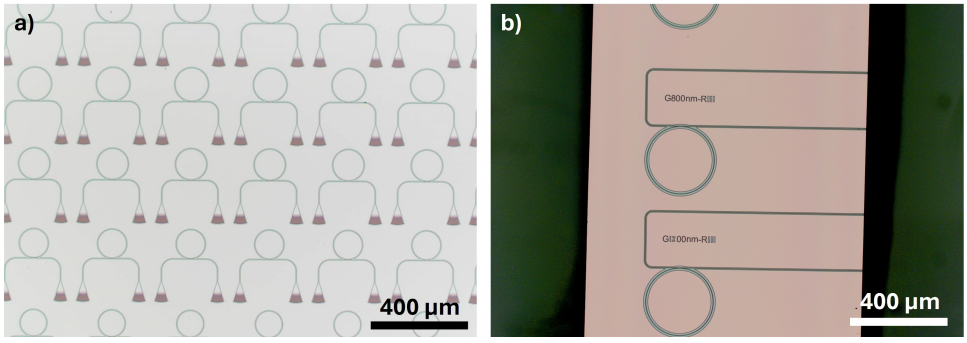

Figure 3.2: Optical devices fabricated using the standard ARP-6200-09 fabrication route on amorphous silicon carbide for a) grating coupler configuration and b) side coupling configuration.

For the integration of our a-SiC platform with superconducting detectors based on NbTiN films, we followed a standard fabrication process on silicon substrates with thermally oxidized silicon dioxide. A thin film of NbTiN film is deposited using DC Magnetron sputtering [16]. The first layer that we pattern are for the gold contact pads of the SNSPDs and the marker field for consecutive lithography steps. Before gold evaporation and to remove possible resist residues, we performed descum. The sample is then transferred to a metal evaporation tool where a layer of 5 nm of chromium is deposited

as a sticking layer and 80 nm of Au to define the pads and markers. Following this deposition, a lift-off process is done. After this, maN-2401 resist is spin-coated at a rate of 4000 rpm/min to achieve a final thickness of 100 nm. The resist is then baked at 90°C to remove the solvent and transferred to the electron beam lithography tool to expose the resist. The set resolution and beam step size (BSS) for this design is 2 nm, with a beam spot size of 3 nm. A dose test is performed to obtain an optimal dose of 300 μC/cm^2. Examples of scanning electron microscope images of lower doses are shown in fig.3.3. To reveal the pattern, we rinsed the sample in maD-525 for 1 min, deionized water for another minute and the sample was dried with a nitrogen gun. For a film thickness between 7 nm and 9 nm, the etching step is run for 40s. At this step, the devices are characterized to verify the performance and it will be reviewed in the section **Device characterization**. The remaining residues of resist are removed by immersing the sample in PRS3000 at 80°C for few hours and later the sample was cleaned. Immediately after this and to prevent the oxidation of the superconducting film, a 280 nm layer of a-SiC is deposited with ICPCVD. The optical ring resonators and waveguides were patterned using ARN-7520-17 negative resist with a dose of 500 μC/cm^2, developed using MF322 for 60s, twice in MF322:H_2O (1:10) for 15 s and tiwce in H_2O for 15s. We performed an etching step for 120 s and resist descum. An oxide lift-off step is performed following the same procedure that will be shown in **Silicon dioxide lift-off**. This is done to leave the markers open for the alignment of the microheater pattern. For the micro-heaters, we deposited 80 nm of titanium and 10 nm of gold, the later to reduce the resistance of the micro-heaters. To finalize, a lift-off step is performed and the sample is cleaned.

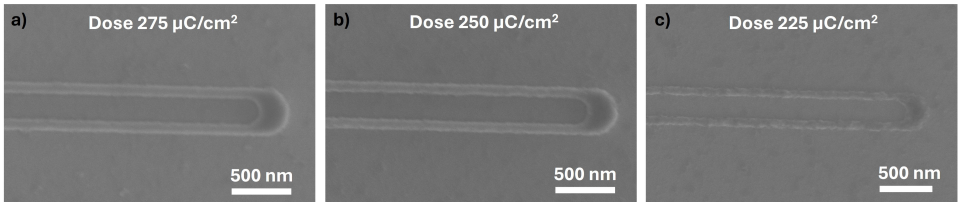

Figure 3.3: Effect of different electron beam doses in maN-2401 resist defining a wire for SNSNPDs, using doses of a) 275 μC/cm^2, b) 250 μC/cm^2 and c) 225 μC/cm^2

3.2.2. SILICON DIOXIDE LIFT-OFF

The fabrication of the optical devices is similar to the previous section using ARP-6200-09 positive resist, including the marker layer for consecutive lithography steps. The sample is then spin-coated with PMMA 960K A11 at 2500 rpm/min for a thickness of 2.2 μm. We perform electron beam lithography and the openings are defined using a resolution of 64 nm, with beam step size of 64 nm and beam spot size of around 100 nm. The dose for this exposure was set to 1300 μC/cm^2. The development is similar to previous PMMA exposures. Afterwards, the most important step is to clean the resist residue with an descum step for 1 min. An optical microscope image of a device after this step is shown in fig.3.4a. The resist height is measured using a profilometer and the deposition of ICPCVD SiO_2 is done to achieve a thickness 200-300 nm lower than the resist thickness. Following the deposition, a lift-off step is performed with a magnetic stir-

rer overnight. The sample is then cleaned and a second opening is done to deposit the second cladding at the desired deposition conditions to achieve bidirectional thermal tunability. Metallic heaters are fabricated on top of the optical waveguides to tune the devices and the resulting device is shown in fig.3.4b.

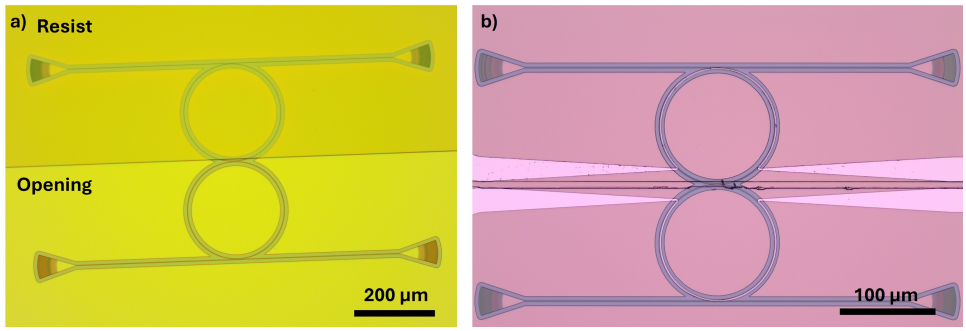

Figure 3.4: a) Resist opening prepared to deposit one of the silicon dioxide claddings and b) final device with two different claddings for bidirectional thermal tunability and metallic micro-heaters.

3.3. DEVICE CHARACTERIZATION

This section gives an overview of the specific components that have been fabricated and provides a detailed explanation of the optical setups that have been used in this thesis. To characterize the wavelength spectra of ring resonators, we assembled two setups for in-plane and grating coupling configurations. In addition, we included a thermal element and a printed circuit board (PCB) with electrical connections to measure thermal shifts and tune the devices using micro-heaters, respectively. To measure the superconducting nanowire single photon detectors, we performed the measurements at cryogenic temperatures in a Gifford-McMahon cryocooler. The PCB used for electrical connections (fig.3.5a) have 8 radio-frequency subminiature push-on (RF SMP) connectors (4 on each side) and 16 pin connectors (14 pins for signal and 2 for the common ground, 8 total connectors on each side).

3.3.1. ROOM TEMPERATURE SETUP

During the work presented in this thesis, the measurement setups at room temperature evolved to two different configurations: for grating coupling using single fibers and side coupling with v-groove fiber assemblies as depicted in fig.3.5b. The common elements for these setups are the tunable laser (Photonetics TUNICS-PRI 3642 HE 15), the DC voltage supply for electrical tuning of the optical devices (RIGOL model DP832A), the paddle polarization controllers (FPC560), the powermeters (818-IR Newport, linearity 0.5%), the free-space polarizer (FBR-LPNIR) and the U-bench (FB-51) with optical fiber collimators (FBP-C-FC). To measure the thermal response of the optical devices, the setups also have a customized sample base with a thermal element and a manual controller with a temperature sensor. A MATLAB Graphical User Interface (GUI) is used to control the laser, stages, powermeter and DC voltage supply and it is capable of obtaining data of trans-

mission spectra for a single ring at fixed temperature and voltage and transmission data at different applied voltages for ring resonators and MZIs. A general description of the setups is given below:

- **Grating coupling setup:** it consists of two XYZ micrometer stages from Thorlabs (MTB612D) and 3D printed magnetic fiber holders with the possibility to adjust the incidence angle. For automatic scanning, the sample stage has two Newport closed-loop piezo linear actuators (model 8310CE). The output light from the optical devices is collected using a multimode fiber. In this configuration, the MATLAB GUI can also automatize the stages to move from ring to ring, adjust the maximum coupling and acquire the transmission spectra. Therefore enabling overnight automatic measurements and data analysis. A close-up of the sample mount for this setup is shown in fig.3.5c.
- **Side coupling setup:** The setup has a 3D printed mount to hold a V-groove fiber assembly from OzOptics (wavelength 1550 nm, separation 250 μm). The sample stage has two Newport open loop linear piezoactuators (model 8302) for XY movement of the sample and the V-groove stage an additional one for the Z movement. The overall setup arrangement is shown in fig.3.5d.

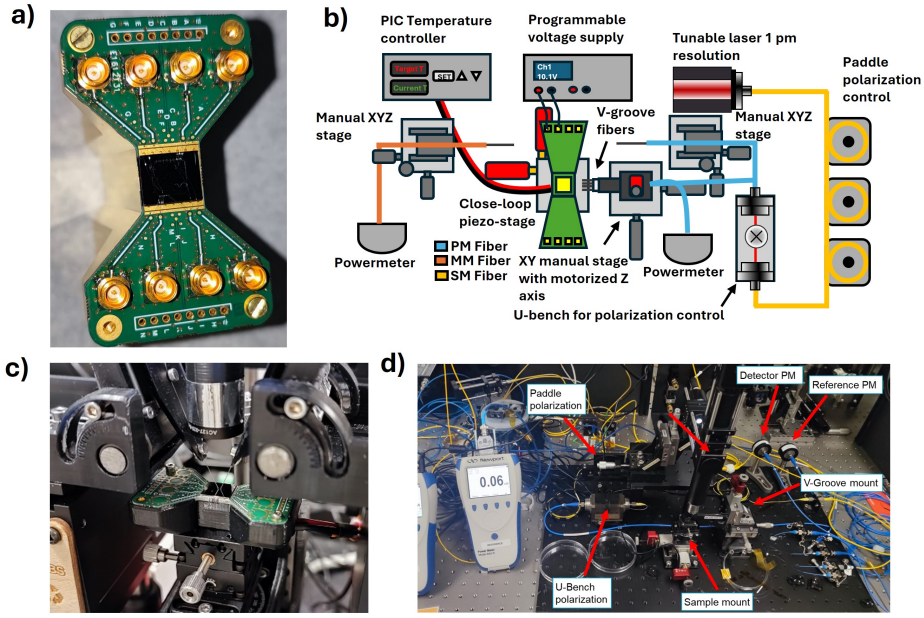

Figure 3.5: a) PCB used for the characterization of photonic devices at room temperature and cryogenics, b) schematic of the optical setup with both grating coupler and side coupling configuration. The setups are assembled separately from each other but with common components such as the tunable laser, a temperature controller, a programmable power supply and the polarization controllers; and they can be seen in c) sample stage for the grating coupling configuration and d) optical setup for side coupling configuration.

3.3.2. CRYOGENIC SETUP

Before further fabrication, the superconducting detectors are wire bonded and the resistance is measured at room temperature. If the values are in agreement with expected values and previously measured devices (around 1 MOhm in this thesis), the PCB is then mounted on the cryostat.

An overview of the optical setup to characterize the photonic devices with superconducting detectors is shown in fig.3.6. The cryostat has an open window for imaging and optical access to be able to couple light into the devices. The imaging system consists of a charge-coupled device (CCD) camera with a movable lens for infinity correction and a fixed lens in the cryostat. The assembly also has an illumination path with a light emitting diode (LED, Thorlabs LIUCWHA) and a fiber collimator (Newport F-C5-F2-1550) to inject light coming from the laser. The cryostat has two thermal radiation shields to achieve low temperatures and an external shield for vacuum. The second shield has a temperature of about 40K and holds cryogenic amplifiers to improve the signal-to-noise ratio of the detection events, while the third shield of the sample stage keeps a temperature of 2.8- 3.2 K. In the PCB stage, there are SMP connections to electrically access the devices and several optical fibers in the case of having to characterize the detectors with flood illumination or with self-aligned fiber sleeves. To bias the detectors and retrieve the photon pulses, the devices are controlled with a driver that is connected using subminiature version A (SMA) connectors to the outside of the cryostat, and Bayonet Neill-Concelman (BNC) connectors to the oscilloscope. The oscilloscope retrieves the voltage pulses as a function of time and can perform time jitter measurements to determine the uncertainty in the arrival of the photons due to the detector characteristics, electrical circuitry and optical setup. A BNC cable is connected from the pulsed laser to the oscilloscope for these measurements to give a reference trigger signal.

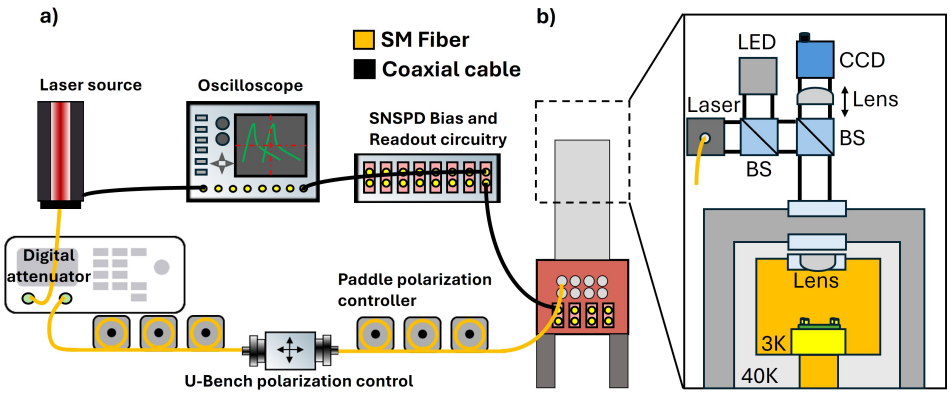

Figure 3.6: a) Overview of the cryogenic setup for SNSPD measurements. The laser source can be a tunable laser for telecom (to characterize ring resonators) or a pulsed laser (to determine the time jitter of the detectors). For time jitter, the pulsed laser is connected to the oscilloscope via coaxial cables for synchronization with the readout signal of the detectors given by the driver. The light is attenuated by a digital attenuator, aligned with paddle polarization controller to a free-space polarizer in a U-bench and again aligned to the maximum coupling of the grating couplers with another paddle polarization controller. b) Open window imaging and laser input. The output from the U-bench goes to a laser collimator in the cage square bracket system and is coupled into the devices using grating couplers.

REFERENCES

[1] P. Xing, D. Ma, K. J. Ooi, J. W. Choi, A. M. Agarwal, and D. Tan, *Cmos-compatible pecvd silicon carbide platform for linear and nonlinear optics,* ACS Photonics **6**, 1162 (2019).

[2] F. Karouta, K. Vora, J. Tian, and C. Jagadish, *Structural, compositional and optical properties of pecvd silicon nitride layers,* Journal of Physics D: Applied Physics **45**, 445301 (2012).

[3] L. Wang, W. Xie, D. Van Thourhout, Y. Zhang, H. Yu, and S. Wang, *Nonlinear silicon nitride waveguides based on a pecvd deposition platform,* Optics Express **26**, 9645 (2018).

[4] A. S. Tong, D. K. Ng, R. Kanhirakkottil, J. S. Goh, J. Jin, A. W. Fong, S. H. Lee, H. Cai, and L. Y. Lee, *Material characterization of silicon dioxide cladding for photonic devices,* in *Oxide-based Materials and Devices XV,* Vol. 12887 (SPIE, 2024) pp. 74–78.

[5] W. Jin, D. D. John, J. F. Bauters, T. Bosch, B. J. Thibeault, and J. E. Bowers, *Deuterated silicon dioxide for heterogeneous integration of ultra-low-loss waveguides,* Optics Letters **45**, 3340 (2020).

[6] L. Mehrvar, B. Le Drogoff, M. Menard, and M. Chaker, *Teos-pecvd films for high-quality SiO_2 cladding layers in Si_3N_4-photonics with low mechanical stress and optical loss,* in *2024 Photonics North (PN)* (IEEE, 2024) pp. 1–2.

[7] S. Yang, Z. Ding, X. Li, X. Luo, S. Zhai, X. Zheng, B. Wang, H. Li, Z. Deng, Q. Wang, *et al.*, *Visible to near-infrared light integrated photonic components on pecvd and lpcvd sin platform,* IEEE Photonics Journal (2024).

[8] X. Ji, Y. Okawachi, A. Gil-Molina, M. Corato-Zanarella, S. Roberts, A. L. Gaeta, and M. Lipson, *Ultra-low-loss silicon nitride photonics based on deposited films compatible with foundries,* Laser & Photonics Reviews **17**, 2200544 (2023).

[9] P. K. Revuri, D. Tripathi, M. Martyniuk, K. Silva, G. Putrino, A. Keating, and L. Faraone, *Silicon and silicon dioxide thin films deposited by icpcvd at low temperature and high rate for mems applications,* in *2018 Conference on Optoelectronic and Microelectronic Materials and Devices (COMMAD)* (IEEE, 2018) pp. 24–26.

[10] J. Lee, K. Mackenzie, D. Johnson, J. Sasserath, S. Pearton, and F. Ren, *Low temperature silicon nitride and silicon dioxide film processing by inductively coupled plasma chemical vapor deposition,* Journal of The Electrochemical Society **147**, 1481 (2000).

[11] I. Parkhomenko, L. Vlasukova, F. Komarov, N. Kovalchuk, S. Demidovich, A. Zhussupbekova, K. Zhussupbekov, I. V. Shvets, O. Milchanin, D. Zhigulin, *et al.*, *Effect of rapid thermal annealing on si-based dielectric films grown by icp-cvd,* ACS omega **8**, 30768 (2023).

[12] K. Yang, O. De Sagazan, L. Pichon, A.-C. Salaün, and N. Coulon, *Inductively coupled plasma chemical vapor deposition for silicon-based technology compatible with low-temperature (≤ 220° c) flexible substrates,* Physica Status Solidi (a) **217**, 1900556 (2020).

[13] D. Bose, M. W. Harrington, A. Isichenko, K. Liu, J. Wang, N. Chauhan, Z. L. Newman, and D. J. Blumenthal, *Anneal-free ultra-low loss silicon nitride integrated photonics,* Light: Science & Applications **13**, 156 (2024).

[14] B. Lopez-Rodriguez, R. Van Der Kolk, S. Aggarwal, N. Sharma, Z. Li, D. Van Der Plaats, T. Scholte, J. Chang, S. Gro¨blacher, S. F. Pereira, *et al.*, *High-quality amorphous silicon carbide for hybrid photonic integration deposited at a low temperature,* ACS Photonics **10**, 3748 (2023).

[15] B. Lopez-Rodriguez, N. Sharma, Z. Li, R. van der Kolk, J. van der Boom, T. Scholte, J. Chang, S. Gro¨eblacher, and I. Esmaeil Zadeh, *Magic silicon dioxide for widely tunable photonic integrated circuits,* ACS Photonics (2025).

[16] J. Zichi, J. Chang, S. Steinhauer, K. Von Fieandt, J. W. Los, G. Visser, N. Kalhor, T. Lettner, A. W. Elshaari, I. E. Zadeh, *et al.*, *Optimizing the stoichiometry of ultrathin nbtin films for high-performance superconducting nanowire single-photon detectors,* Optics Express **27**, 26579 (2019).

4

HIGH-QUALITY AMORPHOUS SILICON CARBIDE FOR HYBRID PHOTONIC INTEGRATION DEPOSITED AT A LOW TEMPERATURE

The results shown in this chapter have been published in ACS Photonics **2023**, 10(10), 3748-3754

Integrated photonic platforms have proliferated in recent years, each demonstrating its own unique strengths and shortcomings. Given the processing incompatibilities of different platforms, a formidable challenge in the field of integrated photonics still remains for combining the strength of different optical materials in one hybrid integrated platform. Silicon carbide is a material of great interest because of its high refractive index, strong second and third-order non-linearities and broad transparency window in the visible and near infrared. However, integrating SiC has been difficult, and current approaches rely on transfer bonding techniques, that are time consuming, expensive and lacking precision in layer thickness. Here, we demonstrate high index Amorphous Silicon Carbide (a-SiC) films deposited at 150°C and verify the high performance of the platform by fabricating standard photonic waveguides and ring resonators. The intrinsic quality factors of single-mode ring resonators were in the range of $Q_{int} = (4.7-5.7) \times 10^5$ corresponding to optical losses between 0.78-1.06 dB/cm. We then demonstrate the potential of this platform for future heterogeneous integration with ultralow loss thin SiN and $LiNbO_3$ platforms.

4.1. INTRODUCTION

Integrated photonics is a rapidly-growing field that is revolutionizing the way we use light for computing, communication, and sensing. By developing new platforms and technologies, researchers are continuously enhancing the performance and capabilities of the building blocks of future photonic technologies. Silicon-On-Insulator [1], Silicon Nitride [2] and Aluminum Nitride [3] have shown outstanding performance, for example, in sub-picometer wavelength filters, low loss and high visibility Mach-Zehnder interferometers and accurate variable beam splitters. Due to the persisting demand to unlock new properties and allow for higher degrees of freedom in photonic devices, materials that offer tunability and strong non-linear behavior have gained attention in recent years.

Silicon Carbide (SiC) is emerging as a promising material for integrated quantum photonics due to its unique characteristics such as a high refractive index, strong second- and third-order optical non-linearities [4, 5] (arising from a wide band gap and suppressed two-photon absorption at telecom wavelengths) and a broad transparency window from visible to the mid-infrared range [6]. For quantum computing experiments, different crystalline forms of silicon carbide are being incorporated in a broad range of photonic schemes to individually address single-photon sources[7] and spin-qubits [8]. 4H-SOI SiC ring resonators have been shown to exhibit quality factors between 1.1×10^6 (making them a valuable demonstrator for optical parametric oscillation) [9] and 5.6×10^6 (used in experiments to study soliton micro-combs) [10]. On the other hand, the highest reported quality factor in a silicon carbide platform was achieved using its crystalline form 4H-SiCOI and reached values up to 6.75×10^6 in micro-disk resonators [11]. However, one challenge in using SiC in quantum photonics is the need for transfer-bonding methods when depositing the crystalline material onto other substrates [11] involving expensive and time-consuming processes together with issues regarding precise thickness control, complicating hybrid integration. Furthermore, provided that this last requirement is fulfilled, processing temperatures and chemical interactions between the different materials give rise to compatibility issues.

For hybrid integration with other platforms, an inert material such as amorphous silicon carbide has great potential. One of the most promising properties of a-SiC is its strong third-order nonlinearity, which is ten times higher than SiN [12] and crystalline SiC [13], useful in, for example, four-wave mixing processes. This has been attributed to the presence of intermediate states (traps or defects) within the band gap which are more prominent in amorphous films and that can lead to enhanced two-photon and three-photon absorption [14]. In another work, the non-linear refractive index of a-SiC was improved by increasing the C-C bonds in C-rich SiCx after annealing [15]. From the standard Chemical Vapor Deposition (CVD) techniques, Plasma-Enhanced CVD (PECVD) has shown excellence in terms of optical performances in ring resonators with intrinsic quality factors reaching up to 1.6×10^5 at around 1550 nm [16]. Furthermore, it was compatible with the well-established CMOS fabrication processes. Recently, four-wave mixing has also been demonstrated using this platform with micro-ring resonators having loaded quality factors of 0.7×10^5 at around 1550 nm [17]. Therefore, it remains a challenge to decrease the losses in this platform and compete with well-established technologies.

In this work, we fabricate and characterize ring resonators on amorphous silicon carbide films deposited via Inductively Coupled Plasma-Enhanced CVD (Oxford ICPCVD PlasmaPro100). All optical devices show intrinsic quality factors above 4.66×10^5, with the highest being 5.7×10^5, overall, more than three times higher than previous achievements with this material and waveguide propagation loss ranging between 0.78-1.07 dB/cm. These values are comparable to well established platforms that can be deposited at low temperatures such as PECVD SiN at 350°C (0.42 dB/cm [18]). Additionally, using our ICPCVD optimized recipe, the a-SiC films can be deposited at 150°C, which to our knowledge is the lowest temperature among other techniques and can be implemented with a variety of optical materials with a simple lift-off process. Most importantly, we demonstrate a fabrication route for heterogeneous integration of a-SiC films with SiN and LNOI supported by optical simulations. Table 1 shows a comparison of the different reported SiC platforms. A more comprehensive table can be found in the supplementary information (table S2 of appendix A).

Material	Width/Thickness (nm)	Q_{int}(x10^5)/Losses(dB/cm)	T (°C)	Reference
3C-SiCOI	1700/500	1.42 / 2.9	-	19
4H-SiCOI	3000/530	11 / 0.38	-	9
4H-SiCOI	1850/500-600	56 / Not reported	-	10
PECVD a-SiC	800/350	1.6 / 3	300	16
ICPCVD a-SiC	**750/280**	**4.7-5.7 / 0.78-1.07**	**150**	**This work**

Table 4.1: Comparison of different waveguide-based optical devices in SiC.

4.2. AMORPHOUS SILICON CARBIDE

4.2.1. DEPOSITION OF A-SiC FILMS

Amorphous silicon carbide has gained interest as a photonic platform due to its high refractive index, large and tunable band gap, chemically inert nature, and potential

compatibility with CMOS processes. The deposition of amorphous Silicon Carbide thin films can be achieved with Low-Pressure CVD (LPCVD) [20], PECVD [21] and ICPCVD [22], where the latest two have been shown in previous studies with good reproducibility not only for Silicon Carbide but also with other materials for photonic devices, such as Silicon Nitride. [16, 23, 24].

The main difference between PECVD and ICPCVD is in the plasma coupling mechanisms, i.e. inductive coupling in the case of ICPCVD while PECVD is capacitively coupled. In the case of PECVD, the bias between the parallel plates is coupled to the forward plasma power, which in turn means that a higher plasma density can cause more ion damage to the substrate compared to ICPCVD. Therefore, in PECVD, the plasma densities have to be kept lower than in ICPCVD. The latter means that in ICPCVD depositions, lower deposition temperatures and higher densities can be achieved [25–27].

In optical devices, the performance is mainly affected by the presence of Si-H and N-H bonds, which is the major loss mechanism for SiN-based resonators (assuming that roughness effects have been eliminated through conventional techniques) [28, 29]. In the case of a-SiC:H thin films, Si-H bonds are also present in addition to C-H bonds. As shown in some studies, hydrogenation decreases with density, involving the increase of the deposition temperature [30].

Fig.4.1a shows the experimentally measured (using an ellipsometer) refractive index (n) and the loss coefficient (k) of an a-SiC film deposited at 150°C. The refractive index of the a-SiC is 2.55 at 1550 nm, which is higher than the refractive index of SiN, leading to more compact and improved device integration since a higher refractive index translates into a high field confinement. Most importantly, depending on the Si and C content of the films, the refractive index and the overall properties of the material can be tuned to match the specific requirements (see Fig. S1 in appendix A).

The inset of fig.4.1a shows typical deposition results on a small 15x15 mm thermally oxidized silicon sample. The color variation close to the edges reveals thickness non-uniformity in the PECVD sample (left) due to thin film interference [31] while, in contrast, ICPCVD (right) shows excellent uniformity. The non-uniformity in PECVD is primarily attributed to edge effects and skin effects [32], which are more prominent in smaller samples due to their increased surface-to-volume ratio. Moreover, the larger plasma sheet leads to more ions accelerating towards the sample from the edge regions and with higher energies [25]. Such uniformity is especially important for wafer-scale processing, where the cost can be reduced through the optimization of the deposition process.

Atomic Force Microscopy (AFM) images in fig.4.1b reveal that the grain size of the PECVD film (left) is significantly larger than that of the ICPCVD film (right). This observation is consistent with previous studies that have suggested that higher plasma densities in PECVD lead to larger grain sizes [33]. Specifically, the root-mean-square (r_q) values for the ICPCVD and PECVD films were found to be 1.02 nm and 1.27 nm, respectively. The difference in surface roughness and grain size between the two films can significantly affect their optical properties.

An important advantage of a-SiC is the possibility to incorporate nitrogen as has been previously demonstrated [34] that could lead to conductive films and optical elements where the devices can be tuned directly with electrical contacts, and therefore allowing

configurations for e.g. optical switches [35] or adding tunability to multimode interferometers (MMIs) [36].

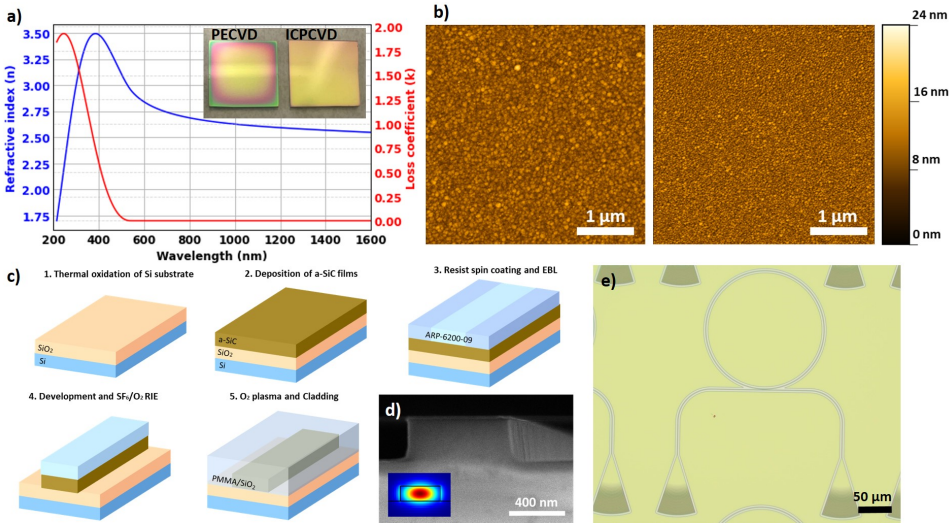

Figure 4.1: a) Refractive index (n) and loss coefficient (k) for ICPCVD films deposited at 150°C. Inset: comparison between film uniformities for the cases of deposition using PECVD and ICPCVD techniques, b) AFM scans of films deposited at 250°C using PECVD (left) and ICPCVD (right), c) fabrication flow for the optical devices and d) SEM image of the waveguide cross-section. Inset: FDTD simulation of the confined mode and e) optical microscope image of a ring resonator device with grating couplers.

4.2.2. EXPERIMENTAL METHODS

A complete process flow of the fabrication of the final photonic devices is shown in fig.4.1c. a-SiC films were deposited with ICPCVD on 2.5 μm thermally grown silicon dioxide. The film thickness for the deposited a-SiC was chosen according to FDTD simulations to ensure single-mode operation in the waveguides and ring resonator (inset of fig.4.1d) and the final film thickness and refractive index was determined using an ellipsometer.

To define the structures, ARP-6200-09 electron beam positive resist was spin-coated and the patterns were formed using electron beam lithography. After exposure, the samples were developed and afterward etched using reactive ion etching (RIE Sentech Etchlab 200) with a mixture of SF_6 and O_2. A final layer of PMMA (1 μm) or SiO_2 was used to enhance the confinement in the waveguides acting as a top cladding. To characterize the devices, we have used both edge and grating couplers. Fig.4.1d shows an electron microscope image of a cross-section of a device and fig.4.1e an optical microscope image of a device with grating couplers. For thermo-optic measurements, a thick (3 μm) layer of SiO_2 was deposited on top of the devices.

For the side coupling configuration, we used a C-band tunable laser (Photonetics TUNICS-PRI 3642 HE 15). The polarization incident in the waveguide was selected using a free space polarizer and polarization-maintaining fibers (OZ Optics V-groove assem-

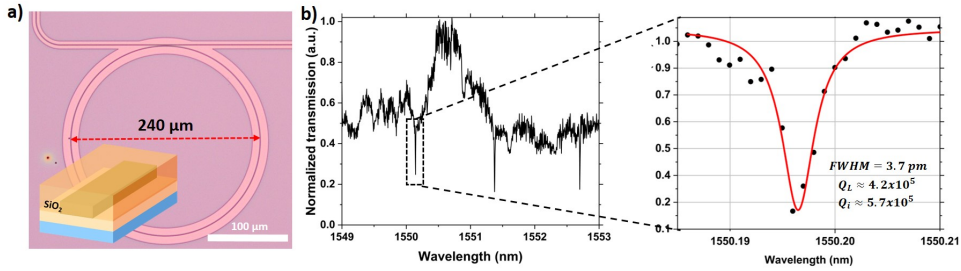

Figure 4.2: a) Optical microscope image of a ring resonator made on films deposited at 150°C with ICPCVD covered with silicon dioxide cladding as represented in the inset, b) spectrum between 1549 nm and 1553 nm of the device and scan with 1 pm resolution of the selected resonant dip at 1550.196 nm.

4

bly). To obtain the transmission spectrum of the optical ring resonators, the wavelength of the laser was swept in the desired range with 1 pm resolution. The output power was recorded with a photodetector (Newport 843-R).

4.3. RESULTS AND DISCUSSION

4.3.1. DEVICE CHARACTERIZATION

Many ring resonators fabricated on PECVD and ICPCVD films with various parameters such as waveguide width, gap, ring radius, and deposition temperature were thoroughly studied and compared, and the overall results can be found in appendix A together with the equations to determine the quality factor and waveguide propagation losses.

The highest quality factors were obtained for a deposition with ICPVCD at a temperature of 150°C for a ring resonator with ring radius of 120 μm as shown in fig.4.2a and the data is shown in fig.4.2b, from which a free spectral range of 1.3 nm is determined. A loaded quality factor (Q_L) of 4.2x10^5 was measured and the intrinsic quality factor (Q_{int}) of the device is estimated to be 5.7x10^5 which is more than three times higher than previously reported results [16], corresponding to waveguide propagation losses of 0.89 dB/cm. The lowest propagation loss was 0.78 dB/cm for the ring resonator shown in Fig.S6 of appendix A.

4.3.2. THERMO-OPTIC COEFFICIENT OF ICPCVD A-SIC

The thermo-optic coefficient plays a major role in the choice of photonic platforms, where many applications require low-power thermal tuning to reduce the thermal cross-talk between devices. In this latter case, platforms based on SiN and SiO_2 have shown poor performance [37], making thermal tuning a challenging task. In this work, we measure the thermo-optic coefficient of a-SiC deposited via ICPCVD by studying the shift in the resonance wavelength of optical ring resonators upon a change in temperature in a range between 23°C and 47°C and the setup is shown in fig.S9 of appendix A. This is done by using a heater in the sample holder that is thermally connected to the PCB through a copper block. In the same location as the heater, there is a thermistor used to monitor the temperature. The sample is fixed into the PCB using thermally conductive

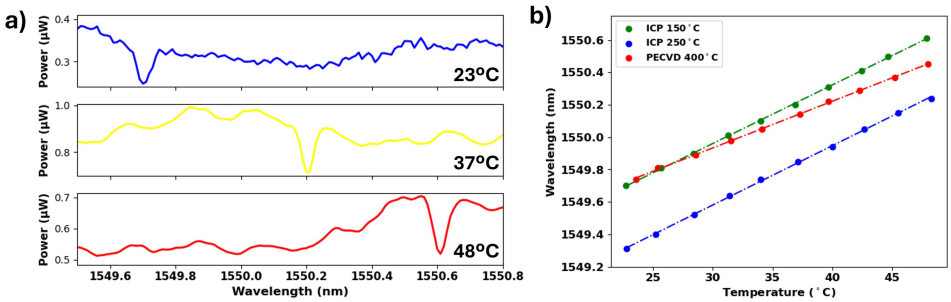

Figure 4.3: a) Transmission spectra for a-SiC deposited at 150°C as the temperature of the devices is raised at 23°C (blue), 37°C (yellow) and 48°C (red) and b) wavelength shift of a resonance dip as a function of temperature for devices made on ICPCVD a-SiC films deposited at 150°C and 250°C and PECVD a-SiC deposited at 400°C taken with steps of 2°C.

silver paste. The heater and thermistor are connected to a controller to change the temperature and keep it constant through a feedback loop. Fig.4.3a shows a representative transmission spectrum at different temperatures taken from the device from which we achieved the highest quality factors. Fig.4.3b shows the wavelength of a specific resonance dip for temperature steps of 2°C for devices fabricated on ICP and PECVD films. The change in effective refractive index (n_{eff}) as a function of the material temperature can be derived from the following relation [38]:

$$\frac{d\lambda}{dT} = \left(a n_{\text{eff}} + \frac{dn_{\text{eff}}}{dT}\right)\frac{\lambda}{n_g} \tag{4.1}$$

with $a = 2.6\text{x}10^{-6}/°\text{C}$ being the expansion coefficient of the thermal Silicon Dioxide upon a change in temperature, n_{eff} the effective index of the a-SiC waveguide with 750 nm in width and varying thickness (measured by ellipsometry and confirmed with SEM) that have been estimated using 3D FDTD simulations in Lumerical, and n_g is the group index at 1550 nm that is obtained from the transmission spectra (see fig.S7 of appendix A). The equation that relates the thermo-optic coefficient of the materials involved with the change in the effective refractive index as a function of temperature was obtained in previous studies using the overlap integral approximation [39, 40]:

$$\frac{dn_{\text{eff}}}{dT} = \Gamma_{\text{SiO}_2}\frac{dn_{\text{SiO}_2}}{dT} + \Gamma_{\text{a-SiC}}\frac{dn_{\text{a-SiC}}}{dT} \tag{4.2}$$

where Γ denotes the overlap integral coefficients for the Silicon Dioxide cladding and the Silicon Carbide waveguide and is determined using 3D Mode simulations in Lumerical with the specific dimensions of the individual devices. The thermo-optic coefficient of PECVD SiO_2 is already known to be $0.96\text{x}10^{-6}/°\text{C}$ as determined in the literature [37]. For the devices made on a-SiC deposited at 150°C, a thermo-optic coefficient of $7.3\text{x}10^{-5}/°C$ is obtained, which is three times higher than PECVD SiN [37]. As a reference, thermo-optic measurements of a-SiC deposited via PECVD at 400°C are also shown, with a thermo-optic coefficient of $5.1\text{x}10^{-5}/°C$, overall in agreement with previous works [41].

4.4. HYBRID INTEGRATION AND FUTURE OUTLOOK

In quantum photonic circuits, routing photons with low losses is a vital requirement and to this end, over the last decade, material platforms such as LPCVD Silicon Nitride have been extensively optimized to reduce the losses. Recent works using thin film SiN waveguides have enabled high-yield and wafer-scale fabrication with losses as low as 1 dB/m [42, 43] which is a fundamental requirement for two-photon interference on chip [44, 45]. As a future outlook, we highlight in fig.4.4a the use of 280 nm thick a-SiC in combination with low-loss waveguides based on Silicon Nitride thin-films (40 nm) and Lithium Niobate, two promising platforms for integrated quantum photonics. In this scheme, delay lines and photonic routing can be done with low-loss on SiN to later exploit the non-linearity of a-SiC in wavelength conversion experiments and generation of entangled photon pairs. It can also be used in combination with crystalline Silicon Carbide or Silicon to deterministically address single photon sources and route the single photons. The input light can be delivered to the photonic structures using grating couplers, edge couplers or directly produced on-chip by embedded nanowire quantum dots based on III-V materials[46]. Photonic mirrors can be used to improve the collection efficiency of the quantum dots and electrical gates allow the control of the fine structure splitting [47]. A tapered waveguide is designed to avoid coupling losses when the light is injected from 40 nm SiN waveguides to the 280 nm a-SiC (n=2 and n=2.589 respectively at 1550 nm). These structures are later covered with a 3 μm thick silicon dioxide cladding that is also tapered to improve the confinement. From FDTD simulations, a taper length of 150 μm achieves a coupling efficiency of 92.6% at a wavelength of 1550 nm with very high confinement in the a-SiC waveguide confirmed by the low bending losses of the mode (see fig.S12 in appendix A). Manipulation of light can be performed via variable beamsplitters and Mach-Zehnder interferometers and routed towards superconducting single-photon detectors forming the basic building blocks to perform quantum photonic operations.

Owing to the low temperature at which these films are deposited, we demonstrate a feasible approach to integrate the a-SiC films with current platforms based in a lift-off process with PMMA in fig.4.4b, where the specific details about the procedure can be found in appendix A.

Lithium Niobate ($LiNbO_3$) provides efficient electro-optic modulation, high second-order non-linearity, broad transparency window from the visible to the mid-infrared range [48] and ultralow losses at telecommunication wavelengths as demonstrated in an LNOI platform [49]. For this reason, to include our a-SiC devices in this platform and combine the properties that they both offer, in appendix A (fig.S13a) we demonstrate a fabrication route for heat-free tuning of photonic devices together with FDTD simulations of the mode profile (fig.S13b).

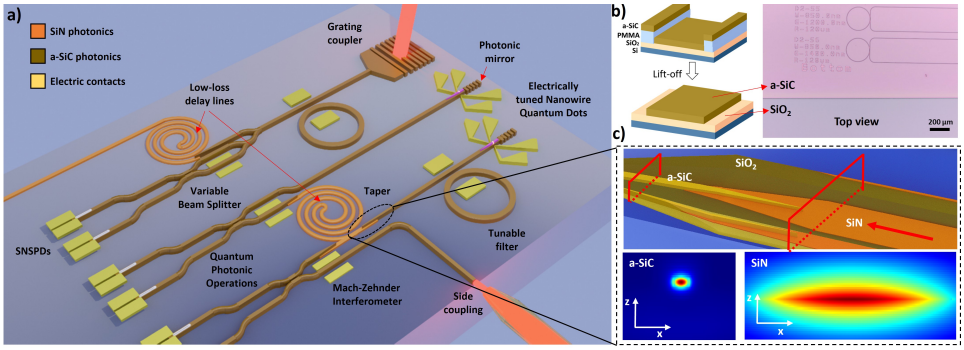

Figure 4.4: a) Amorphous Silicon Carbide Photonic devices made on a Silicon Nitride platform. Light coupling can be performed via side coupling, using grating couplers or waveguide-embedded nanowire quantum dots that have a mirror for enhanced optical collection and can be electrically tuned. The representation includes tunable single-photon filtering with ring resonators, low-loss delay lines made on thin-film a-SiC (or SiN), Mach-Zehnder interferometers, Variable Beamsplitters and Superconducting Nanowire Single Photon Detectors (SNSPDs). b) lift-off process and optical microscope top-view image of the fabricated devices, c) FDTD simulations of the mode profile in tapered a-SiC/SiN waveguides embedded in a tapered SiO_2 cladding for a high coupling efficiency.

REFERENCES

[1] N. Margalit, C. Xiang, S. M. Bowers, A. Bjorlin, R. Blum, and J. E. Bowers, *Perspective on the future of silicon photonics and electronics,* Applied Physics Letters **118**, 220501 (2021).

[2] C. Xiang, W. Jin, and J. E. Bowers, *Silicon nitride passive and active photonic integrated circuits: trends and prospects,* Photon. Res. **10**, A82 (2022).

[3] N. Li, C. P. Ho, S. Zhu, Y. H. Fu, Y. Zhu, and L. Y. T. Lee, *Aluminium nitride integrated photonics: a review,* Nanophotonics **10**, 2347 (2021).

[4] H. Sato, M. Abe, I. Shoji, J. Suda, and T. Kondo, *Accurate measurements of second-order nonlinear optical coefficients of 6h and 4h silicon carbide,* J. Opt. Soc. Am. B **26**, 1892 (2009).

[5] Y. Zheng, M. Pu, A. Yi, X. Ou, and H. Ou, *4h-sic microring resonators for nonlinear integrated photonics,* Opt. Lett. **44**, 5784 (2019).

[6] S. Wang, M. Zhan, G. Wang, H. Xuan, W. Zhang, C. Liu, C. Xu, Y. Liu, Z. Wei, and X. Chen, *4h-sic: a new nonlinear material for midinfrared lasers,* Laser & Photonics Reviews **7**, 831 (2013).

[7] D. M. Lukin, M. A. Guidry, and J. Vuč ković, *Integrated quantum photonics with silicon carbide: Challenges and prospects,* PRX Quantum **1**, 020 (2020).

[8] Q. Li, J.-F. Wang, F.-F. Yan, J.-Y. Zhou, H.-F. Wang, H. Liu, L.-P. Guo, X. Zhou, A. Gali, Z.-H. Liu, Z.-Q. Wang, K. Sun, G.-P. Guo, J.-S. Tang, H. Li, L.-X. You, J.-S. Xu, C.-F. Li, and G.-C. Guo, *Room-temperature coherent manipulation of single-spin qubits in silicon carbide with a high readout contrast,* National Science Review **9**, 2095 (2021).

[9] M. A. Guidry, K. Y. Yang, D. M. Lukin, A. Markosyan, J. Yang, M. M. Fejer, and J. Vučković, *Optical parametric oscillation in silicon carbide nanophotonics,* Optica **7**, 1139 (2020).

[10] M. A. Guidry, D. M. Lukin, K. Y. Yang, R. Trivedi, and J. Vučković, *Quantum optics of soliton microcombs,* Nature Photonics **16**, 52 (2021).

[11] C. Wang, Z. Fang, A. Yi, B. Yang, Z. Wang, L. Zhou, C. Shen, Y. Zhu, Y. Zhou, R. Bao, Z. Li, Y. Chen, K. Huang, J. Zhang, Y. Cheng, and X. Ou, *High-q microresonators on 4h-silicon-carbide-on-insulator platform for nonlinear photonics,* Light: Science & Applications **10**, 139 (2021).

[12] Z. Ye, A. Fülöp, Óskar Bjarki Helgason, P. A. Andrekson, and V. Torres-Company, *Low-loss high-q silicon-rich silicon nitride microresonators for kerr nonlinear optics,* Opt. Lett. **44**, 3326 (2019).

[13] X. Lu, J. Y. Lee, S. Rogers, and Q. Lin, *Optical kerr nonlinearity in a high-q silicon carbide microresonator,* Opt. Express **22**, 30826 (2014).

[14] X. Yu, B. Ding, H. Lu, Y. Huo, Q. Peng, X. Xiu, C. Zhang, C. Yang, S. Jiang, B. Man, and T. Ning, *Third-order optical nonlinearity in nonstoichiometric amorphous silicon carbide films,* Journal of Alloys and Compounds **794**, 518 (2019).

[15] C.-H. Hsieh, C.-H. Cheng, H.-Y. Wang, C.-T. Tsai, Y.-C. Chi, and G.-R. Lin, IEEE J. Sel. Top. Quantum Electron **24**, 8301210 (2018).

[16] P. Xing, D. Ma, K. J. A. Ooi, J. W. Choi, A. M. Agarwal, and D. Tan, *Cmos-compatible pecvd silicon carbide platform for linear and nonlinear optics,* ACS Photonics **6**, 1162 (2019).

[17] P. Xing, D. Ma, L. C. Kimerling, A. M. Agarwal, and D. T. H. Tan, *High efficiency four wave mixing and optical bistability in amorphous silicon carbide ring resonators,* APL Photonics **5**, 076110 (2020).

[18] X. Ji, Y. Okawachi, A. Gil-Molina, M. Corato-Zanarella, S. Roberts, A. L. Gaeta, and M. Lipson, *Ultra-low-loss silicon nitride photonics based on deposited films compatible with foundries,* Laser & Photonics Reviews **17**, 2200544 (2023).

[19] T. Fan, H. Moradinejad, X. Wu, A. A. Eftekhar, and A. Adibi, *High-q integrated photonic microresonators on 3c-sic-on-insulator (sicoi) platform,* Opt. Express **26**, 25814 (2018).

[20] B. Morana, G. Pandraud, J. Creemer, and P. Sarro, *Characterization of lpcvd amorphous silicon carbide (a-sic) as material for electron transparent windows,* Materials Chemistry and Physics **139**, 654 (2013).

[21] E. Chen, G. Du, Y. Zhang, X. Qin, H. Lai, and W. Shi, *Rf-pecvd deposition and optical properties of hydrogenated amorphous silicon carbide thin films,* Ceramics International **40**, 9791 (2014).

[22] T. Frischmuth, M. Schneider, D. Maurer, T. Grille, and U. Schmid, *Inductively-coupled plasma-enhanced chemical vapour deposition of hydrogenated amorphous silicon carbide thin films for mems,* Sensors and Actuators A: Physical **247**, 647 (2016).

[23] Z. Wu, Z. Shao, Z. Xu, Y. Zhang, L. Liu, C. Yang, Y. Chen, and S. Yu, *High quality factor deuterated silicon nitride (sin:d) microring resonators,* in *CLEO Pacific Rim Conference 2018* (Optica Publishing Group, 2018) p. W4D.5.

[24] X. Ji, S. P. Roberts, and M. Lipson, *High quality factor pecvd si3n4 ring resonators compatible with cmos process,* in *Conference on Lasers and Electro-Optics* (Optica Publishing Group, 2019) p. SM2O.6.

[25] M. A. Lieberman and A. J. Lichtenberg, *Direct current (dc) sheaths,* in *Principles of Plasma Discharges and Materials Processing* (John Wiley & Sons, Ltd, 2005) Chap. 6, pp. 165–206.

[26] M. A. Lieberman and A. J. Lichtenberg, *Capacitive discharges,* in *Principles of Plasma Discharges and Materials Processing* (John Wiley & Sons, Ltd, 2005) Chap. 11, pp. 387–460.

[27] M. A. Lieberman and A. J. Lichtenberg, *Inductive discharges,* in *Principles of Plasma Discharges and Materials Processing* (John Wiley & Sons, Ltd, 2005) Chap. 12, pp. 461–489.

[28] M. H. P. Pfeiffer, J. Liu, A. S. Raja, T. Morais, B. Ghadiani, and T. J. Kippenberg, *Ultra-smooth silicon nitride waveguides based on the damascene reflow process: fabrication and loss origins,* Optica **5**, 884 (2018).

[29] W. Jin, Q.-F. Yang, L. Chang, B. Shen, H. Wang, M. A. Leal, L. Wu, M. Gao, A. Feshali, M. Paniccia, K. J. Vahala, and J. E. Bowers, *Hertz-linewidth semiconductor lasers using CMOS-ready ultra-high-q microresonators,* Nature Photonics **15**, 346 (2021).

[30] F. Karouta, K. Vora, J. Tian, and C. Jagadish, *Structural, compositional and optical properties of pecvd silicon nitride layers,* Journal of Physics D: Applied Physics **45**, 445301 (2012).

[31] L. Wang, S. Dimitrijev, G. Walker, J. Han, A. Iacopi, P. Tanner, L. Hold, Y. Zhao, and F. Iacopi, *Color chart for thin sic films grown on si substrates,* Materials Science Forum **740-742**, 279 (2013).

[32] P. Chabert, *Electromagnetic effects in high-frequency capacitive discharges used for plasma processing,* Journal of Physics D: Applied Physics **40**, R63 (2007).

[33] U. Coscia, G. Ambrosone, S. Lettieri, P. Maddalena, V. Rigato, S. Restello, E. Bobeico, and M. Tucci, *Preparation of microcrystalline silicon–carbon films,* Solar Energy Materials and Solar Cells **87**, 433 (2005), international Conference on Physics, Chemistry and Engineering.

[34] J. Šafránková, J. Huran, I. Hotový, A. Kobzev, and S. Korenev, *Characterization of nitrogen-doped amorphous silicon carbide thin films, paper presented at the 10th international school of vacuum electron and ion technologies, 22–27 september 1997, varna, bulgaria,* Vacuum **51**, 165 (1998).

[35] B. Li, *2 - electro-optical switches,* in *Optical Switches*, Woodhead Publishing Series in Electronic and Optical Materials, edited by B. Li and S. J. Chua (Woodhead Publishing, 2010) pp. 5–e8.

[36] D. Chack and S. Hassan, *Design and experimental analysis of multimode interference-based optical splitter for on-chip optical interconnects,* Optical Engineering **59**, 105102 (2020).

[37] A. W. Elshaari, I. E. Zadeh, K. D. Jöns, and V. Zwiller, *Thermo-optic characterization of silicon nitride resonators for cryogenic photonic circuits,* IEEE Photonics Journal **8**, 1 (2016).

[38] F. Qiu, A. M. Spring, and S. Yokoyama, *Athermal and high-q hybrid tio2–si3n4 ring resonator via an etching-free fabrication technique,* ACS Photonics **2**, 405 (2015).

[39] J. T. Robinson, L. Chen, and M. Lipson, *On-chip gas detection in silicon optical microcavities,* Opt. Express **16**, 4296 (2008).

[40] J. T. Robinson, K. Preston, O. Painter, and M. Lipson, *First-principle derivation of gain in high-index-contrast waveguides,* Opt. Express **16**, 16659 (2008).

[41] L.-Y. S. Chang, S. Pappert, and P. K. L. Yu, *High thermo-optic tunability in pecvd silicon-rich amorphous silicon carbide,* Opt. Lett. **48**, 1188 (2023).

[42] D. T. Spencer, J. F. Bauters, M. J. R. Heck, and J. E. Bowers, *Integrated waveguide coupled si3n4 resonators in the ultrahigh-q regime,* Optica **1**, 153 (2014).

[43] S. Gundavarapu, G. M. Brodnik, M. Puckett, T. Huffman, D. Bose, R. Behunin, J. Wu, T. Qiu, C. Pinho, N. Chauhan, J. Nohava, P. T. Rakich, K. D. Nelson, M. Salit, and D. J. Blumenthal, *Sub-hertz fundamental linewidth photonic integrated brillouin laser,* Nature Photonics **13**, 60 (2018).

[44] L. Dusanowski, D. Köck, C. Schneider, and S. Höfling, *On-chip hong–ou–mandel interference from separate quantum dot emitters in an integrated circuit,* ACS Photonics **10**, 2941 (2023).

[45] A. Chanana, H. Larocque, R. Moreira, J. Carolan, B. Guha, E. G. Melo, V. Anant, J. Song, D. Englund, D. J. Blumenthal, K. Srinivasan, and M. Davanco, *Ultra-low loss quantum photonic circuits integrated with single quantum emitters,* Nature Communications **13**, 7693 (2022).

[46] I. E. Zadeh, A. W. Elshaari, K. D. Jöns, A. Fognini, D. Dalacu, P. J. Poole, M. E. Reimer, and V. Zwiller, *Deterministic integration of single photon sources in silicon based photonic circuits,* Nano Letters **16**, 2289 (2016).

[47] M. Zeeshan, N. Sherlekar, A. Ahmadi, R. L. Williams, and M. E. Reimer, *Proposed scheme to generate bright entangled photon pairs by application of a quadrupole field to a single quantum dot,* Phys. Rev. Lett. **122**, 227401 (2019).

[48] Y. Qi and Y. Li, *Integrated lithium niobate photonics,* Nanophotonics **9**, 1287 (2020).

[49] B. Desiatov, A. Shams-Ansari, M. Zhang, C. Wang, and M. Lončar, *Ultra-low-loss integrated visible photonics using thin-film lithium niobate,* Optica **6**, 380 (2019).

5

MAGIC SILICON DIOXIDE FOR WIDELY TUNABLE INTEGRATED PHOTONICS

Parts of this this chapter have been published in ACS Photonics **2025**, 12(3), 1321-1328

Integrated photonic circuits have transformed data communication, biosensing, and light detection and ranging, and hold wide-ranging potential for optical computing, optical imaging and signal processing. These applications often require tunable and reconfigurable photonic components, most commonly accomplished through the thermo-optic effect. However, the resulting tuning window is limited for standard optical materials such as silicon dioxide and silicon nitride. Most importantly, bidirectional thermal tuning on a single platform has not been realized. For the first time, we show that by tuning and optimizing the deposition conditions in inductively-coupled plasma chemical vapor deposition (ICPCVD) of silicon dioxide, this material can be used to deterministically tune the thermo-optic properties of optical devices without introducing significant losses. We demonstrate that we can deterministically integrate positive and negative wavelength shifts on a single chip, validated on amorphous silicon carbide (a-SiC), silicon nitride (SiN) and silicon-on-insulator (SOI) platforms. This enables the fabrication of a novel tunable coupled ring optical waveguide (CROW) requiring only a single heater. In addition, we observe up to a 10-fold improvement of the thermo-optic tunability and demonstrate athermal ring resonators with shifts as low as 1.5 pm/°C. The low-temperature deposition of our silicon dioxide cladding can be combined with lift-off to isolate the optical devices resulting in a decrease in thermal crosstalk by at least two orders of magnitude. Our method paves the way for novel photonic architectures incorporating bidirectional thermo-optic tunability.

5.1. INTRODUCTION

Achieving a high degree of tunability in photonic devices has been a focal point in the field of integrated photonics for several decades with a wide range of applications from telecommunications and biochemical sensing to fundamental quantum photonic experiments in many material platforms[1–17].

The most universally utilized method to achieve photonic device tunability is by exploiting the thermo-optic effect. The thermo-optic coefficient (TOC) of an optical material describes the change in refractive index due to a temperature change (dn/dT)[18–20]. It has been shown that the thermal tunability of a platform depends on the volume expansion of the materials, the temperature-induced refractive index differences, waveguide path-difference variations, the strain between core and cladding material, and their mechanical properties such as Young modulus and Poisson's constant, described with the following relation and simplified [21–24]:

$$\frac{d\lambda}{dT} = \lambda\left(\frac{1}{n_{eff}}\frac{dn_{eff}}{dT} + \alpha_{sub}\right) - \lambda\frac{1}{E}\frac{d\left[\nu\left(\sigma_{xx}+\sigma_{yy}\right)-\sigma_{zz}\right]}{dT} \tag{5.1}$$

where n_{eff} is the effective refractive index at the given wavelength λ, α_{sub} is the thermal expansion coefficient of the substrate, E and ν are the Young modulus and the Poisson's constant of the core, and σ_{xx}, σ_{yy} and σ_{zz} the stress components. In Eq.5.1 the first term on the right-hand side represents the effective thermo-optic coefficient and is the usual term used in literature studies for the stress-free state. In contrast, the second term corresponds to the thermal shift produced by a

stress gradient. Thermal stress arises due to the mismatch between the thermal expansion coefficients of the waveguide and the cladding materials. In the usual configuration to exploit the thermo-optic effect, metal heaters are placed above the guiding material to control the phase of the light. This method of tuning photonic devices is virtually lossless, easy to integrate, and applicable to nearly all photonic platforms. Nevertheless, the tuning strength is specific to the material platform and, importantly, it is weak in photonic platforms such as silicon nitride or silicon dioxide, two of the most commonly used materials in integrated photonics [25, 26]. To compensate for it, hybrid integration with platforms with higher TOC can be performed such that e.g.: delay lines can be fabricated on a low-loss material (SiN) while interference is done on high TOC platforms (a-SiC) [27–29]. Increasing the TOC of materials has been a major challenge and, so far, accomplished by tuning their composition [30, 31] or depositing high refractive index claddings such as silicon oxycarbide (SiOC) [32]. Using TiO_2, a high index cladding, several works achieved SOI athermal devices, where this material cancels out the positive thermal expansion of this photonic platform [33–36]. However, these methods are complex and only applicable to specific platforms. Moreover, changing the composition modifies the overall properties of the guiding layer and often significantly increases the propagation losses, while depositing a high index cladding increases the bending losses and reduces the integration density. Other works have shown that the thermo-optic properties of optical devices can also be modified by applying external thermal stress, with the drawback of presenting multimode operation, birefringence and loss increase [21, 22]. Finally, only positive or negative thermal shifts have been achieved thus far[37–39]; bidirectional tuning on a single platform remains elusive.

In this work we report for the first time that inductively-coupled plasma chemical vapor deposition (ICPECVD) can be used to tailor the thermo-optic properties of optical devices by depositing silicon dioxide claddings, the most common optical material, achieving large positive and negative thermal wavelength shifts on a single chip without significantly affecting the optical losses (depicted in fig.5.1a). We apply this technique on amorphous silicon carbide, silicon nitride and silicon-on-insulator platforms, and demonstrate an up to 10-fold improvement of the thermo-optical wavelength tunability of SiN compared to literature values. Moreover, we demonstrate a 5-fold higher thermal tunability and athermal photonic ring resonators on a-SiC platform. This powerful tunability range allows us to showcase unprecedented photonic devices by deterministically including claddings with negative and positive thermal responses on the same chip. Additionally, thanks to our low-temperature deposition technique, we introduce a novel fabrication approach to isolate active optical devices and demonstrate a decrease in thermal crosstalk by at least two orders of magnitude.

5.2. RESULTS AND DISCUSSION

5.2.1. THERMO-OPTIC WAVELENGTH SHIFT AND PROPAGATION LOSS

Following the general formula for the thermo-optic coefficient in Fig. 5.1b and as demonstrated in other works, applying thermal stress in the cladding can

contribute to controlling the temperature sensitivity of optical devices[21–24]. In CVD techniques it is known that different parameters such as temperature, chamber pressure, gas ratios and RF plasma power can modify the stress profiles in the deposited films [40–44], their morphology (fig.5.1c) such as grain size [45] and density [46] or the chemical composition (fig.5.1d), with nitrogen, hydrogen and incorporation of dopants, overall affecting the thermal expansion properties of the cladding[47, 48]. Most importantly it has been shown that, in ICPCVD, RF plasma power and pressure can also induce noticeable differences in the anisotropy ratio, which relates the film thickness in the sidewall to that of the substrate and could potentially affect the strain profile around the waveguide region [49]. Fig.5.1e shows two scanning electron microscope cross-sections of the deposition of silicon dioxide around the waveguide region. Different chamber pressures of **i** 2.5 mTorr and **ii** 12 mTorr produce noticeable differences in the anisotropy of the cladding. These parameters can also affect other contributing factors such as the thermal expansion coefficient and polarizability [24]. We measure the thermal response of optical ring resonators (radius 120 μm, waveguide width 750 nm, gap 850 nm and, as measured by ellipsometry, thickness of 270 nm) fabricated on a-SiC films and covered with silicon dioxide claddings deposited via ICPCVD and PECVD techniques under different deposition temperatures (Fig. 5.2a) and chamber pressures (Fig. 5.2b). Details about free spectral range, group index, effective index, thermal tunability and device dimensions for a-SiC, SiN and Si platforms can be found in Appendix B together with the calculated effective TOC. For compatibility with the lift-off process, we tune the thermal tunability at a fixed temperature of 150°C by modifying the chamber pressure. We conducted temperature reliability tests for different claddings and found that silicon dioxide claddings deposited at 150°C can withstand temperatures up to 400°C (see Appendix B). At a deposition temperature of 150°C (Fig. 5.2b) we achieve wavelength shifts between +29.5 pm/°C (at 2 mTorr) and -118 pm/°C (at 16 mTorr). Using this approach, we record a thermal shift of -138 pm/°C in a-SiC platform depositing ICPCVD SiO_2 at 300°C and 12 mTorr, corresponding to dn_{eff}/dT = -2.2×10^{-4}RIU/°C. The respective spectra with the detuning of the resonance dip at different temperatures can be seen in Fig. 5.2c. This represents a tunability of almost 5 times higher than standard devices [27] and significantly 22% more than that of silicon [50] (see Appendix B for the fitting). Crucially, for sensing applications, and thanks to the significant thermal tuning from negative to positive, our method allows for the fabrication of athermal devices by choosing the appropriate chamber pressure (3 mTorr) and deposition temperature (150°C). We achieved a thermal response as low as 1.5 pm/°C in a temperature range between 27°C and 35°C, a relevant temperature range for biological and chemical sensing [51] (Fig. 5.2d), which is 20 times lower than the standard PECVD-cladded devices (see Appendix B for individual spectra). In Fig. 5.2a it can be seen that the largest thermal tunability of -166 pm/°C occurs for a deposition temperature of 75°C (temperature raises to 91°C due to table heating). The spectra and fits can be found in Appendix B. For these low temperatures, we find that the device response is not stable, resulting in different TOCs after the temperature is raised. As shown in Appendix B the same is true for a device made on a silicon nitride platform, a

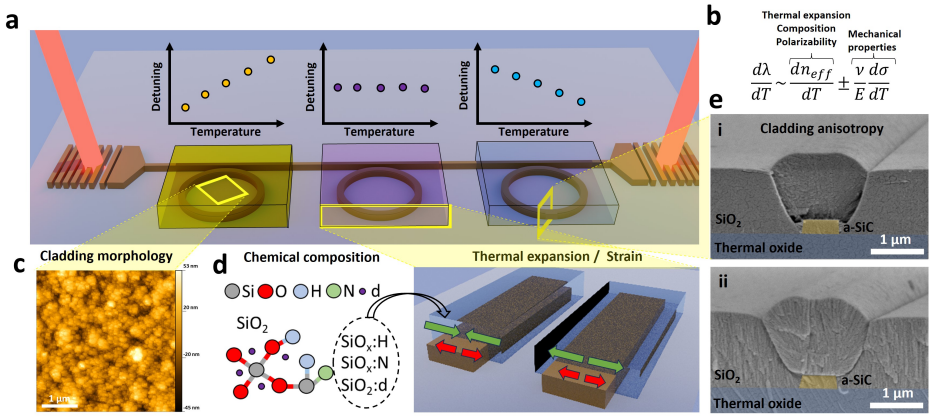

Figure 5.1: **a)** Illustration of the deterministic integration of different claddings on the same chip with positive, athermal and negative detuning. **b)** General formula for the thermal shift in optical devices, proportional to volume expansion, composition, polarizability and mechanical properties [24, 40]. Varying the deposition parameters in CVD techniques can induce changes in the thermal expansion properties of the films due to **c)** the morphology (grain size and topography) [45] and density [46] of the films as shown by our AFM studies, **d)** their chemical composition and bonds with other compounds such as hydrogen, nitrogen or dopants [47, 48] and **e)** cladding anisotropy around the waveguide adding additional strain [23, 49] as has also been observed in our crossectional SEM images of waveguides with ICPCVD silicon dioxide claddings deposited at chamber pressures of **i** 2.5 mTorr, **ii** 12 mTorr.

cladding deposited at 30°C cannot be heated more than 33°C since the thermal shift and hence the tunability decreases.

To demonstrate that this method can be applied to other platforms, we deposit claddings using PECVD and ICPCVD at different temperatures on SOI (width 700 nm and thickness 220 nm with ring radius of 120 μm) and SiN (width 1000 nm and thickness 368 nm with ring radius of 120 μm) platforms and record the detuning of the resonance wavelength for each device as a function of the stage temperature. The resonance wavelength detuning as a function of temperature are shown in Fig. 5.2e and f, respectively. The representative spectra at different temperatures can be found in Appendix B. Fig. 5.2e shows that for SOI optical ring resonators we can achieve thermal shifts between -96 pm/°C (dn_{eff}/dT = -2.2×10^{-4}/°C) for ICPCVD oxide deposited at 75°C and +40 pm/°C for 300°C PECVD oxide cladding.

Similarly, Fig. 5.2f shows that depositing PECVD SiO_2 on SiN devices yields 14 pm/°C, comparable to values found in the literature[52]. In contrast, when this cladding is deposited with ICPCVD at 300°C we achieve a thermal shift of -106 pm/°C, representing an improvement of almost an order of magnitude and a dn_{eff}/dT of -1.2×10^{-4}/°C.

In terms of optical quality, using ICPCVD SiO_2 at a temperature of 150°C and changing the chamber pressure results in devices with similar quality over the pressure range from 2 mTorr to 8 mTorr with waveguide propagation losses of 2.68 dB/cm (Q_{int} = 1.58×10^5, comparable to literature values).

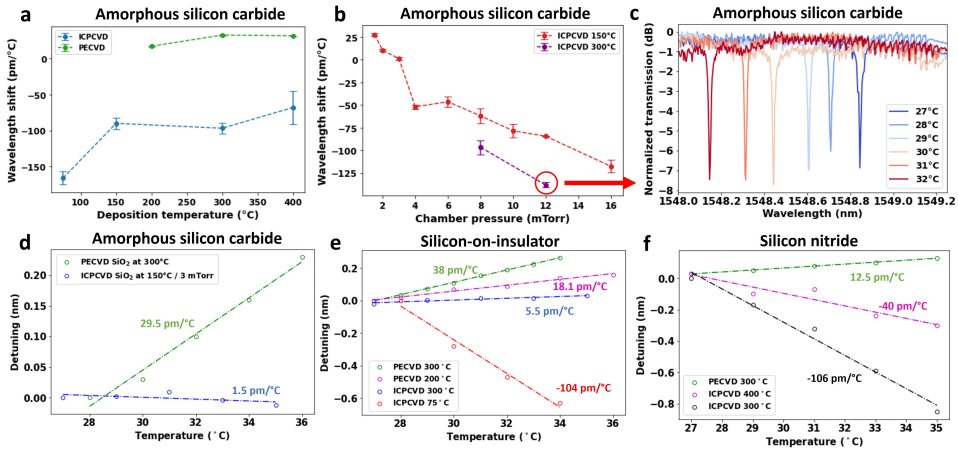

Figure 5.2: **a)** Wavelength shift in pm/°C for a-SiC devices with ICPCVD cladding deposited at different temperatures and a constant chamber pressure of 8 mTorr using ICPCVD (green) and PECVD (blue) together with the standard deviation obtained from the linear fitting. Lines are guides to the eye. **b)** Thermo-optic tunability in pm/°C for a-SiC devices with ICPCVD cladding deposited at different chamber pressures and a temperature of 150°C (red) and 300°C (purple) together with the standard deviation obtained from the linear fitting. **c)** Wavelength spectra of a device with a cladding deposited via ICPCVD at 300°C and 12 mTorr chamber pressure recorded at different temperatures between 27°C and 32°C. **d)** Detuning of the resonance wavelength for a-SiC devices with cladding deposited by PECVD (chamber temperature 300°C; green symbols) and ICPCVD (chamber temperature 150°C and chamber pressure 3 mTorr; blue symbols). Lines are linear fits. **e)** Detuning of the resonance wavelength for silicon-on-insulator optical devices with PECVD and ICPCVD claddings deposited at different temperatures. Lines are linear fits with slopes as indicated. **f)** Detuning of the resonance wavelength for silicon nitride optical devices with PECVD and ICPCVD claddings deposited at different temperatures. Lines are linear fits with slopes as indicated.

5.2.2. PASSIVE AND ACTIVE DEVICES

To highlight the flexibility of our fabrication strategy, we propose the first demonstration of a passive actuated coupled resonator optical waveguide (CROW) device using a single cladding with negative thermal tunability. CROW devices are typically used in optical filtering, dispersion compensation, and non-linear optics [53–56]. In addition, they can be used to delay, store, and buffer photons with controlled times[57]. The basic structure of a CROW device consists of two or more adjacent and coupled ring resonators. Fig. 5.3a shows a device with this configuration and the inset a basic lift-off process using a silicon dioxide cladding deposited at 150°C and 8 mTorr. Lift-off is challenging for CVD methods due to the high deposition temperatures, incompatible with lithography resists [58]. Other techniques such as sputtering can be used, but the number of parameters that can be modified is much more limited and they often lead to lower-quality oxides (unless annealing is performed) and poor step coverage [59, 60]. Fig. 5.3b shows the output spectra as the temperature of the sample is increased from 32.5°C to 34.5°C. In this case, the matching condition is achieved at a temperature of 33.9°C. As another example, we show in Appendix B a Mach-Zehnder interferometer where it is possible to vary the output power in the ports by modifying the stage temperature. In their usual configuration, these devices are tuned with separate micro-heaters on top of the rings. Once the coupling condition is fulfilled, the resonances of each ring overlap, and the photons can be filtered to the output. In contrast, our CROW design incorporating two rings of opposite thermal shifts can be tuned by a single heater. This is done by using a lift-off friendly temperature of 150°C, compatible with lithography resists, but with chamber pressures of 2 mTorr (positive TOC) and 8 mTorr (negative TOC) following Fig. 5.2b.

Using our fabrication scheme, we fabricate a CROW configuration with two claddings (Fig. 5.3c) and similar ring parameters as previously shown. Fig. 5.3d shows an optical microscope image of the final rings with heaters. They are connected in series (or in parallel) having common voltage and common ground. For a device connected in parallel (R=784Ω), sweeping the voltage results in the diagram shown in Fig. 5.3e. This figure represents a 2D map tracking the position of the dips for both rings as the voltage is increased. For a voltage of 6V, the resonance matching condition for both rings is fulfilled. Appendix B includes a similar plot for a device connected in series, displaying similar behavior but requiring a higher operation voltage.

5.2.3. CLADDING LIFT-OFF FOR THERMAL ISOLATION

In standard methods, the cladding is deposited on the whole sample making it challenging to place optical devices close to each other due to thermal crosstalk. Some approaches have shown that, to reduce the thermal crosstalk, the cladding between devices can be etched [61–64] or predictive models can be developed to control their overall response [65–67]. The possibility of defining the cladding using lift-off significantly reduces the design and fabrication complexity.

Due to the low processing temperatures involved in ICPCVD we fabricated a cladding limited to a region of 4μm around the waveguide and studied the

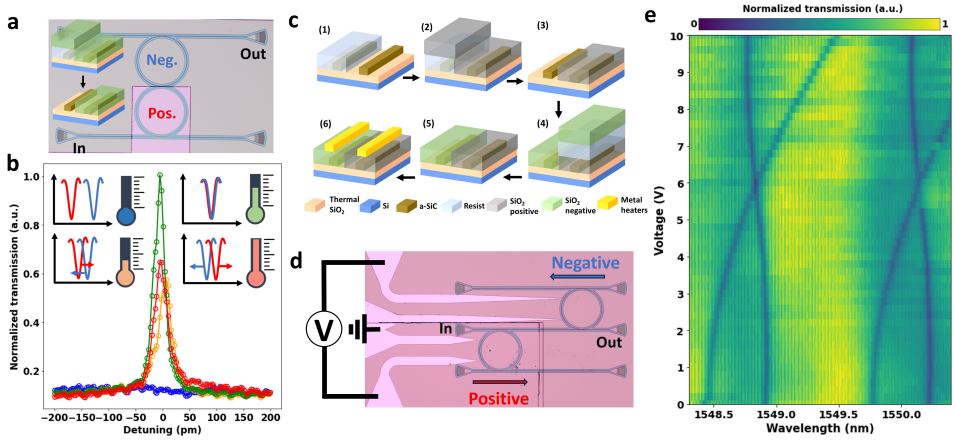

Figure 5.3: **a)** CROW resonator fabricated using bidirectional thermal response with only one cladding. Inset: basic lift-off process with cladding. **b)** Transmission spectra around 1552 nm of the output signal of the device shown in panel d at temperatures of 32.5°C (blue), 33.5°C (orange), 33.9°C (green) and 34.5°C (red). **c)** Fabrication scheme for the inclusion of bidirectional claddings in optical devices. 1) Resist spin coating, exposure and development. 2) SiO_2 cladding deposition for positive shift. 3) Lift-off in acetone. 4) Resist spin-coating, exposure, development and deposition of negative TOC cladding. 5) Lift-off in acetone. 6) Patterning of metal heaters via lift-off. **d)** Optical microscope image of two ring resonators connected with a middle waveguide. **e)** Resonant wavelength as a function of the voltage applied to metal heaters of the optical device shown in panel b (R=784Ω)

thermal response. For reference, we also fabricated ring resonators with standard PECVD cladding. Both ring resonators have a 10 μm separation between adjacent waveguides and dimensions similar to those in previous sections. Fig. 5.4a shows optical images of the devices together with a schematic side-view of the cladding. To determine the thermal crosstalk between adjacent rings, we varied the power dissipated in the heater of ring A (R=1.9kΩ) and observe the thermal response of both rings A and B (Fig. 5.4a). In the case of standard PECVD cladding, the thermal response of rings A and B is 18.5 pm/mW (red line in Fig. 5.4b) and 1.5 pm/mW (red line in Fig. 5.4c), respectively. Similar to PECVD, for a continuous ICPCVD cladding, the thermal response of rings A and B is -22.7 pm/mW (purple line in Fig. 5.4b) and -2.5 pm/mW (purple line in Fig. 5.4c), respectively. By using an ICPCVD cladding with lift-off method, we improve the performance of our device in two ways: we increase the thermal response in ring A (42 pm/mW, green line in Fig. 5.4b) and decrease the thermal response in ring B (no thermal shift visible within a free spectral range, green line in Fig. 5.4c). Therefore, we can thermally isolate two ring resonators placed 10 μm apart by depositing an ICPCVD cladding with the lift-off method, which is not feasible in standard PECVD claddings (see Appendix B for the measured data). Note that the heating efficiency of the on-chip micro-heaters falls outside the scope of this study, and the geometry of the heaters and thickness of the cladding can be modified to significantly raise the ratio between heat generation and power consumption, and optimize the reconfiguration time [68–72].

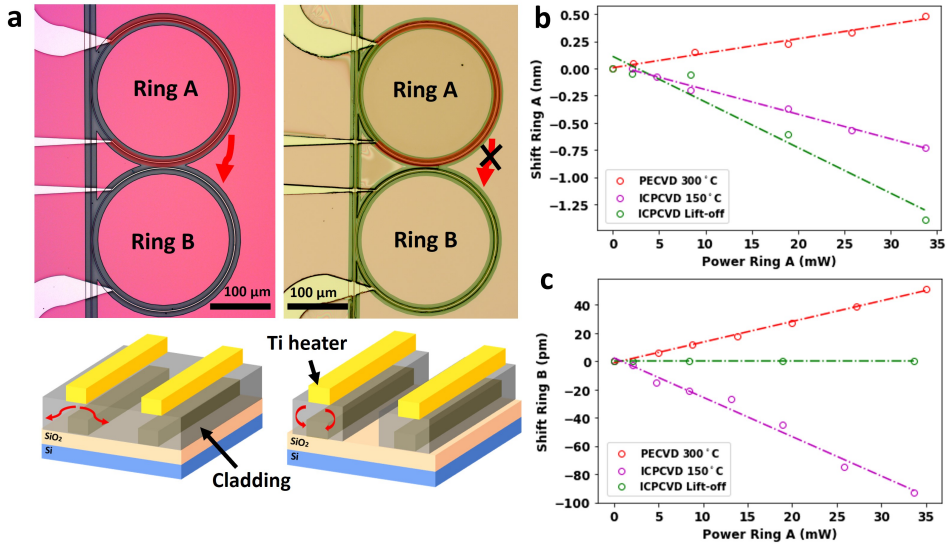

Figure 5.4: **a)** Optical microscope image (top view) of ring resonator devices fabricated using continuous cladding (left) and cladding delimited with lift-off (right). Red arrows denote thermal crosstalk from the micro-heater of R=1.9kΩ. **b)** Detuning as a function of power consumed in ring A fabricated using PECVD (red), ICPCVD (purple) and cladding lift-off (green). **c)** Shift of the adjacent ring due to thermal crosstalk as a function of power consumed in the micro-heater for PECVD (red), ICPCVD (purple) and cladding lift-off (green).

5.3. CONCLUSIONS

We demonstrated, for the first time, the use of ICPCVD silicon dioxide claddings deposited at low temperatures to achieve positive, negative and athermal thermo-optic devices on a single chip with large thermal tunability across several photonic platforms such as amorphous silicon carbide, silicon nitride and silicon-on-insulator. Most importantly, we fabricated both passive and active components. Our approach opens up the possibility for the fabrication of low-power photonic configurations such as Mach-Zehnder interferometers, single-heater CROW optical devices, and highly sensitive temperature sensors that could be easily integrated with current electronic and photonic technologies. Additionally, we showed that the low-temperature fabrication scheme allows to thermally isolate the optical devices to compensate for the high thermal shifts and to increase the photonic integration densities. This study presented a phenomenological approach to tuning the thermal properties of optical devices. While preliminary research into the root cause of the effect is presented in Appendix B, more comprehensive studies are needed to fully unravel the mechanism behind the exciting findings that are reported here. Measurements of film stress, surface morphology and anisotropy ratio of the cladding indicate that these properties could be the main mechanism behind this effect. Nevertheless, to model these devices, it is important to understand other contributions such as the composition and density of the films, hydrogen, nitrogen or dopant incorporation, specific mechanical constants of the deposited films (Young´s modulus and Poisson constant), the strain between the layers and how the device geometry can affect the thermal tunability. With further improvements, we foresee the use of these configurations for novel photonic architectures and widely tunable photonic circuits.

REFERENCES

[1] A. Rizzo, A. Novick, V. Gopal, B. Y. Kim, X. Ji, S. Daudlin, Y. Okawachi, Q. Cheng, M. Lipson, A. L. Gaeta, *et al.*, *Massively scalable kerr comb-driven silicon photonic link,* Nature Photonics **17**, 781 (2023).

[2] M. Lipson, *The revolution of silicon photonics,* Nature Materials **21**, 974 (2022).

[3] S. A. Miller, M. Yu, X. Ji, A. G. Griffith, J. Cardenas, A. L. Gaeta, and M. Lipson, *Low-loss silicon platform for broadband mid-infrared photonics,* Optica **4**, 707 (2017).

[4] X. Ji, Y. Okawachi, A. Gil-Molina, M. Corato-Zanarella, S. Roberts, A. L. Gaeta, and M. Lipson, *Ultra-low-loss silicon nitride photonics based on deposited films compatible with foundries,* Laser & Photonics Reviews **17**, 2200544 (2023).

[5] X. Ji, S. Roberts, M. Corato-Zanarella, and M. Lipson, *Methods to achieve ultra-high quality factor silicon nitride resonators,* APL Photonics **6, 071101** (2021).

[6] B. Stern, X. Ji, A. Dutt, and M. Lipson, *Compact narrow-linewidth integrated laser based on a low-loss silicon nitride ring resonator,* Optics Letters **42**, 4541 (2017).

[7] X. Ji, F. A. Barbosa, S. P. Roberts, A. Dutt, J. Cardenas, Y. Okawachi, A. Bryant, A. L. Gaeta, and M. Lipson, *Ultra-low-loss on-chip resonators with sub-milliwatt parametric oscillation threshold,* Optica **4**, 619 (2017).

[8] A. Klenner, A. S. Mayer, A. R. Johnson, K. Luke, M. R. Lamont, Y. Okawachi, M. Lipson, A. L. Gaeta, and U. Keller, *Gigahertz frequency comb offset stabilization based on supercontinuum generation in silicon nitride waveguides,* Optics Express **24**, 11043 (2016).

[9] K. Luke, Y. Okawachi, M. R. Lamont, A. L. Gaeta, and M. Lipson, *Broadband mid-infrared frequency comb generation in a si 3 n 4 microresonator,* Optics Letters **40**, 4823 (2015).

[10] A. Yi, C. Wang, L. Zhou, Y. Zhu, S. Zhang, T. You, J. Zhang, and X. Ou, *Silicon carbide for integrated photonics,* Applied Physics Reviews **9, 031302** (2022).

[11] A. Yi, Y. Zheng, H. Huang, J. Lin, Y. Yan, T. You, K. Huang, S. Zhang, C. Shen, M. Zhou, *et al.*, *Wafer-scale 4h-silicon carbide-on-insulator (4h–sicoi) platform for nonlinear integrated optical devices,* Optical Materials **107**, 109990 (2020).

[12] Y. Zheng, M. Pu, A. Yi, X. Ou, and H. Ou, *4h-sic microring resonators for nonlinear integrated photonics,* Optics Letters **44**, 5784 (2019).

[13] C. Wang, Z. Fang, A. Yi, B. Yang, Z. Wang, L. Zhou, C. Shen, Y. Zhu, Y. Zhou, R. Bao, *et al.*, *High-q microresonators on 4h-silicon-carbide-on-insulator platform for nonlinear photonics,* Light: Science & Applications **10**, 139 (2021).

[14] D. M. Lukin, C. Dory, M. A. Guidry, K. Y. Yang, S. D. Mishra, R. Trivedi, M. Radulaski, S. Sun, D. Vercruysse, G. H. Ahn, and J. Vučković, *4h-silicon-carbide-on-insulator for integrated quantum and nonlinear photonics,* Nature Photonics **14**, 330 (2019).

[15] P. Rabiei, J. Ma, S. Khan, J. Chiles, and S. Fathpour, *Heterogeneous lithium niobate photonics on silicon substrates,* Optics Express **21**, 25573 (2013).

[16] D. Pohl, M. R. Escalé, M. Madi, F. Kaufmann, P. Brotzer, A. Sergeyev, B. Guldimann, P. Giaccari, E. Alberti, U. Meier, and R. Grange, *An integrated broadband spectrometer on thin-film lithium niobate,* Nature Photonics **14**, 24 (2019).

[17] H. Feng, T. Ge, X. Guo, B. Wang, Y. Zhang, Z. Chen, S. Zhu, K. Zhang, W. Sun, C. Huang, *et al.*, *Integrated lithium niobate microwave photonic processing engine,* Nature , 1 (2024).

[18] F. Qiu, A. M. Spring, and S. Yokoyama, *Athermal and high-q hybrid tio2–si3n4 ring resonator via an etching-free fabrication technique,* ACS Photonics **2**, 405 (2015).

[19] J. T. Robinson, L. Chen, and M. Lipson, *On-chip gas detection in silicon optical microcavities,* Optics Express **16**, 4296 (2008).

[20] J. T. Robinson, K. Preston, O. Painter, and M. Lipson, *First-principle derivation of gain in high-index-contrast waveguides,* Optics Express **16**, 16659 (2008).

[21] M. Huang and X. Yan, *Thermal-stress effects on the temperature sensitivity of optical waveguides,* J. Opt. Soc. Am. B **20**, 1326 (2003).

[22] M. Huang, *Stress effects on the performance of optical waveguides,* International Journal of Solids and Structures **40**, 1615 (2003).

[23] D. Cohen, B. Mason, J. Dolan, C. Burns, and L. Coldren, *Enhanced wavelength tuning of an ingaasp-inp laser with a thermal-strain-magnifying trench,* Applied Physics Letters **77**, 2629 (2000).

[24] J. M. Jewell, *Thermooptic coefficients of some standard reference material glasses,* Journal of the American Ceramic Society **74**, 1689 (1991).

[25] A. Arbabi and L. L. Goddard, *Measurements of the refractive indices and thermo-optic coefficients of si3n4 and siox using microring resonances,* Optics Letters **38**, 3878 (2013).

[26] A. W. Elshaari, I. E. Zadeh, K. D. Jöns, and V. Zwiller, *Thermo-optic characterization of silicon nitride resonators for cryogenic photonic circuits,* IEEE Photonics Journal **8**, 1 (2016).

[27] B. Lopez-Rodriguez, R. van der Kolk, S. Aggarwal, N. Sharma, Z. Li, D. van der Plaats, T. Scholte, J. Chang, S. Gröblacher, S. F. Pereira, H. Bhaskaran, and I. E. Zadeh, *High-quality amorphous silicon carbide for hybrid photonic integration deposited at a low temperature,* ACS Photonics **10**, 3748 (2023).

[28] N. Sharma, Z. Li, B. Lopez-Rodriguez, J. Vrugt, S. H. van der Waal, L. Li, R. van der Kolk, P. J. Poole, D. Dalacu, and I. Esmaeil Zadeh, *Design and validation of a-sic/sin hybrid photonic platform for integrated quantum photonics,* Materials for Quantum Technology , 4, 035401 (2024).

[29] C. Chen, Y. Chen, Z. Fang, R. Ge, J. Wu, and X. Chen, *Hybrid material integration for active photonic applications,* APL Photonics **9, 030903** (2024).

[30] L.-Y. S. Chang, S. Pappert, and P. K. L. Yu, *High thermo-optic tunability in pecvd silicon-rich amorphous silicon carbide,* Opt. Lett. **48**, 1188 (2023).

[31] H. Nejadriahi, A. Friedman, R. Sharma, S. Pappert, Y. Fainman, and P. Yu, *Thermo-optic properties of silicon-rich silicon nitride for on-chip applications,* Optics Express **28**, 24951 (2020).

[32] F. A. Memon, F. Morichetti, and A. Melloni, *High thermo-optic coefficient of silicon oxycarbide photonic waveguides,* ACS Photonics **5**, 2755 (2018).

[33] B. Guha, J. Cardenas, and M. Lipson, *Athermal silicon microring resonators with titanium oxide cladding,* Optics Express **21**, 26557 (2013).

[34] S. Feng, K. Shang, J. T. Bovington, R. Wu, B. Guan, K.-T. Cheng, J. E. Bowers, and S. J. B. Yoo, *Athermal silicon ring resonators cladded with titanium dioxide for 1.3um wavelength operation,* Optics Express **23**, 25653 (2015).

[35] S. S. Djordjevic, K. Shang, B. Guan, S. T. S. Cheung, L. Liao, J. Basak, H.-F. Liu, and S. J. B. Yoo, *Cmos-compatible, athermal silicon ring modulators clad with titanium dioxide,* Optics Express **21**, 13958 (2013).

[36] T. Lipka, L. Moldenhauer, J. Müller, and H. K. Trieu, *Athermal and wavelength-trimmable photonic filters based on tio2-cladded amorphous-soi,* Optics Express **23**, 20075 (2015).

[37] H. Park, J. Jung, Y. Zhang, M. Liu, J. Lee, H. Noh, M. Choi, S. Lee, and H. Park, *Effects of thermally induced phase transition on the negative thermo-optic properties of atomic-layer-deposited tio2 films,* ACS Applied Electronic Materials **4**, 651 (2021).

[38] J. Teng, P. Dumon, W. Bogaerts, H. Zhang, X. Jian, X. Han, M. Zhao, G. Morthier, and R. Baets, *Athermal silicon-on-insulator ring resonators by overlaying a polymer cladding on narrowed waveguides,* Optics Express **17**, 14627 (2009).

[39] P. Alipour, E. S. Hosseini, A. A. Eftekhar, B. Momeni, and A. Adibi, *Temperature-insensitive silicon microdisk resonators using polymeric cladding layers,* in *2009 Conference on Lasers and Electro-Optics and 2009 Conference on Quantum electronics and Laser Science Conference* (IEEE, 2009) pp. 1–2.

[40] D. Guan, A. Bruccoleri, R. Heilmann, and M. Schattenburg, *Stress control of plasma enhanced chemical vapor deposited silicon oxide film from tetraethoxysilane,* Journal of Micromechanics and Microengineering **24**, 027001 (2013).

[41] J. Wei, P. L. Ong, F. E. Tay, and C. Iliescu, *A new fabrication method of low stress pecvd sinx layers for biomedical applications,* Thin Solid Films **516**, 5181 (2008).

[42] S. Greenhorn, E. Bano, V. Stambouli, and K. Zekentes, *Amorphous sic thin films deposited by plasma-enhanced chemical vapor deposition for passivation in biomedical devices,* Materials **17**, 1135 (2024).

[43] K. Mackenzie, D. Johnson, M. DeVre, R. Westerman, and B. Reelfs, *Stress control of si-based pecvd dielectrics,* in *Proceedings of the 207th Electrochemical Society Meeting* (2005) pp. 148–159.

[44] M. Jaikissoon, Ç. Köroğlu, J. A. Yang, K. Neilson, K. C. Saraswat, and E. Pop, *Cmos-compatible strain engineering for monolayer semiconductor transistors,* Nature Electronics **7**, 885 (2024).

[45] D. S. Smith, F. Puech, B. Nait-Ali, A. Alzina, and S. Honda, *Grain boundary thermal resistance and finite grain size effects for heat conduction through porous polycrystalline alumina,* International Journal of Heat and Mass Transfer **121**, 1273 (2018).

[46] V. Zharkov, *On the dependence of the coefficient of thermal expansion on density,* Physics of the Earth and Planetary Interiors **109**, 79 (1998).

[47] I. McKerracher, L. Fu, H. Tan, and C. Jagadish, *Thermal expansion coefficients and composition of sputter-deposited silicon oxynitride thin films,* Journal of Physics D: Applied Physics **43**, 335104 (2010).

[48] H. Bouchard, A. Azelmad, J. F. Currie, M. Meunier, S. Blain, and T. Darwall, *Thermal stress in doped silicate glasses (b, p) deposited by pecvd and lpcvd,* MRS Online Proceedings Library **308**, 63 (1993).

[49] C. Liang, Y. Zhong, Q. Zhong, J. Li, W. Cao, X. Wang, S. Wang, X. Xu, J. Wang, and Y. Cao, *Low-temperature deposition of high-quality sio2 films with a sloped sidewall profile for vertical step coverage,* Coatings **12**, 1411 (2022).

[50] M. W. Pruessner, T. H. Stievater, M. S. Ferraro, and W. S. Rabinovich, *Thermo-optic tuning and switching in soi waveguide fabry-perot microcavities,* Optics Express **15**, 7557 (2007).

[51] M. R. Bryan, J. N. Butt, J. Bucukovski, and B. L. Miller, *Biosensing with silicon nitride microring resonators integrated with an on-chip filter bank spectrometer,* ACS sensors **8**, 739 (2023).

[52] S. T. Ilie, J. Faneca, I. Zeimpekis, T. D. Bucio, K. Grabska, D. W. Hewak, H. M. Chong, and F. Y. Gardes, *Thermo-optic tuning of silicon nitride microring resonators with low loss non-volatile sb 2 s 3 phase change material,* Scientific Reports **12**, 17815 (2022).

[53] R. R. Kumar and H. K. Tsang, *High-extinction crow filters for scalable quantum photonics,* Optics Letters **46**, 134 (2021).

[54] J. Hryniewicz, P. Absil, B. Little, R. Wilson, and P.-T. Ho, *Higher order filter response in coupled microring resonators,* IEEE Photonics Technology Letters **12**, 320 (2000).

[55] B. Little, S. Chu, W. Pan, D. Ripin, T. Kaneko, Y. Kokubun, and E. Ippen, *Vertically coupled glass microring resonator channel dropping filters,* IEEE Photonics Technology Letters **11**, 215 (1999).

[56] C. Madsen and G. Lenz, *Optical all-pass filters for phase response design with applications for dispersion compensation,* IEEE Photonics Technology Letters **10**, 994 (1998).

[57] H. Takesue, N. Matsuda, E. Kuramochi, W. J. Munro, and M. Notomi, *An on-chip coupled resonator optical waveguide single-photon buffer,* Nature Communications **4**, 2725 (2013).

[58] W. Jin, D. D. John, J. F. Bauters, T. Bosch, B. J. Thibeault, and J. E. Bowers, *Deuterated silicon dioxide for heterogeneous integration of ultra-low-loss waveguides,* Optics Letters **45**, 3340 (2020).

[59] M. Sasaki and T. Ehara, *Silicon oxide thin films prepared by vacuum evaporation and sputtering using silicon monoxide,* in *Journal of Physics: Conference Series*, Vol. 417 (IOP Publishing, 2013) p. 012028.

[60] M. Belt, M. L. Davenport, J. E. Bowers, and D. J. Blumenthal, *Ultra-low-loss ta 2 o 5-core/sio 2-clad planar waveguides on si substrates,* Optica **4**, 532 (2017).

[61] G. Gilardi, W. Yao, H. R. Haghighi, X. J. Leijtens, M. K. Smit, and M. Wale, *Deep trenches for thermal crosstalk reduction in inp-based photonic integrated circuits,* Journal of Lightwave Technology **32**, 4864 (2014).

[62] F. Ceccarelli, S. Atzeni, C. Pentangelo, F. Pellegatta, A. Crespi, and R. Osellame, *Low power reconfigurability and reduced crosstalk in integrated photonic circuits fabricated by femtosecond laser micromachining,* Laser & Photonics Reviews **14**, 2000024 (2020).

[63] Q. Wu, L. Zhou, X. Sun, H. Zhu, L. Lu, and J. Chen, *Silicon thermo-optic variable optical attenuators based on mach–zehnder interference structures,* Optics Communications **341**, 69 (2015).

[64] L. Zhao, C. Zhao, J. Liu, Z. Liu, and Y. Chen, *Effect of sputtering pressure on the structure and properties of sio2 films prepared by magnetron sputtering,* Micro & Nano Letters **15**, 872 (2020).

[65] M. Milanizadeh, D. Aguiar, A. Melloni, and F. Morichetti, *Canceling thermal cross-talk effects in photonic integrated circuits,* Journal of Lightwave Technology **37**, 1325 (2019).

[66] I. Teofilovic, A. Cem, D. Sanchez-Jacome, D. Perez-Lopez, and F. Da Ros, *Thermal crosstalk modelling and compensation methods for programmable photonic integrated circuits, 2024, arxiv. arxiv:2404.10589,* arXiv. https://arxiv.org/abs/2404.10589 (accessed November 02, 2024) .

[67] M. Orlandin, A. Cem, V. Curri, A. Carena, F. Da Ros, and P. Bardella, *Thermal crosstalk effects in a silicon photonics neuromorphic network,* in *2023 International Conference on Numerical Simulation of Optoelectronic Devices (NUSOD)* (IEEE, 2023) pp. 43–44.

[68] A. Atabaki, E. S. Hosseini, A. Eftekhar, S. Yegnanarayanan, and A. Adibi, *Optimization of metallic microheaters for high-speed reconfigurable silicon photonics,* Optics Express **18**, 18312 (2010).

[69] L. Cao, A. A. Aboketaf, and S. F. Preble, *Cmos compatible micro-oven heater for efficient thermal control of silicon photonic devices,* Optics Communications **305**, 66 (2013).

[70] R. Alemany, P. Muñoz, D. Pastor, and C. Domínguez, *Thermo-optic phase tuners analysis and design for process modules on a silicon nitride platform,* in *Photonics*, Vol. 8 (MDPI, 2021) p. 496.

[71] J. R. Erickson, V. Shah, Q. Wan, N. Youngblood, and F. Xiong, *Designing fast and efficient electrically driven phase change photonics using foundry-compatible waveguide-integrated microheaters,* Optics Express **30**, 13673 (2022).

[72] Z. Li, H. Chen, J. Wang, H. Lu, and C. Liu, *Compact design of an optical phase shifter packaged with ist microheater used for integrated photonics,* Results in Physics **19**, 103644 (2020).

6

WAVEGUIDE-INTEGRATED SUPERCONDUCTING NANOWIRE SINGLE-PHOTON DETECTORS ON AN AMORPHOUS SILICON CARBIDE PLATFORM

This chapter is based on a manuscript being written by B. Lopez-Rodriguez, Z. Li and I. Esmaeil Zadeh

In this chapter we demonstrate the integration of NbTiN superconducting nanowire single-photon detectors (SNSPDs) exhibiting saturated internal detection efficiency at near-infrared wavelengths of 950 nm with amorphous silicon carbide (a-SiC) waveguides and photonic devices. This integration approach opens promising pathways toward scalable, high-performance photonic systems, beneficial for applications in quantum communication, integrated LiDAR and quantum computing. The manuscript is under preparation.

6.1. INTRODUCTION

Superconducting nanowire single-photon detectors (SNSPDs) represent the state-of-the-art choice for quantum photonic experiments, offering substantial advantages over alternative technologies like transition edge detectors and avalanche photodiodes. SNSPDs provide exceptionally low dark count rates, broad spectral sensitivity from visible to mid-infrared wavelengths, detection efficiencies surpassing 90% between 900 nm and 1550 nm, sub-10 ps timing resolution, rapid recovery times and photon number resolving capabilities [1–5]. All of these properties are critical for single-photon-sensitive applications, including quantum key distribution, light detection and ranging (LiDAR), quantum computing and quantum information [6–11]. SNSPDs are usually integrated inside cryostats, which cool them to a few Kelvin to maintain superconductivity. Optical fibers are aligned to the detectors, often using self-aligned sleeves that position the fiber core directly above each nanowire for efficient coupling. In multi-channel systems, each detector is typically connected to its own fiber, ensuring independent photon input. This setup allows stable, low-loss light delivery into the cryogenic environment while preserving the detector's high efficiency and low noise for different wavelengths [2, 12]. Integrating these detectors onto photonic circuits combines their superior sensitivity and wide detection window with the reconfigurability and scalability inherent to integrated photonics [13].

SNSPDs consist of ultrathin superconducting nanowires, commonly fabricated from materials such as niobium nitride (NbN), niobium titanium nitride (NbTiN), tungsten silicide (WSi), or molybdenum silicide (MoSi), deposited on waveguides or deterministically embedded into waveguides to facilitate efficient coupling of guided optical modes directly to their active detection regions. A SNSPD works by exploiting the transition of a superconducting nanowire into a resistive state upon photon absorption and the behaviour is explained through the hot-spot model [9]. The nanowire, cooled below its critical temperature and biased with a current just under its critical current, remains superconducting with zero resistance until a photontransfers the energy to the material. When absorbed, the photon's energy breaks Cooper pairs and generates a localized "hotspot" where superconductivity is suppressed. As the current passes through the nanowire, the hot-spot grows due to an avalanche effect and this forces the bias current to flow around the hotspot. When the current density exceeds the critical limit, a temporary resistive region develops. The appearance of this resistive section produces a measurable voltage pulse, which serves as the detection signal. After the hotspot cools within picoseconds to nanoseconds, the nanowire returns to its superconducting state,

being able to detect the next photon.

SNSPDs have been successfully integrated in different photonic material platforms such as Si [14–19], SiN [20–27], GaAs [28–33], AlN [34], $LiNbO_3$ [35, 36], Ta_2O_5 [37] and diamond [38–40].

Amorphous silicon carbide (a-SiC) is a promising platform for integration with SNSPDs due to its broad optical transparency extending from the ultraviolet (UV) to mid-infrared (mid-IR), high refractive index (2.4-2.6), relatively low waveguide propagation losses and high third-order non-linearities. Its high refractive index particularly enhances coupling efficiency with nanowire quantum dots in microcavities [41]. In comparison to the traditionally utilized PECVD techniques, a-SiC deposited with ICPCVD yields high-quality film deposition at a lower temperature (150°C) and optical devices with better performance [42].

As has been shown in previous studies, this compatibility opens up the seamless integration of SNSPDs with advanced photonic structures, including adiabatic tapers for hybrid integration with low-loss thin-film SiN [43, 44] and lithium niobate [45]. The integration with lithium niobate is particularly beneficial, allowing heat-free electro-optical modulation and leveraging its strong second- and third-order nonlinear optical properties. In this section we present an alternative material platform suitable for quantum photonics and waveguide-integrated SNSPDs saturating at near-infrared wavelengths of 950 nm. Therefore, matching the emission wavelength of nanowire quantum dots based on InAsP that we characterize in our lab [44].

As a general overview of the applications for the proposed configuration, we fabricated a chip shown in fig.6.1a which can be used for signal demultiplexing with several ring resonators tuned to separate the specific wavelengths (fig.6.1b) directly applied in single-photon biosensing [46], c) high data rate optical communication using time-amplitude demultiplexing (fig.6.1c) [47] and on-chip quantum interference experiments (fig.6.1d) using balanced Mach-Zehnder interferometers to measure the quality of single-photon sources [41].

6.2. SAMPLE FABRICATION

The complete fabrication flow for these devices is described in section 3.2.1 of the Experimental methods and a simplified fabrication process is depicted in Fig. 6.2a. A microscope image illustrating a fabricated Mach-Zehnder interferometer (MZI) on the a-SiC photonic layer is shown in Fig. 6.2b. Additionally, Fig. 6.2c presents a fully fabricated coupled resonator optical waveguide (CROW) device featuring integrated metallic micro-heaters. Ring resonators provide a compact way to study resonance effects, spectral filtering and quality factors; while MZIs serve as versatile interferometric structures for modulation, switching and phase control. Together, they validate the platform's ability to support both passive and active photonic functionalities. Because of limited time and the required modifications to the optical setup, these elements have not yet been fully characterized to assess their performance.

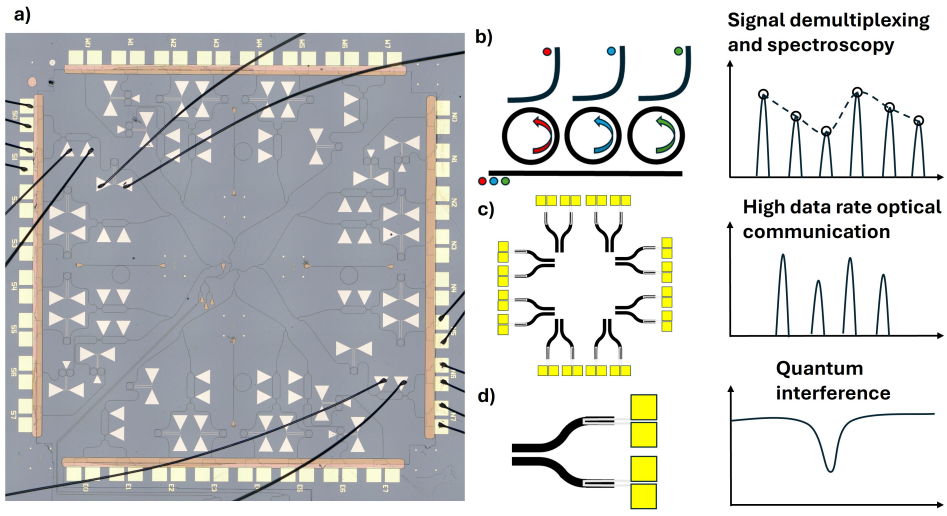

Figure 6.1: a) Optical microscope image of the fabricated chip for several applications such as b) wavelength demultiplexing for spectroscopy and biosensing, c) high data rate optical communication using time-amplitude demultiplexing and d) quantum interference to measure the quality of single-photon sources.

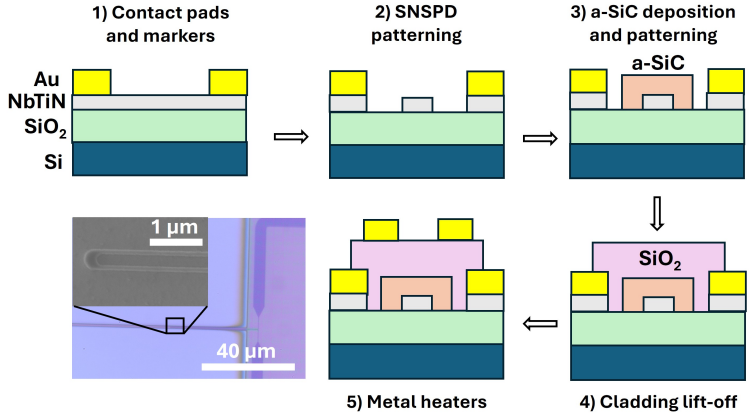

Figure 6.2: Fabrication flow for the integration of SNSPDs with a-SiC photonic devices and optical microscope image of a waveguide integrated SNSPD. Inset: scanning electron microscope image of the nanowire.

6.3. CHARACTERIZATION OF SNSPDS AND RING RESONATORS

The main optical and electrical setup to characterize the SNSPDs with flood illumination is shown in section 3 (Experimental Methods). The first method to characterize the detection response of SNSPDs is through the photon count rate (PCR) curves that measure how detection efficiency depends on the bias current

applied to the detector and the photon flux. At low bias currents, the PCR is low, but it rises sharply as the bias current increases following a sigmoidal curve. Near the critical current, the PCR saturates, reflecting the detector's intrinsic efficiency. At this point, increasing the bias current has no effect in the efficiency of the detector. Fig.6.3a shows the photon count rate curves before and after deposition of ICPCVD a-SiC with an illumination wavelength of 940 nm.

In SNSPDs, the photon energy plays a key role in determining detection efficiency. Higher-energy photons (shorter wavelengths) deposit more energy into the nanowire, producing larger hot spots with more quasiparticles, which makes it easier for the bias current to exceed the local critical current and trigger a resistive transition. This generally leads to higher detection efficiency and lower timing jitter. In contrast, lower-energy photons (longer wavelengths) create smaller hot spots with fewer excitations, which may not be sufficient to drive the nanowire into the normal state unless the device is biased very close to its critical current or specifically engineered for long-wavelength sensitivity. As a result, SNSPDs tend to detect high-energy photons more readily, while detecting low-energy photons requires careful optimization of nanowire geometry, material properties and operating conditions. Fig.6.3b demonstrates these detectors' fabrication and successful operation up to 2000 nm wavelength in a 7 nm NbTiN film without performing waveguide integration.

The second important aspect of these detectors are the dark counts. Dark counts in SNSPDs are false detection events that occur even when no photon is present. They arise mainly from random fluctuations in the superconducting nanowire, such as thermal excitations, stray blackbody radiation or electronic noise, which can create resistive hotspots similar to those caused by real photons. Dark counts set the noise floor of the detector and are typically minimized by cooling to very low temperatures, using proper shielding and optimizing the nanowire design and fabrication process. Fig.6.3c shows the effect of waveguide integration in the dark count rates and critical currents of a detector made on a 9 nm film. Therefore, the photonic integration of the detectors created additional dark counts and a decrease in critical current that could be explained by the introduction of unwanted strain in the superconducting film. More experiments need to be performed to determine the exact process adding this additional strain, such as the deposition of the a-SiC film or that of the silicon dioxide claddings.

Last but equally important is the timing properties of the nanowires know as the time jitter. This metric refers to the uncertainty in the exact arrival time of the detection signal relative to when the photon actually hits the detector. It is caused by variations in hotspot formation, current redistribution, signal propagation along the nanowire and noise in the readout electronics. Lower jitter means more precise timing resolution, which is crucial for applications like quantum communication and time-correlated photon counting. In fig.6.3d we demonstrate a timing jitter of 37.4 ps for a detector with 70 nm wide nanowires in a 9 nm film. Even when this value is larger than previous literature studies [4], the performance can be improved by optimizing the detector geometry and varying film thickness without compromising the detector performance.

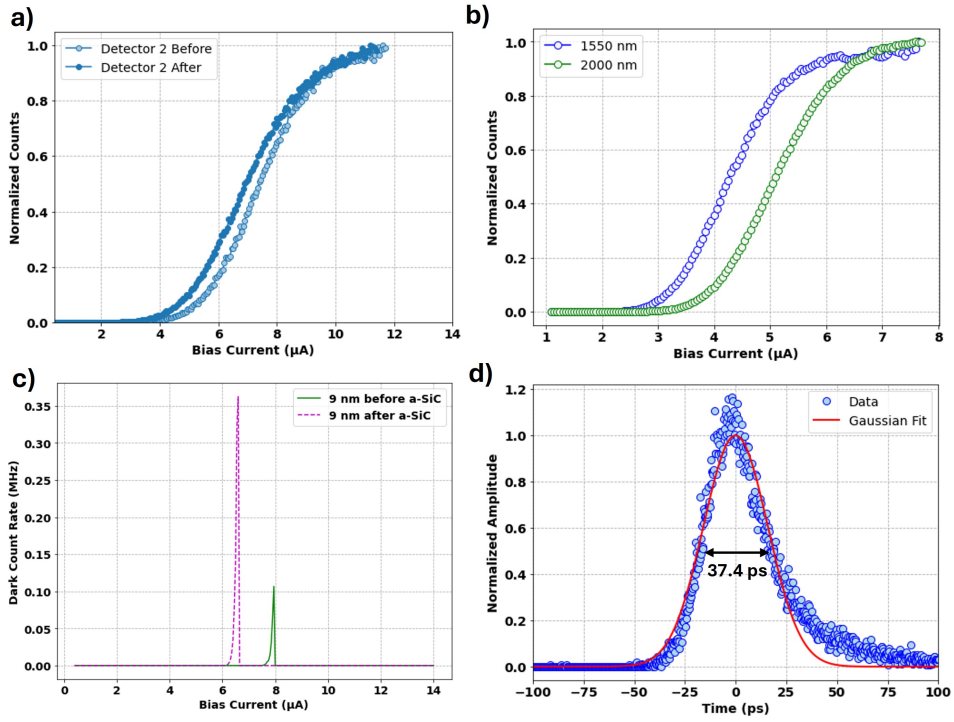

Figure 6.3: a) Photon count rate curves for 940 nm wavelength as a function of the bias current applied to a detector before and after deposition of a-SiC via ICPCVD for 9 nm NbTiN film, b) PCR curves for 1550 nm and 2000 nm wavelength of a hairpin SNSPD fabricated on a 7 nm NbTiN film before a-SiC deposition, c) dark count rates as a function of the bias current applied to the 9 nm SNSPD before and after deposition and d) histogram of time jitter for a detector with 70 nm wide nanowires.

Using this fabrication process, the similarities of the etching recipe of the SNSPDs also create some roughness in the thermal silicon dioxide due to overetch which can affect the quality of the optical layer. To demonstrate that after this etching process does not influence the performance of the optical devices, we measured the transmission spectrum of a ring resonator similar to the one shown in Fig.6.4a using the room temperature setup with grating coupler configuration (see Experimental methods section). The resulting spectrum is shown in Fig.6.4b, from which we obtained a full-width-at-half maximum (FWHM) of 24.4 pm corresponding to a loaded quality factor of 63,524. Comparing this value to standard devices made on this platform shows that the degradation and increased optical losses are related to both the induced roughness in the thermal oxide due to over-etching and the etching quality of the a-SiC film generating sidewall roughness in the waveguides. Nevertheless, the obtained quality factors can still be used for most photonic architectures and fundamental quantum photonic experiments using quantum dots, validating the fabrication process.

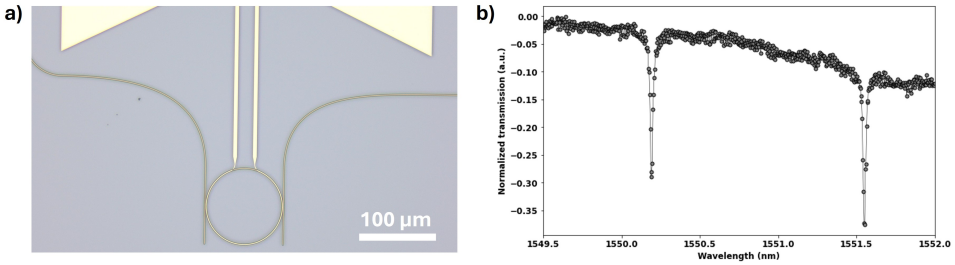

Figure 6.4: a) Optical microscope image of a ring resonator in a drop-port configuration for signal filtering and b) Transmission spectra at room temperature of the through-port of a similar ring resonator fabricated in the same sample with wavelength step size of 4 pm.

6.4. CONCLUSION AND OUTLOOK

This chapter overviews the feasibility of integrating SNSPDs with our recently developed amorphous silicon carbide (a-SiC) photonic platform. In this platform, we have demonstrated all the essential building blocks required to conceive a fully reconfigurable photonic circuit, capable of supporting a wide range of applications including optical communications, quantum photonics, LiDAR, and biosensing. As a next step, our efforts will focus on a systematic characterization of the waveguides, modulators, filters and superconducting nanowire single-photon detectors under cryogenic operating conditions. These studies will allow us to quantify optical losses, assess device stability, evaluate modulation and switching performance and understand the mechanisms that drive SNSPD degradation. Beyond passive and active photonic elements, we will pursue the integration of on-chip nanowire quantum dots as deterministic single-photon sources, enabling quantum light generation for fundamental experiments in quantum optics and information processing. Finally, we will explore hybrid integration strategies, combining our detector arrays with advanced material platforms such as thin-film lithium niobate, to achieve heat-free electro-optic modulation, ultra-low propagation loss and the high-bandwidth needed for next-generation quantum information processors.

Integrating SNSPDs directly onto photonic platforms is highly significant for the future of both classical and quantum technologies. By combining ultrafast, highly efficient single-photon detection with compact, scalable photonic circuits, it becomes possible to build chip-scale systems that are far more stable, compact and energy-efficient than current bulk-optics solutions. There are immediate examples where this integration will be essential. For example, for advancing **quantum communication** and **quantum key distribution**, where reliable detection of single photons is essential for secure information transfer. It also enables large-scale **quantum photonic processors**, since having detectors on the same chip as sources and modulators minimizes coupling losses and improves overall system fidelity.

REFERENCES

[1] I. Esmaeil Zadeh, J. W. Los, R. Gourgues, V. Steinmetz, G. Bulgarini, S. M. Dobrovolskiy, V. Zwiller, and S. N. Dorenbos, *Single-photon detectors combining high efficiency, high detection rates, and ultra-high timing resolution,* Apl Photonics **2, 11** (2017).

[2] J. Chang, J. Los, J. Tenorio-Pearl, N. Noordzij, R. Gourgues, A. Guardiani, J. Zichi, S. Pereira, H. Urbach, V. Zwiller, *et al.*, *Detecting telecom single photons with 99.5- 2.07+ 0.5% system detection efficiency and high time resolution,* APL Photonics **6, 3** (2021).

[3] D. V. Reddy, R. R. Nerem, S. W. Nam, R. P. Mirin, and V. B. Verma, *Superconducting nanowire single-photon detectors with 98% system detection efficiency at 1550 nm,* Optica **7, 12**, 1649 (2020).

[4] I. Esmaeil Zadeh, J. W. Los, R. B. Gourgues, J. Chang, A. W. Elshaari, J. R. Zichi, Y. J. Van Staaden, J. P. Swens, N. Kalhor, A. Guardiani, *et al.*, *Efficient single-photon detection with 7.7 ps time resolution for photon-correlation measurements,* Acs Photonics **7, 7**, 1780 (2020).

[5] J. Los, M. Sidorova, B. Lopez-Rodriguez, P. Qualm, J. Chang, S. Steinhauer, V. Zwiller, and I. E. Zadeh, *High-performance photon number resolving detectors for 850–950 nm wavelength range,* APL Photonics **9, 6** (2024).

[6] F. Grünenfelder, A. Boaron, G. V. Resta, M. Perrenoud, D. Rusca, C. Barreiro, R. Houlmann, R. Sax, L. Stasi, S. El-Khoury, *et al.*, *Fast single-photon detectors and real-time key distillation enable high secret-key-rate quantum key distribution systems,* Nature Photonics **17, 5**, 422 (2023).

[7] S. Ferrari, C. Schuck, and W. Pernice, *Waveguide-integrated superconducting nanowire single-photon detectors,* Nanophotonics **7**, 1725 (2018).

[8] A. McCarthy, G. G. Taylor, J. Garcia-Armenta, B. Korzh, D. V. Morozov, A. D. Beyer, R. M. Briggs, J. P. Allmaras, B. Bumble, M. Colangelo, *et al.*, *High-resolution long-distance depth imaging lidar with ultra-low timing jitter superconducting nanowire single-photon detectors,* Optica **12**, 168 (2025).

[9] I. Esmaeil Zadeh, J. Chang, J. W. Los, S. Gyger, A. W. Elshaari, S. Steinhauer, S. N. Dorenbos, and V. Zwiller, *Superconducting nanowire single-photon detectors: A perspective on evolution, state-of-the-art, future developments, and applications,* Applied Physics Letters **118, 19** (2021).

[10] K. Alexander, A. Bahgat, A. Benyamini, D. Black, D. Bonneau, S. Burgos, B. Burridge, G. Campbell, G. Catalano, A. Ceballos, *et al.*, *A manufacturable platform for photonic quantum computing,* arXiv preprint arXiv:2404.17570 (2024).

[11] L. You, *Superconducting nanowire single-photon detectors for quantum information,* Nanophotonics **9, 9**, 2673 (2020).

[12] J. Chang, J. W. Los, R. Gourgues, S. Steinhauer, S. Dorenbos, S. F. Pereira, H. P. Urbach, V. Zwiller, and I. Esmaeil Zadeh, *Efficient mid-infrared single-photon detection using superconducting nbtin nanowires with high time resolution in a gifford-mcmahon cryocooler,* Photonics Research **10**, 1063 (2022).

[13] S. Gyger, J. Zichi, L. Schweickert, A. W. Elshaari, S. Steinhauer, S. F. Covre da Silva, A. Rastelli, V. Zwiller, K. D. Jöns, and C. Errando-Herranz, *Reconfigurable photonics with on-chip single-photon detectors,* Nature communications **12**, 1408 (2021).

[14] W. H. Pernice, C. Schuck, O. Minaeva, M. Li, G. Goltsman, A. Sergienko, and H. Tang, *High-speed and high-efficiency travelling wave single-photon detectors embedded in nanophotonic circuits,* Nature communications **3**, 1325 (2012).

[15] C. Schuck, W. H. Pernice, O. Minaeva, M. Li, G. Gol'Tsman, A. V. Sergienko, and H. X. Tang, *Matrix of integrated superconducting single-photon detectors with high timing resolution,* IEEE transactions on applied superconductivity **23**, 2201007 (2013).

[16] A. Vetter, S. Ferrari, P. Rath, R. Alaee, O. Kahl, V. Kovalyuk, S. Diewald, G. N. Goltsman, A. Korneev, C. Rockstuhl, *et al.*, *Cavity-enhanced and ultrafast superconducting single-photon detectors,* Nano letters **16**, 7085 (2016).

[17] M. K. Akhlaghi, E. Schelew, and J. F. Young, *Waveguide integrated superconducting single-photon detectors implemented as near-perfect absorbers of coherent radiation,* Nature communications **6**, 8233 (2015).

[18] S. Buckley, J. Chiles, A. N. McCaughan, G. Moody, K. L. Silverman, M. J. Stevens, R. P. Mirin, S. W. Nam, and J. M. Shainline, *All-silicon light-emitting diodes waveguide-integrated with superconducting single-photon detectors,* Applied Physics Letters **111, 14** (2017).

[19] J. Li, R. A. Kirkwood, L. J. Baker, D. Bosworth, K. Erotokritou, A. Banerjee, R. M. Heath, C. M. Natarajan, Z. H. Barber, M. Sorel, *et al.*, *Nano-optical single-photon response mapping of waveguide integrated molybdenum silicide (mosi) superconducting nanowires,* Optics express **24**, 13931 (2016).

[20] O. Kahl, S. Ferrari, V. Kovalyuk, A. Vetter, G. Lewes-Malandrakis, C. Nebel, A. Korneev, G. Goltsman, and W. Pernice, *Spectrally multiplexed single-photon detection with hybrid superconducting nanophotonic circuits,* Optica **4**, 557 (2017).

[21] O. Kahl, S. Ferrari, V. Kovalyuk, G. N. Goltsman, A. Korneev, and W. H. Pernice, *Waveguide integrated superconducting single-photon detectors with high internal quantum efficiency at telecom wavelengths,* Scientific reports **5**, 10941 (2015).

[22] S. Ferrari, O. Kahl, V. Kovalyuk, G. N. Goltsman, A. Korneev, and W. H. Pernice, *Waveguide-integrated single-and multi-photon detection at telecom wavelengths using superconducting nanowires,* Applied physics letters **106, 15** (2015).

[23] C. Schuck, W. H. Pernice, X. Ma, and H. X. Tang, *Optical time domain reflectometry with low noise waveguide-coupled superconducting nanowire single-photon detectors,* Applied Physics Letters **102, 19** (2013).

[24] C. Schuck, X. Guo, L. Fan, X. Ma, M. Poot, and H. X. Tang, *Quantum interference in heterogeneous superconducting-photonic circuits on a silicon chip,* Nature communications **7**, 10352 (2016).

[25] C. Schuck, W. H. Pernice, and H. X. Tang, *Waveguide integrated low noise nbtin nanowire single-photon detectors with milli-hz dark count rate,* Scientific reports **3**, 1893 (2013).

[26] A. D. Beyer, R. M. Briggs, F. Marsili, J. D. Cohen, S. M. Meenehan, O. J. Painter, and M. D. Shaw, *Waveguide-coupled superconducting nanowire single-photon detectors,* in *2015 Conference on Lasers and Electro-Optics (CLEO)* (IEEE, 2015) pp. 1–2.

[27] J. M. Shainline, S. M. Buckley, N. Nader, C. M. Gentry, K. C. Cossel, J. W. Cleary, M. Popović, N. R. Newbury, S. W. Nam, and R. P. Mirin, *Room-temperature-deposited dielectrics and superconductors for integrated photonics,* Optics Express **25**, 10322 (2017).

[28] J. Sprengers, A. Gaggero, D. Sahin, S. Jahanmirinejad, G. Frucci, F. Mattioli, R. Leoni, J. Beetz, M. Lermer, M. Kamp, *et al.*, *Waveguide superconducting single-photon detectors for integrated quantum photonic circuits,* Applied Physics Letters **99, 18** (2011).

[29] S. Jahanmirinejad, G. Frucci, F. Mattioli, D. Sahin, A. Gaggero, R. Leoni, and A. Fiore, *Photon-number resolving detector based on a series array of superconducting nanowires,* Applied Physics Letters **101, 7** (2012).

[30] D. Sahin, A. Gaggero, Z. Zhou, S. Jahanmirinejad, F. Mattioli, R. Leoni, J. Beetz, M. Lermer, M. Kamp, S. Höfling, *et al.*, *Waveguide photon-number-resolving detectors for quantum photonic integrated circuits,* Applied Physics Letters **103, 11** (2013).

[31] G. Reithmaier, M. Kaniber, F. Flassig, S. Lichtmannecker, K. Mu¨ller, A. Andrejew, J. Vuckovic, R. Gross, and J. Finley, *On-chip generation, routing, and detection of resonance fluorescence,* Nano letters **15**, 5208 (2015).

[32] G. E. Digeronimo, M. Petruzzella, S. Birindelli, R. Gaudio, S. Fattah Poor, F. W. Van Otten, and A. Fiore, *Integration of single-photon sources and detectors on gaas,* in *Photonics*, Vol. 3 (MDPI, 2016) p. 55.

[33] M. Kaniber, F. Flassig, G. Reithmaier, R. Gross, and J. J. Finley, *Integrated superconducting detectors on semiconductors for quantum optics applications,* Applied Physics B **122**, 1 (2016).

[34] F. Najafi, J. Mower, N. C. Harris, F. Bellei, A. Dane, C. Lee, X. Hu, P. Kharel, F. Marsili, S. Assefa, *et al.*, *On-chip detection of non-classical light by scalable integration of single-photon detectors,* Nature communications **6**, 5873 (2015).

[35] M. Tanner, L. S. E. Alvarez, W. Jiang, R. Warburton, Z. Barber, and R. Hadfield, *A superconducting nanowire single photon detector on lithium niobate,* Nanotechnology **23**, 505201 (2012).

[36] A. A. Sayem, R. Cheng, S. Wang, and H. X. Tang, *Lithium-niobate-on-insulator waveguide-integrated superconducting nanowire single-photon detectors,* Applied Physics Letters **116, 15** (2020).

[37] M. A. Wolff, S. Vogel, L. Splitthoff, and C. Schuck, *Superconducting nanowire single-photon detectors integrated with tantalum pentoxide waveguides,* Scientific Reports **10**, 17170 (2020).

[38] O. Kahl, S. Ferrari, P. Rath, A. Vetter, C. Nebel, and W. H. Pernice, *High efficiency on-chip single-photon detection for diamond nanophotonic circuits,* Journal of Lightwave Technology **34**, 249 (2016).

[39] P. Rath, O. Kahl, S. Ferrari, F. Sproll, G. Lewes-Malandrakis, D. Brink, K. Ilin, M. Siegel, C. Nebel, and W. Pernice, *Superconducting single-photon detectors integrated with diamond nanophotonic circuits,* Light: Science & Applications **4**, e338 (2015).

[40] H. A. Atikian, S. Meesala, M. J. Burek, Y.-I. Sohn, J. Israelian, A. S. Patri, N. Clarke, A. Sipahigil, R. E. Evans, D. Sukachev, *et al.*, *Novel fabrication of diamond nanophotonics coupled to single-photon detectors,* SPIE Newsroom (2017).

[41] I. E. Zadeh, A. W. Elshaari, K. D. Jons, A. Fognini, D. Dalacu, P. J. Poole, M. E. Reimer, and V. Zwiller, *Deterministic integration of single photon sources in silicon based photonic circuits,* Nano letters **16**, 2289 (2016).

[42] B. Lopez-Rodriguez, R. Van Der Kolk, S. Aggarwal, N. Sharma, Z. Li, D. Van Der Plaats, T. Scholte, J. Chang, S. Gro¨blacher, S. F. Pereira, *et al.*, *High-quality amorphous silicon carbide for hybrid photonic integration deposited at a low temperature,* ACS photonics **10**, 3748 (2023).

[43] Z. Li, B. Lopez-Rodriguez, N. Sharma, and I. Esmaeil-Zadeh, *Heterogeneous interconnection of low-loss and dense material platforms using adiabatic tapering coupler,* in *EPJ Web of Conferences*, Vol. 287 (EDP Sciences, 2023) p. 01014.

[44] N. Sharma, Z. Li, B. Lopez-Rodriguez, J. Vrugt, S. van der Waal, L. Li, R. van der Kolk, P. J. Poole, D. Dalacu, and I. E. Zadeh, *Design and validation of a-sic/sin hybrid photonic platform for integrated quantum photonics,* Materials for Quantum Technology **4**, 035401 (2024).

[45] Z. Li, N. Sharma, B. Lopez-Rodriguez, R. van der Kolk, T. Scholte, H. Voncken, J. van der Boom, S. Gröblacher, and I. E. Zadeh, *Heterogeneous integration of amorphous silicon carbide on thin film lithium niobate,* APL Photonics **10, 1** (2025).

[46] M. R. Bryan, J. N. Butt, J. Bucukovski, and B. L. Miller, *Biosensing with silicon nitride microring resonators integrated with an on-chip filter bank spectrometer,* ACS sensors **8**, 739 (2023).

[47] J. Nunn, L. Wright, C. Söller, L. Zhang, I. Walmsley, and B. Smith, *Large-alphabet time-frequency entangled quantum key distribution by means of time-to-frequency conversion,* Optics express **21**, 15959 (2013).

7

OUTLOOK AND CONCLUSION

7.1. OUTLOOK

To highlight several possibilities in hybrid photonic integration of our platform for different applications, this section briefly summarizes the works that followed our primary research on the deposition of high-quality a-SiC films and are part of collaborations or current research projects in our group. Combining amorphous silicon carbide films with polymers was done at VU Amsterdam and TU Delft sent high-quality films. The integration of a-SiC with lithium niobate and with silicon nitride are both research lines developed in our group at TU Delft.

7.1.1. POLYMERS

Mohammad Talebi Khoshmehr et al. [1] presented an etch-less method with a novel hybrid optical waveguide configuration that enhances functionality and performance in photonic integrated circuits. Traditional optical waveguides rely on high-index material etching, limiting their versatility and increasing propagation losses due to fabrication imperfections. This work integrates a low-index, easily processable SU8 polymer with an amorphous silicon carbide (a-SiC) guiding layer, eliminating the need for etching. The hybrid design significantly enhances polarization control, achieving a transverse magnetic mode suppression of 62 dB at 1550 nm which simplifies optical measurements. Additionally, the waveguide demonstrates a 2.5× improvement in coupling efficiency compared to untapered SiC waveguides. The authors further optimize performance through thermal baking, reducing scattering losses from 1.57 to 1.3 dB/cm. These advancements make the hybrid waveguide an attractive alternative for low-loss, polarization-sensitive, and highly efficient photonic devices, particularly for applications requiring precise mode shaping and dispersion control. The study's findings contribute to the development of next-generation photonic systems, with implications for quantum photonics, biosensing, and high-density optical circuits.

7.1.2. LITHIUM NIOBATE

Zizheng Li et al. [2] demonstrate the heterogeneous integration of amorphous silicon carbide (a-SiC) on thin-film lithium niobate (TFLN), offering a scalable and CMOS-compatible platform for high-speed reprogrammable photonic integrated circuits (PICs). Lithium niobate is widely recognized for its exceptional electro-optic properties, fast modulation and second-order nonlinearity, but the processing of this material remains challenging due to etching limitations and incompatibility with standard CMOS fabrication techniques. By depositing a-SiC using low-temperature inductively coupled plasma-enhanced chemical vapor deposition (ICPCVD), this work circumvents these challenges, enabling high-performance photonic devices without compromising the integrity of the lithium niobate substrate. The fabricated a-SiC/LN waveguides and ring resonators achieve intrinsic quality factors exceeding 1.06×10^5 and demonstrate resonance electro-optic tunability of 3.4 pm/V. The platform supports dense integration, allowing the realization of compact photonic structures down to 40 μm bending radius while maintaining low loss. The demonstrated approach holds significant promise for advanced applications in reconfigurable photonics, nonlinear optics, and quantum information processing, leveraging both second- and third-order nonlinearities on a single chip.

7.1.3. SILICON NITRIDE

Zizheng Li et. al [3] introduced an adiabatic tapering coupler designed to enable bidirectional, low-loss optical interconnection between thin-film silicon nitride (Si3N4) and amorphous silicon carbide (a-SiC) photonic platforms. While Si3N4 is well known for its ultra-low propagation loss (1 dB/m), it suffers from weak mode confinement, limiting its integration density. In contrast, a-SiC offers higher refractive index contrast, much higher thermo-optic tuning coefficient and stronger mode confinement, making it ideal for compact photonic circuits. With an adiabatic transition between these two materials, the proposed coupler achieves a high coupling efficiency at telecom wavelengths of 1550 nm, higher than 96%, with minimal insertion loss. The design is optimized through numerical simulations, showing efficient mode transfer with negligible losses even at tight bending radii (0.29% loss at a 90° bend with a 20 μm radius). In another publication, Zizheng Li, Naresh Sharma et al. [4] also investigated the incorporation of quantum dots (QDs) and superconducting nanowire single-photon detectors (SNSPDs) within this hybrid platform. Through experiments and simulations, the authors demonstrate an adiabatic coupler that efficiently transfers light between SiN and a-SiC waveguides with a coupling efficiency of 96% at 885 nm. Moreover, the work characterizes nanowire quantum dots, showing high single-photon purity ($g(2)(0) = 0.011$) and a short lifetime (0.98 ns). By transferring these sources, this hybrid approach would enable advanced on-chip quantum optics experiments such as Hong–Ou–Mandel interference, while addressing key challenges in integrating low-loss and high-confinement photonic platforms.

7.2. CONCLUSION OF THE THESIS

In this thesis we started by optimizing the deposition of amorphous silicon carbide films using PECVD and ICPCVD to make high quality and low propagation loss optical devices. We then used this platform to fabricate standard waveguides and ring resonators, focusing on the telecom range, and more precisely, 1550 nm. To increase the tunability of the photonic devices, we developed a deposition recipe for silicon dioxide that can be used to deterministically address optical devices on a single chip, achieving up to a ten-fold improvement in the thermal tunability, athermal devices and bi-directional thermal response. To finish, we integrated superconducting single photon detectors on this platform for future quantum experiments. The main achievements of this thesis are:

1) We developed high quality amorphous silicon carbide films using the novel technique ICPCVD. The deposition with this tool enabled lower temperature processes than standard PECVD techniques, from 300°C to 150°C. The optimization was performed by controlling the plasma power, chamber pressure, gas ratios and deposition temperature aiming to increase the refractive index of the films, reduce the grain sizes and achieve low surface roughness. In parallel to this optimization process, we fabricated photonic waveguides, ring resonators and grating couplers to verify the platform's performance. We achieved three times higher quality factors above $4.7x10^5$ compared to ring resonators made on a standard PECVD a-SiC platform with the highest intrinsic quality factor of $5.7x10^5$, corresponding to waveguide propagation losses of less than 1 dB/cm. We demonstrated how this process, combined with a lift-off technique, can embed the deposited films into silicon nitride, or any other platform, to protect optical devices in hybrid photonic systems. The low-temperature deposition of the films will allow the combination with many more material platforms than before, including quantum dots based on III-V materials and superconducting single-photon detectors.

2) We developed a silicon dioxide deposition recipe using ICPCVD that can be used to tune the thermal properties of ring resonators and that is universally applicable to any platform that uses the thermo-optic effect. To achieve this, we varied the deposition temperature and pressure of the cladding and measured the thermal response of the resonance wavelength in ring resonators. The highest thermal shift recorded was -138 pm/°C on a-SiC for a deposition temperature of 300°C and a chamber pressure of 12 mTorr, representing 5 times higher thermal shift than standard devices fabricated using PECVD silicon dioxide claddings. On a silicon nitride platform, we demonstrated that we can achieve a ten fold improvement in the thermal tunability with -106 pm/°C. To determiniscally address the specific devices, we selected a temperature of 150°C in order to be compatible with a lift-off process and demonstrated that we can achieve both positive and negative thermal shifts. Most importantly, we fabricated a novel CROW device configuration using this approach that can be tuned using only a single heater. Finally, to address the high thermal crosstalk inherent to this platform, we showcase an integration approach based on lift-off to thermally isolate optical devices and allow for high integration densities.

3) We integrated superconducting nanowire single photon detectors on amorphous

silicon carbide and demonstrated their performance from 940 nm to 2000 nm.

The platform developed during this thesis provides a stepping stone for further development of basic technologies that can potentially reach the market.

7.3. CHALLENGES AND OPPORTUNITIES

Whenever a new platform is developed, there are challenges and opportunities ahead. With all the information and literature review provided in this thesis it is a requirement to ask what disadvantages arise, possibilities to solve them and opportunities for future advancements.

1) Even with the drawback of transfer bonding, crystalline silicon carbide will still be the platform of choice for integrated photonics, mainly for the high second-order non-linearities, possibility to integrate with CMOS electronics and the existence of well-known single photon sources based on vacancy centers. To address the issue with single-photon centers, several works have implemented them using irradiation techniques [5], ion implantation [6], femtosecond laser writing [7] or in-situ defect incorporation during deposition. Another approach could be to irradiate the devices with erbium ions that could potentially induce the creation of color centers [8]. A more comprehensive overview of single photon centers on silicon carbide can be found in literature studies [9].

2) While developing the amorphous silicon carbide high-quality films, the focus was on telecom wavelengths. As we move closer to the demands of current quantum technologies, it is imperative to start thinking about improving the optical performance at wavelength matching today´s state-of-the-art single photon emitters. It is a requirement to put effort into decreasing the waveguide propagation losses at near-infrared and eventually visible wavelengths for their use with quantum dot sources and color centers. Similarly, with the current advancement of detectors, mid-infrared operation should also be addressed for sensing applications [10].

3) To further decrease the losses, it is known that using nitrogen-based precursors will incorporate this element into the deposited films. As shown in works with silicon nitride, deuterated or chlorine-based precursors will lower the waveguide propagation losses [11, 12].

4) Another implication of using CVD techniques for the deposition of amorphous silicon carbide is the feasibility to introduce nitrogen dopants in the films [13, 14]. While the effect on the optical quality is still unknown, it could enable the possibility of making conductive dielectric films to directly affect the device functionality using electrical contacts. Future studies should look into the effect in optical quality and electrical conductivity as nitrogen is incorporated during deposition. Most importantly, the fabrication of electrically tunable ring resonators, multimode interferometers and heating elements should be experimentally verified.

5) While we obtained high thermal tunability devices using silicon dioxide claddings, it will be important to understand the device temporal dynamics and the relation of heat dissipation, reconfiguration time and oxide deposition parameters.

6) Thermo-optic measurements at room temperature are not valid for lower temperatures. To properly characterize and simulate the claddings and combine them with superconducting detectors, the next step should be to characterize them

at cryogenic temperatures [15].

A natural progression for future research would involve addressing these challenges systematically, ensuring that silicon carbide-based integrated photonic platforms meet the requirements of emerging quantum technologies. Investigating methods to enhance non-linearities in the material, optimizing waveguide designs and deposition recipes to reduce the propagation losses across multiple wavelength ranges, and understanding thermal tunability mechanisms will be essential. Additionally, exploring cryogenic characterization techniques will provide deeper insight into the device performance.

REFERENCES

[1] M. T. Khoshmehr, M. M. Dashtabi, H. Nikbakht, B. L. Rodriguez, N. Sharma, I. E. Zadeh, B. van Someren, and B. I. Akca, *Versatile hybrid optical waveguides in amorphous silicon carbide with enhanced functionality and performance,* Applied Physics Letters **125, 11** (2024).

[2] Z. Li, N. Sharma, B. Lopez-Rodriguez, R. van der Kolk, T. Scholte, H. Voncken, J. van der Boom, S. Gröblacher, and I. E. Zadeh, *Heterogeneous integration of amorphous silicon carbide on thin film lithium niobate,* APL Photonics **10, 1** (2025).

[3] Z. Li, B. Lopez-Rodriguez, N. Sharma, and I. Esmaeil-Zadeh, *Heterogeneous interconnection of low-loss and dense material platforms using adiabatic tapering coupler,* in *EPJ Web of Conferences*, Vol. 287 (EDP Sciences, 2023) p. 01014.

[4] N. Sharma, Z. Li, B. Lopez-Rodriguez, J. Vrugt, S. van der Waal, L. Li, R. van der Kolk, P. J. Poole, D. Dalacu, and I. E. Zadeh, *Design and validation of a-sic/sin hybrid photonic platform for integrated quantum photonics,* Materials for Quantum Technology **4**, 035401 (2024).

[5] C. Kasper, D. Klenkert, Z. Shang, D. Simin, A. Gottscholl, A. Sperlich, H. Kraus, C. Schneider, S. Zhou, M. Trupke, *et al.*, *Influence of irradiation on defect spin coherence in silicon carbide,* Physical Review Applied **13**, 044054 (2020).

[6] V. Chandrasekaran, M. Titze, A. R. Flores, D. Campbell, J. Henshaw, A. C. Jones, E. S. Bielejec, and H. Htoon, *High-yield deterministic focused ion beam implantation of quantum defects enabled by in situ photoluminescence feedback,* Advanced Science **10**, 2300190 (2023).

[7] S. Castelletto, A. F. M. Almutairi, K. Kumagai, T. Katkus, Y. Hayasaki, B. Johnson, and S. Juodkazis, *Photoluminescence in hexagonal silicon carbide by direct femtosecond laser writing,* Optics letters **43**, 6077 (2018).

[8] A. Kaloyeros, S. Dutta, *et al.*, *Engineering and polarization properties of erbium-implanted lithium niobate films for integrated quantum applications,* APL Materials **12, 11** (2024).

[9] S. Castelletto, *Silicon carbide single-photon sources: challenges and prospects,* Materials for Quantum Technology **1**, 023001 (2021).

[10] K. A. Buzaverov, A. S. Baburin, E. V. Sergeev, S. S. Avdeev, E. S. Lotkov, S. V. Bukatin, I. A. Stepanov, A. B. Kramarenko, A. S. Amiraslanov, D. V. Kushnev, *et al.*, *Silicon nitride integrated photonics from visible to mid-infrared spectra,* Laser & Photonics Reviews **18**, 2400508 (2024).

[11] D. Bose, M. W. Harrington, A. Isichenko, K. Liu, J. Wang, N. Chauhan, Z. L. Newman, and D. J. Blumenthal, *Anneal-free ultra-low loss silicon nitride integrated photonics,* Light: Science & Applications **13**, 156 (2024).

[12] D. K. Ng, H. Gao, P. Xing, G. F. Chen, X. X. Chia, Y. Cao, K. Y. Ong, and D. T. Tan, *Enhanced photonics devices based on low temperature plasma-deposited dichlorosilane-based ultra-silicon-rich nitride (si8n),* Scientific Reports **12**, 5267 (2022).

[13] J. Šafránkováa, J. Hurana, I. Hotovỳb, A. Kobzevc, and S. Korenevc, *Characterization of nitrogen-doped amorphous silicon carbide thin films,* Vacuum **51**, 165 (1998).

[14] V. Ivashchenko, P. Turchi, R. Shevchenko, L. Gorb, J. Leszczynski, and A. Kozak, *An effect of nitrogen incorporation on the structure and properties of amorphous sic: First-principles molecular dynamics simulations,* Thin Solid Films **756**, 139349 (2022).

[15] A. W. Elshaari, I. E. Zadeh, K. D. Jöns, and V. Zwiller, *Thermo-optic characterization of silicon nitride resonators for cryogenic photonic circuits,* IEEE Photonics Journal **8**, 1 (2016).

A

Supplementary information: High quality amorphous silicon carbide for hybrid photonic integration deposited at a low temperature

A

Table of contents

A.1. DEPOSITION RECIPES AND ELLIPSOMETRY DATA

The deposition of amorphous silicon carbide films in PECVD was done using a mixture of SiH_4 (15 sccm), CH_4 (75 sccm) and Ar (285 sccm) with temperatures ranging between 300°C and 400°C. The chamber pressure was kept in all recipes at 1000 mTorr with a forward plasma power (PFW) of 20W. The average deposition rates were 39 nm/min. An example for the effect in optical properties (refractive index and extinction coefficient) upon the variation of Si/C ratio during PECVD deposition is shown in fig.S1.

For the deposition of ICPCVD a-SiC films, the same mixture was applied with 15 sccm of SiH_4, 10 sccm of CH_4, at temperatures ranging between 150°C and 400°C. In this case, an Ar flow close to the sample (Arring) was choose to be 11 sccm while the Ar flow in the chamber was 10 sccm. The chamber pressure was kept at 2 mTorr for all recipes with a forward plasma power of 750 W. The average deposition rates were 37 nm/min. In fig.S2 it can be seen that lowering the temperature lowers the roughness in the films with a minimum at 150°C.

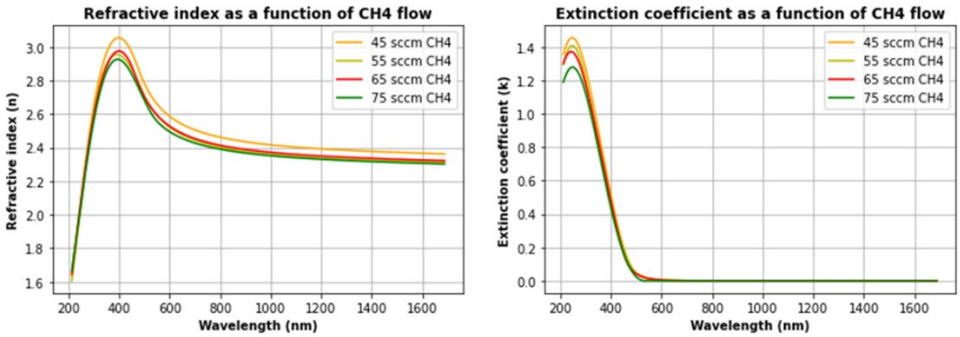

Figure S. A.1: Refractive index and loss coefficient of a-SiC films deposited at 300°C with PECVD as a function of methane flow for a fixed silane flow.

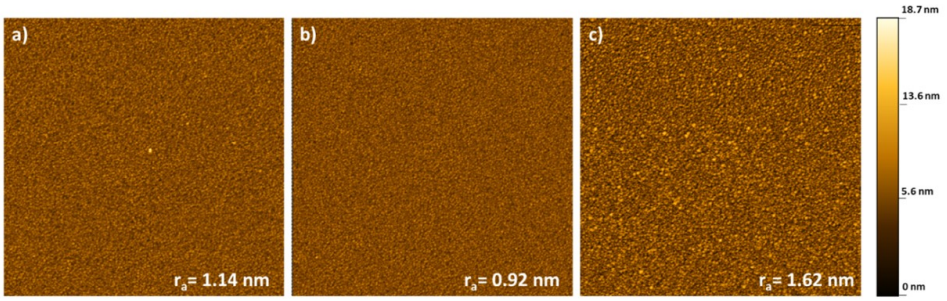

Figure S. A.2: Atomic Force microscope images of ICPCVD a-SiC deposited at a) 75°C, b) 150°C and c) 400°C

A.2. Device fabrication and inspection

The development of the electron beam resist was performed in a three-step process immersing the samples in pentyl-acetate, MBIK:IPA (1:1) and IPA for 1 min each. For etching, the plasma power was set to 20W with 13.5 sccm of SF6 and 3.5 sccm of O_2 at a chamber pressure of 8 μBar. After etching the excess e-beam resist was removed by oxygen plasma cleaning (200 sccm O_2 at 50W) for 8 minutes.

To determine the specific dimensions of the waveguides under study, electron microscope images were taken top view and cross-section as shown in fig.S3.

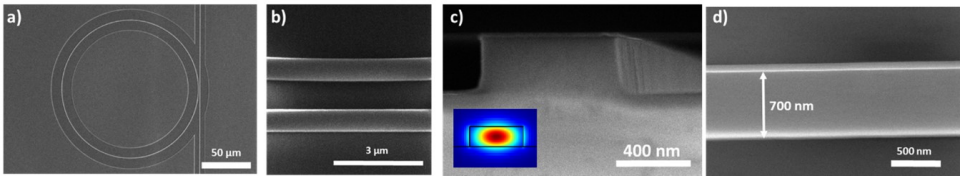

Figure S. A.3: Scanning Electron Microscope images of a) a ring resonator with 100 μm radius and gap 900 nm, b) gap region between the ring resonator and the bus waveguide, c) side image of the waveguide profile and d) top image of the bus waveguide for a design of 800 nm width.

A.3. Device fabrication and inspection

The most important parameter in an optical ring resonator is the loaded quality factor (Q_L), and is obtained experimentally from the transmission spectra of a resonance dip (or peak). This value quantifies the filtering quality of the device, and it is defined as [1]:

$$Q_L = \frac{\lambda}{\Delta\lambda} \tag{A.1}$$

where λ is the center wavelength at the resonance and $\Delta\lambda$ is the Full Width at half maximum of the Lorentzian fit. However, since this value is affected by the interaction with the coupling waveguide, the following expression for an intrinsic quality factor is often preferred:

A

$$Q_i = \frac{2Q_L}{1+\sqrt{T}} \tag{A.2}$$

In this equation, T denotes the transmission at the resonance.

From the intrinsic quality factor (Q_i), the loss coefficient (α) can be estimated by attending to the following expressions [2]:

$$\alpha = \frac{2\pi n_g}{Q_i \lambda} \tag{A.3}$$

where the group index (n_g) can be determined using experimental data of the free spectral range (FSR) of the ring resonator with radius R under study:

$$n_g = \frac{\lambda^2}{2\pi R \cdot FSR} \tag{A.4}$$

Last, to convert to units of dB/cm, the relation below is applied to the loss coefficient (cm^{-1}), with L being the length of the waveguide:

$$\alpha(dB/cm) = \frac{1}{L} 10 log_{10}\left(\frac{P}{P_o}\right) = \frac{1}{L} 10 log_{10}\left(e^{-\alpha L}\right) = 4.3429 \cdot \alpha(cm^{-1}) \tag{A.5}$$

A.4. SYSTEMATIC MEASUREMENTS OF QUALITY FACTOR, FREE SPECTRAL RANGE AND GROUP INDEX

To systematically characterize the devices with PMMA cladding, we used a C-L band tunable laser (Santec TSL-550). The light is coupled into the device using grating couplers patterned in the films. A fiber polarization controller Thorlabs (FPC032) is used to select the polarization of the input light. To obtain the transmission spectrum of the optical ring resonators, the wavelength of the laser is swept from 1500-1600 nm with 1 pm resolution at a speed of 10 nm/sec. The output transmission of the device is collected on a photodetector (Newport 2011). The following data is taken for the best two samples in the several deposition runs of ICPCVD. For these systematic measurements, devices were fabricated including grating couplers and an automatic setup was used to obtain the spectra. For reference, PECVD is also shown to demonstrate and compare this technique. In the later, the temperature cannot be lower than 200°C since no functional devices will be achieved. All the results obtained for the best two recipes in ICPCVD and PECVD are shown in fig.S4. Devices patterned on PECVD films deposited at 400°C presented higher quality factors, thus confirming that the main loss mechanism in PECVD, hydrogen incorporation, is lower. In this case, the highest loaded quality factor for the ring resonator was 1.8×10^5 with intrinsic quality factor of 2.1×10^5. On the other hand, ICPCVD shows a great stability over a broader temperature range due to the minimal incorporation of hydrogen and generally, lower grain sizes. The device with the highest quality factor obtained during this optimization process is shown in fig.S5.

For the device shown in fig.S5 and using the equations introduced in the beginning, a waveguide propagation loss of 1.06 dB/cm is obtained. Nevertheless,

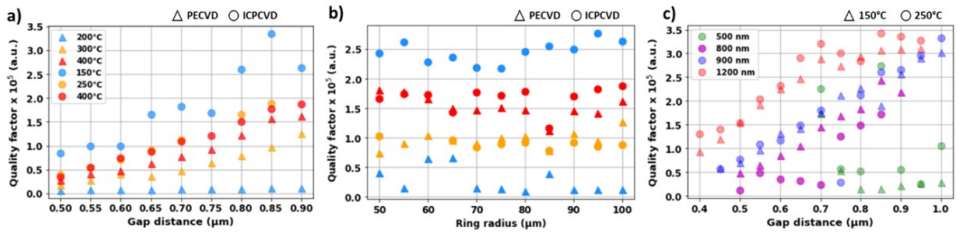

Figure S. A.4: Systematic data acquisition for the loaded quality factor of ring resonators in PECVD (400°C) and ICPCVD (150°C) as a function of a) gap distance and b) ring radius; c) gap distance for different waveguides widths and two different temperatures of ICPCVD.

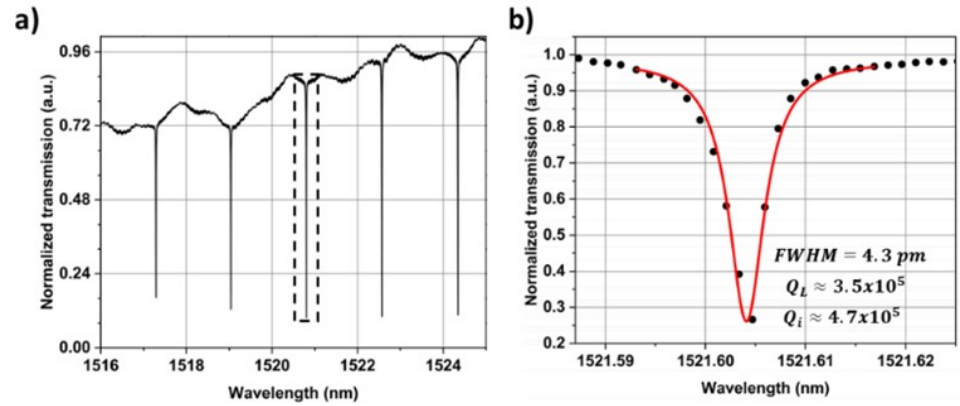

Figure S. A.5: a) Transmission spectrum from 1516 to 1525 nm of the ring resonator with highest quality factor with a free spectral range of 1.4 and b) 1 pm resolution scan of a resonance dip at 1521.65 nm.

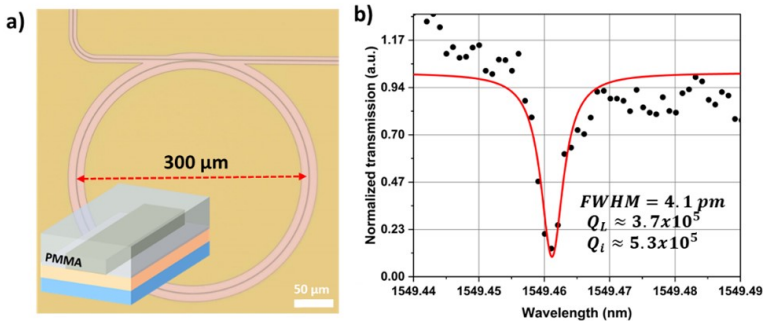

Figure S. A.6: a) Optical microscope image of a ring resonator with 300 μm diameter fabricated on a-SiC films deposited at 150°C with PMMA cladding and b) normalized transmission spectra with 1 pm resolution of a resonance dip around 1549.46 nm.

the lowest propagation losses were obtained for the device with 150 μm radius and PMMA cladding shown in fig. S6 with 0.78 dB/cm.

The free spectral range of the devices was taken from a set of dips around 1550 nm and the measurement number indicates each of the dip to dip distances. The group index was obtained using eq.S4 for each wavelength and ring radius and the data is represented in fig.S7.

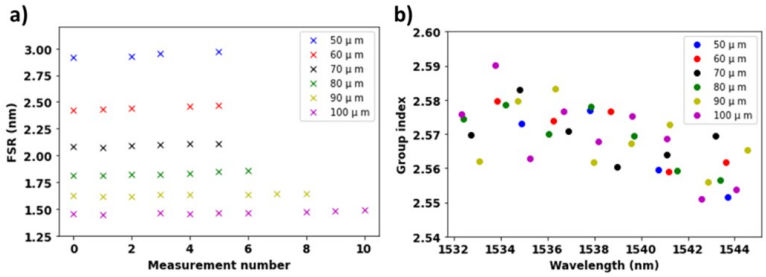

Figure S. A.7: For devices made on ICPCVD a-SiC deposited at 150°C with different radii, from 50 μm (blue) to 100 μm (purple), a) Free spectral range of several peaks around 1550 nm and b) group index as a function of the wavelength obtained from the FSR data for different radius.

A.5. THERMO-OPTIC COEFFICIENT OF A-SiC DEVICES

To determine the thermo-optic coefficient (TOC) of the optical ring resonators, the refractive index (n) and the thickness of the film (t) was obtained from ellipsometry data (shown in fig.S8) and confirmed via electron microscope images of the devices under study. Finite-Domain Time-Domain (FDTD) simulations using the commercial software Lumerical were performed to obtain the effective refractive index (n_{eff}) and the overlapping factor (Γ).

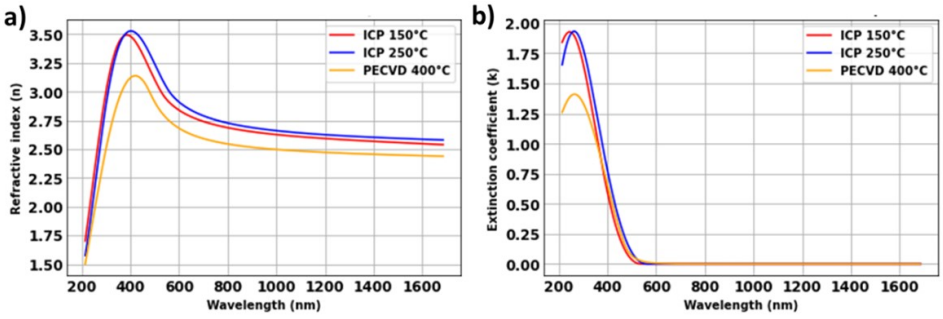

Figure S. A.8: Ellipsometry data for ICPCVD films deposited at 150°C and 250°C and PECVD deposited at 400°C showing a) refractive index and b) extinction coefficient

The samples were placed on top of a PCB using thermally conductive silver paste (fig.S9a). The PCB has a resistive thermal element and the temperature can be varied with a voltage supply up to 100°C (fig.S9b). The temperature is recorded

using a temperature sensor close to the sample surface. Optical access to the devices is performed with the same polarization maintaining fiber v-groove assemblies used for the initial characterization. In table S1 are shown the main parameters used for the calculation of the TOC together with the loaded and intrinsic quality factors for the best performing recipes.

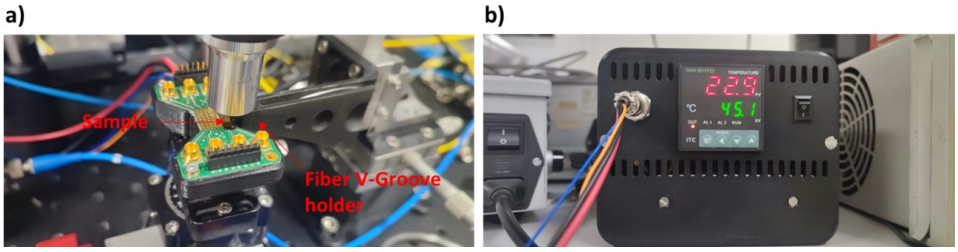

Figure S. A.9: a) PCB with heating element and b) temperature controller for side coupling configuration.

Sample	t (nm)	n_{eff}	Shift (pm/°C)	TOC (10^{-5}/°C)	Q_L (x10^5)	Q_{int} (10^5)
ICP 150°C	280	1.91	36.2	7.3	4.2	5.7
ICP 250°C	270	1.92	36.6	7.4	1.9	2.4
PECVD 400°C	265	1.79	28.8	5.1	1.8	2.1

Table A.1: Physical and optical parameters of fabricated devices.

A.6. Lift-off of a-SiC devices

The sample is prepared by exposing a 1 μm layer of PMMA with the desired shape to transfer. The shape used in this study is a squared island, yet the feasibility of this method is not limited to the geometry to transfer, enabling for small footprint and high flexibility for the implementation. Afterwards, deposition of a-SiC at 150°C is performed, and the pattern is revealed by doing lift-off with acetone at 53°C, followed by a patterning step for the optical devices that can be seen in fig.S10a and are tested with a side coupling configuration.

A close look of the interface between the deposited a-SiC and the thermal SiO_2 in fig.S10c shows that the temperature at which the films are deposited does not affect the quality of the lift-off. Devices fabricated on films deposited without the lift-off technique showed similar performance and the degradation can be attributed to the deposition tool as shown in fig.S10b.

A.7. Taper design for a-SiC-SiN integration

To determine the losses between the two platforms we performed Lumerical simulations considering the overlapping integral of the power in the two waveguides (fig.S11a for a-SiC profile and fig.S11b for 40 nm SiN). For the confinement of the final mode in the a-SiC, several bending radii were chosen and the power loss after

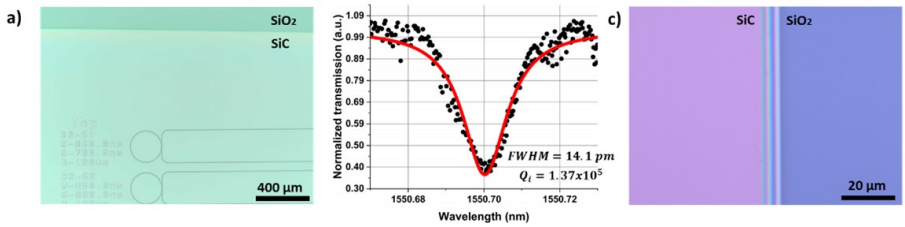

Figure S. A.10: a) Optical microscope image of lift-off a-SiC deposited at 150°C with ring resonator devices, b) 1 pm resolution transmission spectra of one of the devices and c) edge of the region between a-SiC and the substrate.

the bend was evaluated and shown fig.S12a with the configuration in fig.S12b. The monitor size to compute this power transfer was set to 1.2x1μm^2.

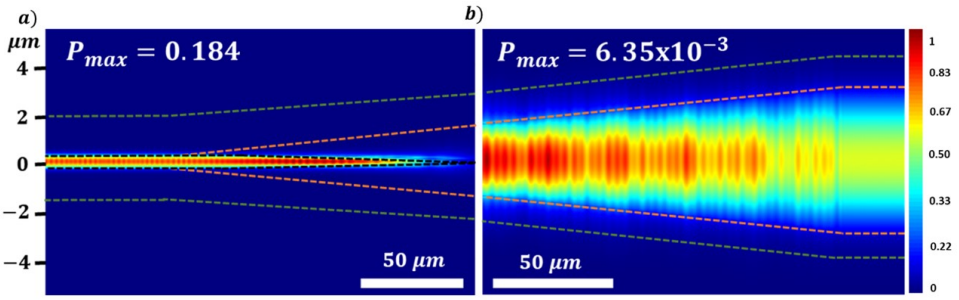

Figure S. A.11: Power distribution obtained by FDTD Simulations of the top taper region of a) a-SiC (dotted black line) and b) SiN (dotted orange line): both embedded in a tapered SiO2 cladding (dotted green line).

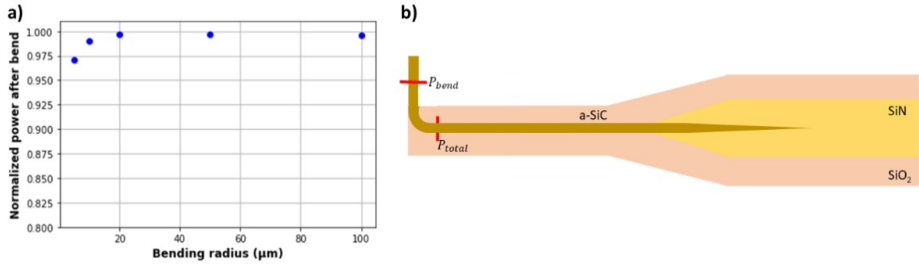

Figure S. A.12: a) Normalized power transfer as a function of bending radius and b) taper and monitor position for the determination of the bending losses.

A.8. Fabrication route for integration of a-SiC and lithium niobate

To protect the lithium niobate layer to the etching chemistry of a-SiC, a thin layer of silicon dioxide (50 nm) is deposited via PECVD or ICPCVD. In case the roughness of this layer affects the optical performance of the a-SiC devices, a planarization step using ion beam etching can be followed. Deposition of a-SiC films at low temperature is performed with a thickness of 280 nm. Depending on the configuration needed for modulation, a second etching step can be performed using Ar milling to define a waveguide in the LN or to etch a bias for the Au contact pads, which could enhance the modulation. After etching the LN waveguide, RCA-1 cleaning step is used to remove organic contaminants and reduce the sidewall roughness of the optical devices, enhancing the optical performance. For the FDTD simulations, the refractive index of a-SiC was chosen to be n=2.589 according to experimental data obtained via ellipsometry while for x-cut Lithium Niobate, it was chosen as nx=2.21, ny=2.21 and nz=2.13 (according to the coordinates in fig.S13b).

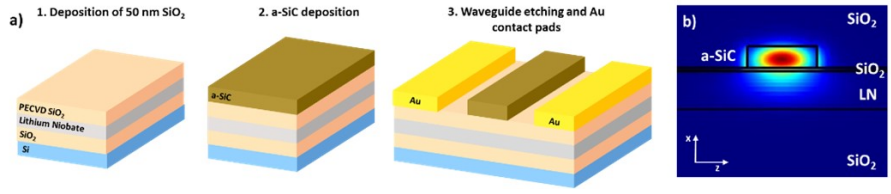

Figure S. A.13: a) Fabrication flow of a-SiC on LN for electro-optic modulation and b) mode profile obtained via FDTD 3D simulations of a-SiC/LN. The isolation layer between a-SiC and LN allows for the etching of the a-SiC waveguides without affecting the performance of the LN.

Material	Refractive index (n)	W/T (nm)	Q_{int} (x10^5) / dB/cm	Temp. (C)	n_2 (cm^2/W)	Ref
PECVD SiN	1.9	1500/730	7.24 / 0.42	350	-	[3]
LPCVD SiN	2.07	1300/655	8 / 0.4	700-850/1100*	$5{\cdot}10^{-15}$	[4]
Sputtered AlN	2.02	3500/1100	37 / 0.1	300	-	[5]
3C-SiCOI	2.6	1700/500	1.42 / 2.9	-	-	[6]
4H-SiCOI	2.6	3000/530	11 / 0.38	-	$6.9{\cdot}10^{-15}$	[7]
4H-SiCOI	2.6	1850/500-600	56 / -	-	$6.9{\cdot}10^{-15}$	[8]
PECVD a-SiC	2.45	800/350	1.6 / 3	300	$4.8{\cdot}10^{-15}$	[9]
ICPCVD a-SiC	2.59	750/280	4.7-5.7 / 0.78-1.07	150	-	This work

Table A.2: Physical and optical parameters of fabricated devices, being W and T the width and thickness of the waveguides in the optical devices, and n_2 the Kerr coefficient. *Annealing temperature

A

REFERENCES

[1] P. E. Barclay, K. Srinivasan, and O. Painter, *Nonlinear response of silicon photonic crystal microresonators excited via an integrated waveguide and fiber taper,* Optics express **13**, 801 (2005).

[2] P. Rabiei, W. H. Steier, C. Zhang, and L. R. Dalton, *Polymer micro-ring filters and modulators,* Journal of lightwave technology **20**, 1968 (2002).

[3] X. Ji, Y. Okawachi, A. Gil-Molina, M. Corato-Zanarella, S. Roberts, A. L. Gaeta, and M. Lipson, *Ultra-low-loss silicon nitride photonics based on deposited films compatible with foundries,* Laser & Photonics Reviews **17**, 2200544 (2023).

[4] Z. Ye, A. Fülöp, Ó. B. Helgason, P. A. Andrekson, and V. Torres-Company, *Low-loss high-q silicon-rich silicon nitride microresonators for kerr nonlinear optics,* Optics letters **44**, 3326 (2019).

[5] K. Liu, S. Yao, Y. Ding, Z. Wang, Y. Guo, J. Yan, J. Wang, C. Yang, and C. Bao, *Fundamental linewidth of an aln microcavity raman laser,* Optics Letters **47**, 4295 (2022).

[6] T. Fan, H. Moradinejad, X. Wu, A. A. Eftekhar, and A. Adibi, *High-q integrated photonic microresonators on 3c-sic-on-insulator (sicoi) platform,* Optics express **26**, 25814 (2018).

[7] M. A. Guidry, K. Y. Yang, D. M. Lukin, A. Markosyan, J. Yang, M. M. Fejer, and J. Vučković, *Optical parametric oscillation in silicon carbide nanophotonics,* Optica **7**, 1139 (2020).

[8] M. A. Guidry, D. M. Lukin, K. Y. Yang, R. Trivedi, and J. Vučković, *Quantum optics of soliton microcombs,* Nature Photonics **16**, 52 (2022).

[9] P. Xing, D. Ma, K. J. Ooi, J. W. Choi, A. M. Agarwal, and D. Tan, *Cmos-compatible pecvd silicon carbide platform for linear and nonlinear optics,* ACS Photonics **6**, 1162 (2019).

B

Supplementary information: Magic silicon dioxide for widely tunable integrated photonic circuits

B

Table of contents

B1. FILM CHARACTERIZATION

We performed stress measurements, atomic force microscopy and ellipsometry of the deposited silicon dioxide films and the results are found in this section. Overall, these measurements are an indication of the different properties that could be affecting the thermal expansion and conduction of the films. Stress measurements indicate overall stress in the film and not local stress on specific devices, which might be higher around the waveguide region due to anisotropy differences. AFM measurements reveal the grain sizes, surface roughness and deposition topography (skew) of the silicon dioxide claddings. As discussed in the main manuscript and supported by literature studies, these parameters affect the thermal expansion and conduction properties of a material. Ellipsometry data provides refractive index and an estimation of the density of the films, showing similar optical properties among all deposited films independent of deposition temperature or chamber pressure.

B1.1. Film stress

We measured the stress of amorphous silicon carbide and silicon dioxide films using FLX-2320-S Thin Film Stress Measurement system from Toho Technology. Silicon carbide films were deposited on top of thermally oxidized silicon wafers (525 μm) with oxide thickness of 8 μm. To characterize the silicon dioxide films they were deposited on bare silicon wafers. The data is summarized in table S1.

Table S. B.1: Stress data for a-SiC and SiO2 deposited using PECVD and ICPCVD techniques.

Technique and condition	Stress (MPa)
a-SiC PECVD 300°C	-50
a-SiC ICP 150°C	-300 to -500
SiO_2 ICP 30°C	10
SiO_2 ICP 150°C	10.4
SiO_2 ICP 300°C	-22.9
SiO_2 PECVD 300°C	-20

B1.2. Atomic Force Microscopy

We performed AFM scans of the deposited silicon dioxide films via PECVD and ICPCVD at different temperatures and retrieved surface morphology data, mainly surface roughness and skewness. The latter measures whether the surface has more deep valleys (negative skew) or protruding narrow peaks (positive). Three examples of AFM scans taken at different temperatures and techniques can be seen in fig.S1 and results can be found in table S2 with varying temperatures.

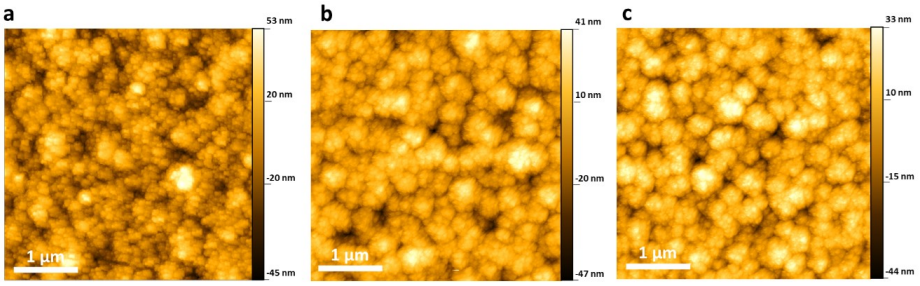

Figure S. B.1: Atomic Force Microscope scans of silicon oxide deposited a) with PECVD at 300°C, b) with ICPCVD at 30°C and c) with ICPCVD at 150°C.

B1.3. Ellipsometry

To characterize the refractive index of the silicon dioxide films deposited via ICPCVD and PECVD, we used Woollam M-2000 spectroscopic ellipsometer and fitted the corresponding data with a Cauchy model for both PECVD and ICPCVD at different deposition temperatures (Fig.S2a). For ICPCVD, we also performed ellipsometry for different chamber pressures (Fig.S2b). Table S2 summarizes the thickness, refractive index, surface roughness and skew obtained for the different films.

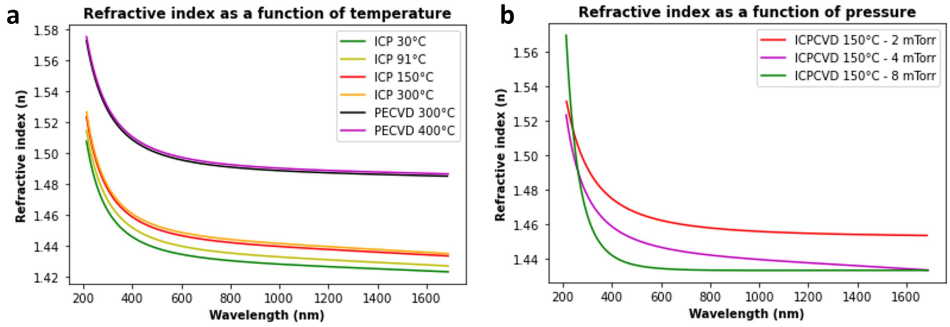

Figure S. B.2: Ellipsometry data for the refractive index as a function of wavelength for PECVD and ICPCVD Silicon Dioxide films deposited at different a) temperatures and b) chamber pressure.

Table S. B.2: Data for silicon dioxides deposited with ICPCVD and PECVD at different temperatures representing film thickness, refractive index, surface roughness and AFM skew. (—) refers to not measured.

Parameter / Technique	Thickness (nm)	Refractive index	Surface roughness (RMS nm)	Skew
ICP 30°C	2786.58	1.433	10.19 ± 1.34	-0.99
ICP 91°C	2746.93	1.443	---	---
ICP 150°C	2641.77	1.445	9.55 ± 1.28	-0.09
ICP 300°C	2607.79	1.447	11.49 ± 1.66	-0.12
PECVD 300°C	3101.33	1.494	12.11 ± 1.91	0.19
PECVD 400°C	3284.44	1.496	10.75 ± 1.49	0.01

B2. CHARACTERIZATION SETUP AND SUMMARIZED DATA

B2.1. CHARACTERIZATION SETUP

An schematic of the characterization setup described in the main manuscript is shown in fig. S3a with a picture of the optical setup in the lab shown in fig.S3b.

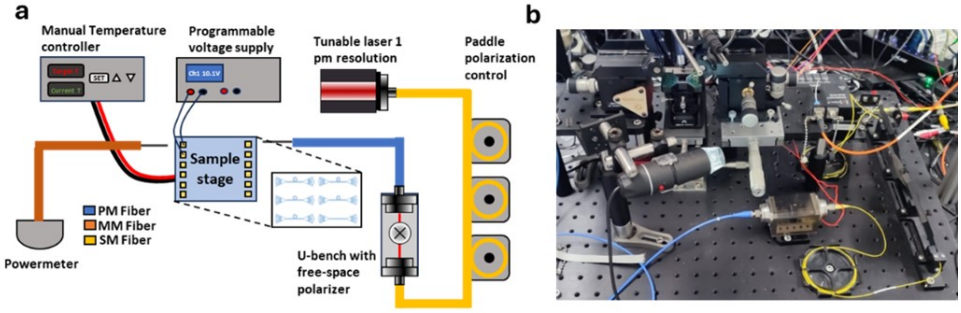

Figure S. B.3: a) Schematic of the optical setup used for the measurements and b) full optical setup in the lab.

B2.2. Optical properties of the fabricated devices

For the silicon dioxide claddings deposited at different temperatures via ICPCVD and PECVD on a-SiC, SiN and SOI, we summarize in table S3 the refractive index, free spectral range and corresponding group index of optical devices with dimensions stated in table S5.

Table S. B.3: Optical properties of the devices fabricated using different oxides with PECVD and ICPCVD at different temperatures. All the free spectral ranges are taken from the spectral measurement done at room temperature. *The corresponding group index is calculated assuming the FSR of the first mode. (—) refers to samples not fabricated.

	SiO_2 T (°C)	n oxide	a-SiC		SiN		SOI	
			FSR (nm)	n_g	FSR (nm)	n_g	FSR (nm)	n_g
PECVD	200	---	1.32	2.41	---	---	0.96	3.32
	300	1.49440	1.30	2.45	1.49-1.55	2.14*	0.96	3.32
	400	1.49605	1.22	2.61	---	---	---	
ICP	30	1.43336	1.34	2.38	1.83	1.74	0.87	3.66
	75	---	---	---	---	---	0.90	3.54
	150	1.44543	1.32	2.41	1.69-1.59	1.89*	0.86	3.71
	300	1.49605	1.30	2.45	1.80	1.68	0.86	3.71
	400	---	1.31	2.43	1.71-1.31	1.86*	0.87	3.66

For silicon dioxide claddings deposited via ICPCVD on a-SiC platform at a fixed deposition temperature of 150°C, we summarize in table S4 the free spectral range and group index of the fabricated devices.

Table S. B.4: Optical properties of the devices made with Silicon Dioxide deposited via ICPCVD at 150°C varying the chamber pressure.

Oxide pressure (mTorr)	1.5	2	2.5	4	6	8	10	12	16
FSR (nm)	1.33	1.32	1.34	1.35	1.36	1.32	1.43	1.34	1.40
n_g	2.40	2.41	2.38	2.36	2.34	2.41	2.23	2.38	2.28

To determine the effective thermo-optic coefficient, we simulated the mode profile with the selected dimensions using Ansys Lumerical MODE solutions for the different platforms. The table below summarizes information about width, thickness, ring radius, refractive index and obtained effective index. In table S6 we summarize the mode overlap factor for the different platforms using the simulation results in table S5.

Table S. B.5: For the studied ring resonators summary of material platform, waveguide dimensions, ring radius and effective index calculated using FDTD (Ansys Lumerical MODE solutions).

Material	Width / Thickness (nm)	Ring radius (µm)	n	n_{eff}
ICPCVD a-SiC 150°C	800 / 271	120	2.67	1.937
SOI	700 / 220	120	3.44	2.565
Silicon Nitride	1000 / 368	120	2	1.633

Table S. B.6: For the studied ring resonators mode fill factors calculated using FDTD (Ansys Lumerical MODE solutions).

Material	Overlap waveguide (%)	Overlap cladding (%)	Overlap substrate (%)
ICPCVD a-SiC 150°C	71.4856	13.7907	14.7237
SOI	79.4482	9.644	10.9078
Silicon Nitride	63.4867	20.6400	15.8733

Table S7 summarizes the wavelength shifts in pm/°C and the corresponding effective thermos-optic coefficient for the different claddings deposited on a-SiC, SiN and SOI.

Table S. B.7: For a-SiC, SiN and SOI optical ring resonators, thermal shift in pm/°C and effective thermo-optic coefficient for different oxide temperatures and techniques. (—) refers to samples not fabricated/non-functional devices. As a reference, PMMA on SiN has thermal tunability of -51 pm/°C.

SiO_2 T (°C)		a-SiC		SiN		SOI	
Technique		Shift (pm/°C)	TOC_{eff} (10^{-5})	Shift (pm/°C)	TOC_{eff}(10^{-5})	Shift (pm/°C)	TOC_{eff}(10^{-5})
PECVD	200	16.9 ± 0.4	2.12	---	---	17.10 ± 0.7	3.00
	300	32.4 ± 1.0	4.63	14.29 ± 0.4	1.41	38.0 ± 0.4	7.47
	400	31.4 ± 0.3	4.78	---	---	---	---
ICPCVD	30	---	---	-157.3 ± 22.1	-18.16	13.9 ± 2.2	2.62
	75	-165.9 ± 9.2	-25.96	---	---	-94.6 ± 9.6	-22.28
	150	-90.0 ± 8.1	-14.52	-86.4 ± 24.1	-11.03	---	---
	300	-96.7 ± 7.9	-15.80	-106.0 ± 7.9	-11.99	4.8 ± 0.7	0.48
	400	-68.1 ± 23.5	-11.19	-36.94 ± 5.8	-4.97	17.4 ± 0.8	3.45

For the ICPCVD silicon dioxide claddings deposited at a temperature of 150°C and varying the chamber pressure, we summarize in table S8 the wavelength shift in pm/°C and the corresponding effective thermos-optic coefficient.

Table S. B.8: For a-SiC optical ring resonators, thermal shift in pm/°C and effective thermo-optic coefficient with an ICPCVD oxide cladding deposited at 150°C at different chamber pressures.

Oxide pressure (mTorr)	1.5	2	2.5	4	6	8	10	12	16
Shift (pm/°C)	27.5	10.2	21.6	-52.1	-46.5	-62	-78.5	-84.5	-117.7
STD ± Δσ (pm/°C)	1.6	1.1	1.5	2.6	5.5	8	7	0.4	7.1
TOC_{eff} (10^{-5})	3.75	1.09	2.81	-8.44	-7.53	-10.02	-11.18	-13.47	-17.85

To determine the losses introduced by the different claddings deposited at different deposition temperatures and pressures on a-SiC optical devices, we summarized the main parameters of the analysed resonance dip together with the optical losses in dB/cm in table S9.

We also deposited one of the ICPCVD claddings at a temperature of 300°C with a chamber pressure of 12 mTorr on a-SiC, corresponding to the wavelength spectra reported in the main manuscript (fig.2c). The data to determine the losses can be found in table S10 has been taken from the spectra at room temperature (27°C).

Table S11 summarizes main parameters of the measured resonance for a-SiC devices depositing silicon dioxide claddings via ICPCVD at a deposition temperature of 150°C and varying chamber pressure from 2.5 mTorr to 16 mTorr.

Table S. B.9: Optical data for different ICPCVD Silicon Dioxide at a chamber pressure of 8 mTorr and different deposition temperatures of specific transmission dips.

Temperature (°C)	30	150	300
Full-Width at Half-Maximum (FWHM - pm)	14.50	11.88	13.77
Wavelength (nm)	1549.73	1548.50	1549.87
Transmission (au)	0.367	0.412	0.460
Loaded quality factor	107,000	130,000	113,000
Intrinsic quality factor	133,000	158,000	134,000
Group index	2.378	2.41	2.45
Loss (dB/cm)	3.15	2.68	3.22

Table S. B.10: Optical data for ICPCVD Silicon Dioxide deposited at a temperature of 300°C and chamber pressure of 12 mTorr of a specific transmission dip.

T (°C)	P (mTorr)	FWHM (pm)	Wavelength (nm)	T (au)	Q_{load}	Q_{int}	n_g	Loss (dB/cm)
300	12	22.45	1550.22	0.265	69,000	91,000	2.41	4.74

Table S. B.11: Optical data for ICPCVD Silicon Dioxide deposited at a temperature of 150°C and different chamber pressures of a specific transmission dip.

Pressure (mTorr)	2.5	8	10	16
Full-Width at Half-Maximum (FWHM)	13.07	11.88	18.80	30.27
Wavelength (nm)	1548.32	1548.50	1548.38	1550.4
Transmission (au)	0.329	0.412	0.363	0.250
Loaded quality factor	118,000	130,000	82,360	51,220
Intrinsic quality factor	150,000	158,000	103,000	68,000
Group index	2.38	2.41	2.23	2.28
Loss (dB/cm)	2.79	2.69	3.81	5.90

Fig. S4 shows a graphical representation of the change of free-spectral range, quality factor and refractive index for ICPCVD films deposited at different temperatures and pressures. Fig.S4c also shows the refractive index of silicon dioxide claddings deposited via PECVD at 300°C and 400°C.

B3. Passive devices

We demonstrate two different passive configurations of optical devices. Fig.S5a shows the resulting spectra two ring resonators connected in series with positive and negative claddings as the temperature of the sample stage is raise from 20°C to 35°C in steps of 2°C. Fig.S5b shows an optical microscope image of a Mach-Zehnder interferometer where one of the arms is covered with a cladding deposited via ICPCVD at a temperature of 150°C and chamber pressure of 8 mTorr. Raising the

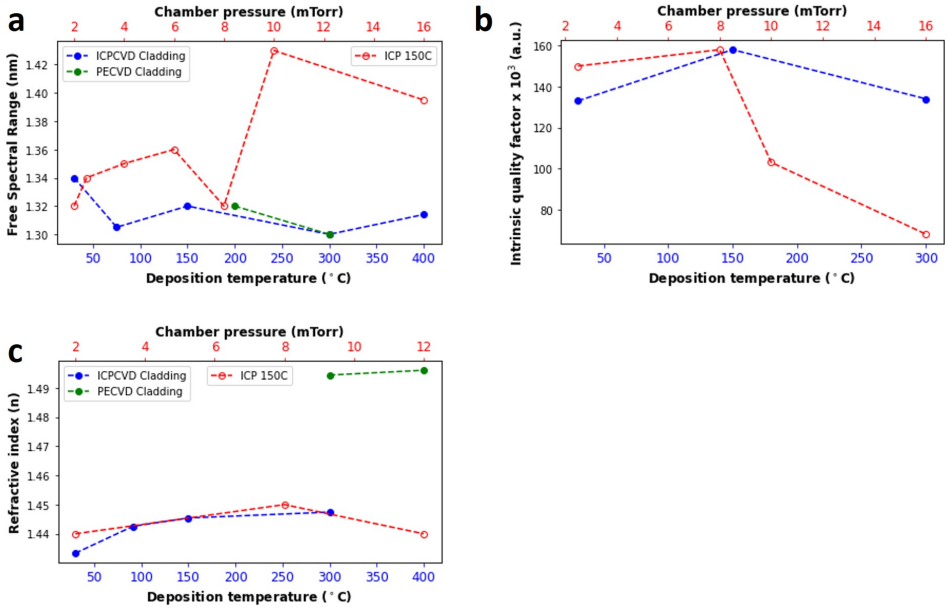

Figure S. B.4: For a-SiC devices, parameters as a function of deposition temperature and pressure of the Silicon Dioxide cladding. More precisely, a) Free spectral range, b) Intrinsic quality factor and c) refractive index of the deposited oxides.

stage temperature vary the relative phase between each arm and the intensities at different outputs.

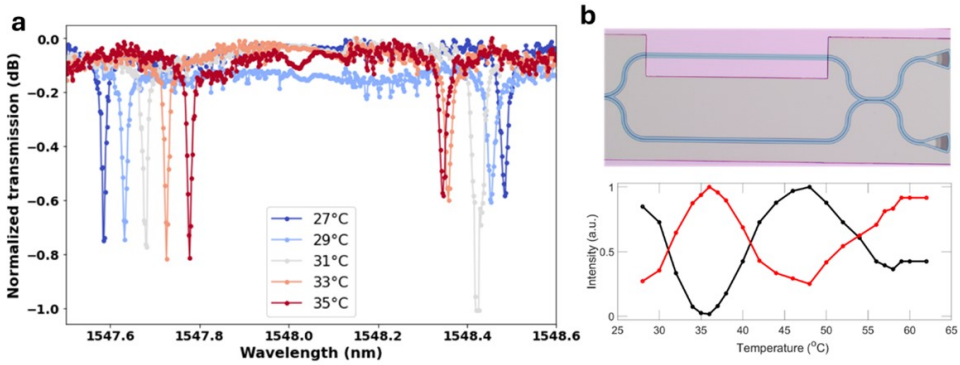

Figure S. B.5: a) Spectra of ring resonators at different temperatures fabricated on the same chip with shared bus waveguide and claddings presenting bidirectional thermal response and b) Optical microscope image of a Mach-Zehnder interferometer covered with ICPCVD SiO2 cladding in one of the arms and intensity as a function of temperature for the two output ports.

B4. Strain release

B4.1. Deposition of PECVD films

As an experiment to determine the effect in the thermal tunability when depositing other films with opposite thermal expansion, we deposited PECVD claddings on top of the ICPCVD cladded devices deposited at 150°C. The resonance wavelength position as a function of the stage temperature for the different configurations is depicted in fig.S6. It is observed that the dominant shift is similar to the one introduced by only using PECVD cladding and it cannot be attributed to annealing effects in the films as shown in section 4.3.

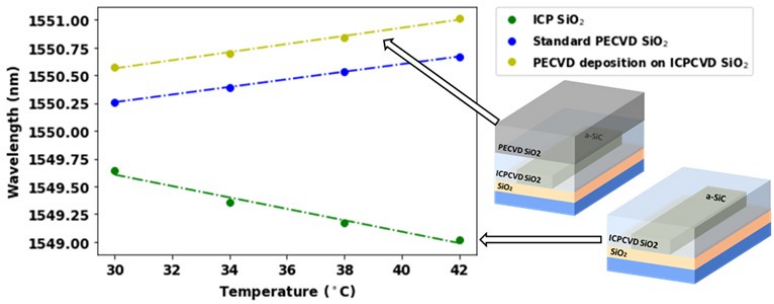

Figure S. B.6: Wavelength shift as a function of temperature for optical ring resonators covered with ICPCVD SiO2, Standard PECVD SiO2 and PECVD on top of ICPCVD oxide.

B4.2. Low temperature cladding

We deposited a silicon dioxide cladding via ICPCVD at 30°C on silicon nitride devices and the wavelength spectra as a function of the stage temperature between 27°C and 35°C is shown in fig.S7. When measuring the thermal response of the resonance, we observed that for stage temperatures higher than 33°C, there is a non-linear jump and the thermal tunability becomes lower. We attribute this effect to strain release between the core and the cladding that causes a decrease in the thermal tunability of the optical devices.

B4.3. Temperature stability

On films deposited via ICPCVD at a temperature of 150°C and chamber pressure of 8 mTorr, we also performed high temperature processing of the devices to investigate possible changes in the thermo-optic shift. The temperature range was done in incremental steps from 200°C to 400°C during 1h and the resulting position of the resonance dip as a function of stage temperature for the different processing temperatures is shown in fig.S8. We observed no difference in the thermal tunability.

B5. Representative spectra for the different platforms

Below we include representative data and spectra for the wavelength shift of devices on amorphous silicon carbide, silicon nitride and silicon-on-insulator using different deposition conditions, mainly chamber pressure and deposition temperature.

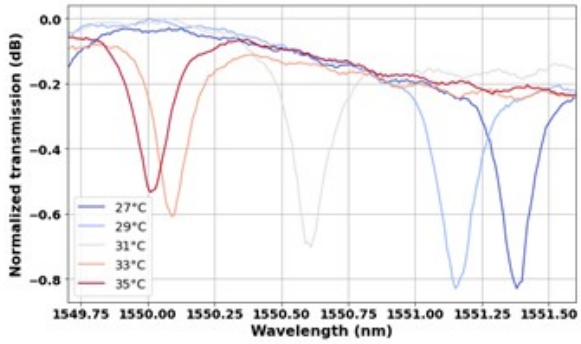

Figure S. B.7: Wavelength spectra around 1550 nm for ICPCVD 30°C Silicon Dioxide cladding on a SiN device as a function of temperature between 27°C and 35°C in steps of 2°C.

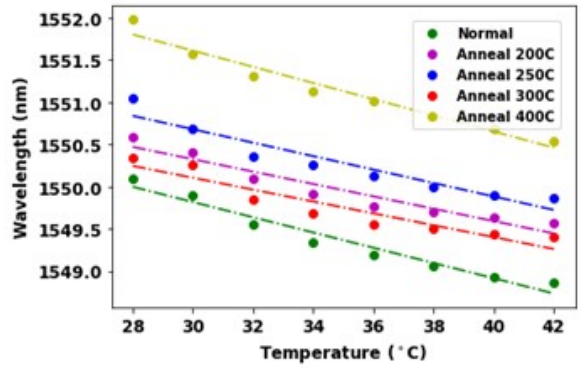

Figure S. B.8: Wavelength shift as a function of the stage temperature of the selected resonance dip for different temperatures, from the standard devices (green) to annealing at 400°C (yellow).

B5.1 AMORPHOUS SILICON CARBIDE

In fig.S9 we represent the wavelength shift as a function of stage temperature for ICPCVD silicon dioxide claddings deposited at 150°C and chamber pressures of 1.5 mTorr and 12 mTorr corresponding to negative and positive thermal tunability. Fig.S10 shows the resulting wavelength spectra taken at different stage temperatures and linear fitting to obtain the wavelength tunability for a-SiC devices with silicon dioxide ICPCVD claddings deposited at 30°C and chamber pressure of 8 mTorr. This device presents the largest shift in wavelength in a stage temperature range between 27°C and 30°C.

We also include in fig.S17 the wavelength spectra at different stage temperatures and corresponding resonance wavelength fitting of ICPCVD claddings deposited via ICPCVD at 150°C and varying the chamber pressure. The wavelength accuracy is limited by the step size of the wavelength sweeps (0.005 nm) and the accuracy of the laser (absolute wavelength accuracy of ±0.2 nm, tuning accuracy of ±0.02 nm and tuning repeatability of ±0.005 nm). Every time a scan is finished, the laser is set back

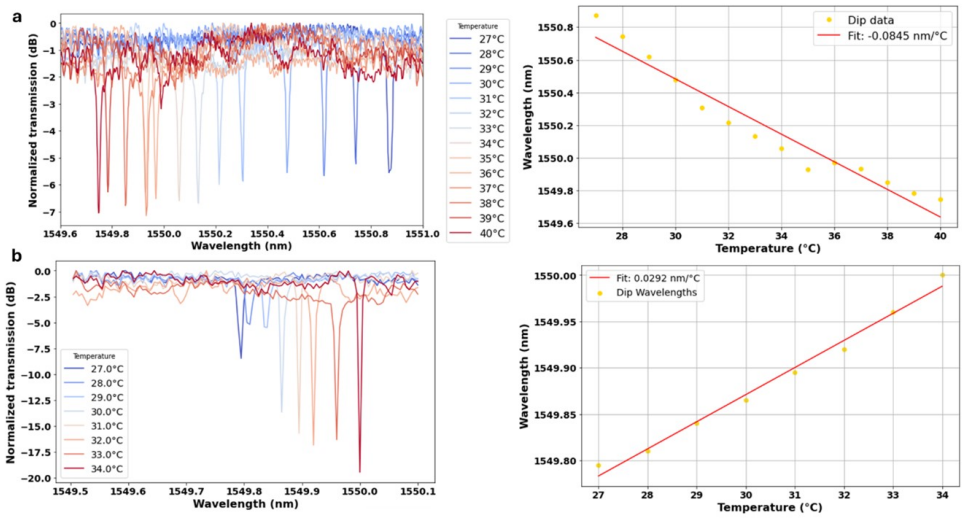

Figure S. B.9: Spectra taken at different temperatures for a-SiC ring resonators with SiO2 cladding deposited via ICPCVD at 150°C and corresponding fitting for chamber pressure of a) 12 mTorr and b) 1.5 mTorr.

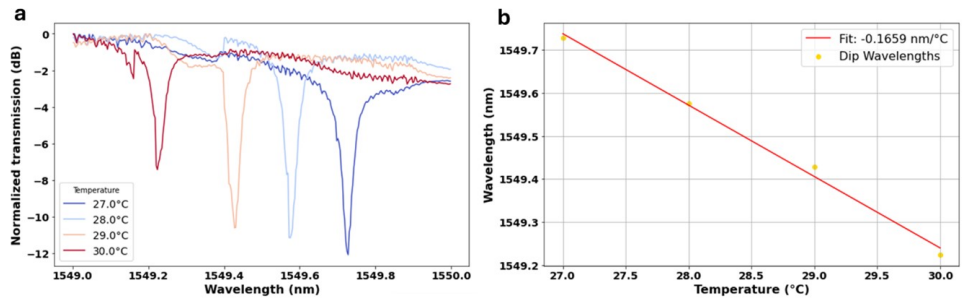

Figure S. B.10: a) Normalized spectra at different stage temperatures for an a-SiC optical device with ICPCVD SiO2 cladding deposited via ICPCVD at 75°C (ramp up to 91°C) and chamber pressure of 8 mTorr and b) resonance dip position with linear fitting.

to the initial wavelength and the limiting factor is the laser positioning accuracy. The measurements done with the optical spectrum analyser (for all the devices with SiN and SOI and a-SiC devices using PECVD cladding) show minimal standard deviation in the resonant dip position.

The device that presented the highest negative shift for the a-SiC platform was fabricated using ICPCVD SiO2 deposited at a temperature of 300°C and chamber pressure of 12 mTorr. The fitting of the resonance dip as a function of temperature is represented in fig.S12 and corresponds to the data shown in fig.2b in the main manuscript.

Attending to the systematic measurements done for ICPCVD claddings deposited

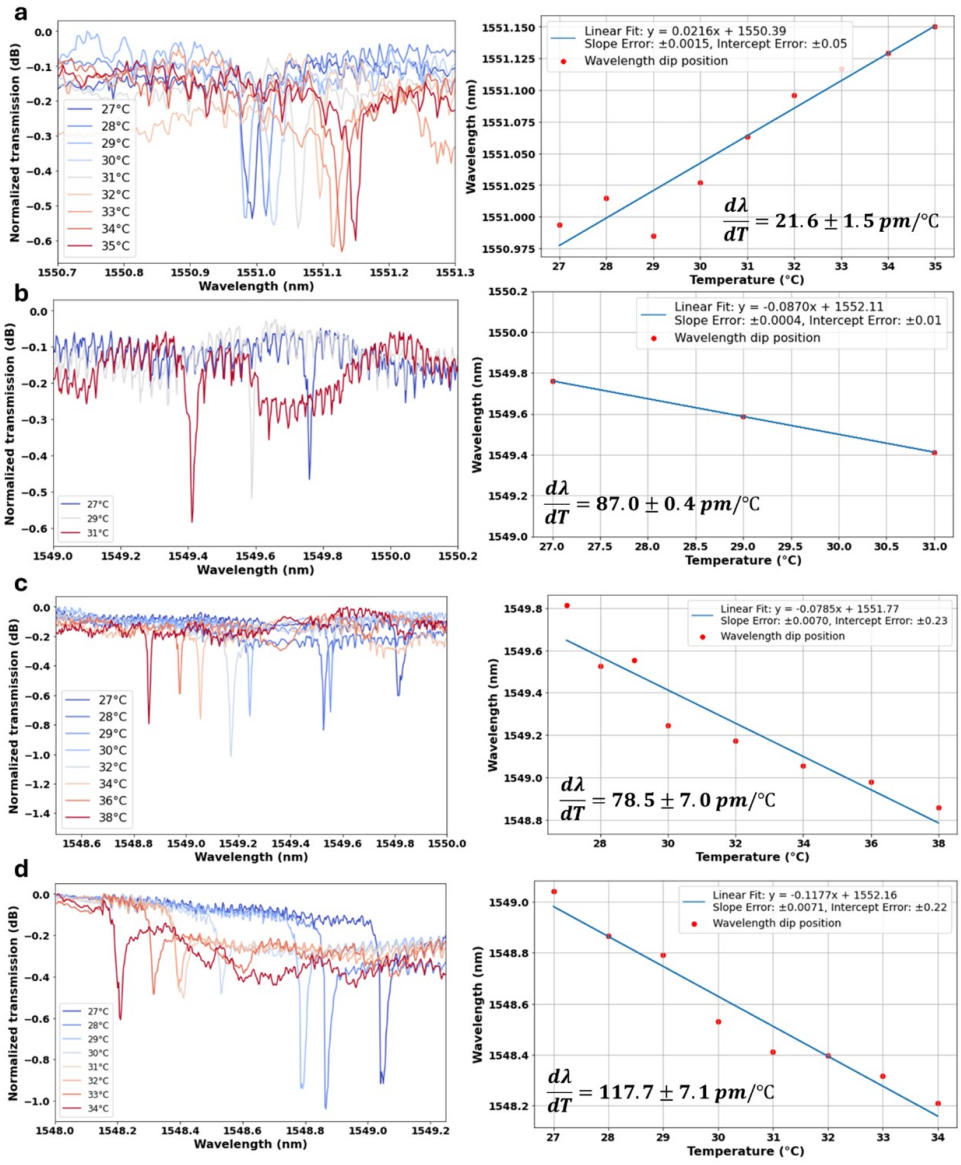

Figure S. B.11: Spectra taken at different temperatures for a-SiC ring resonators with SiO2 cladding deposited via ICPCVD at 150°C and corresponding fitting for chamber pressure of a) 2.5 mTorr, b) 8 mTorr, c) 10 mTorr and d) 16 mTorr.

at a temperature of 150°C and varying the chamber pressure on a-SiC optical devices, the athermal condition can be achieved for a chamber pressure of 3 mTorr. We deposited a silicon dioxide cladding on a-SiC with these conditions and measured

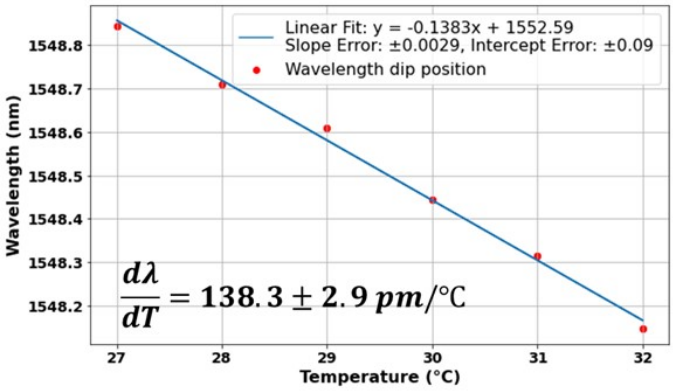

Figure S. B.12: For silicon dioxide deposited using ICPCVD at a temperature of 300°C and chamber pressure of 12 mTorr, wavelength position of the selected resonance dip position as a function of temperature together with the linear fitting.

the ring resonator in a temperature range between 27°C and 41°C in steps of 1°C. The resulting spectra is shown in fig.13a with the corresponding wavelength position as a function of the stage temperature in fig.13b. The thermal tunability between 27°C and 35°C obtained from fitting the data is 1.1 pm/°C . In the main article, the same data is represented in steps of 2°C resulting in a thermal tunability of 1.5 pm/°C.

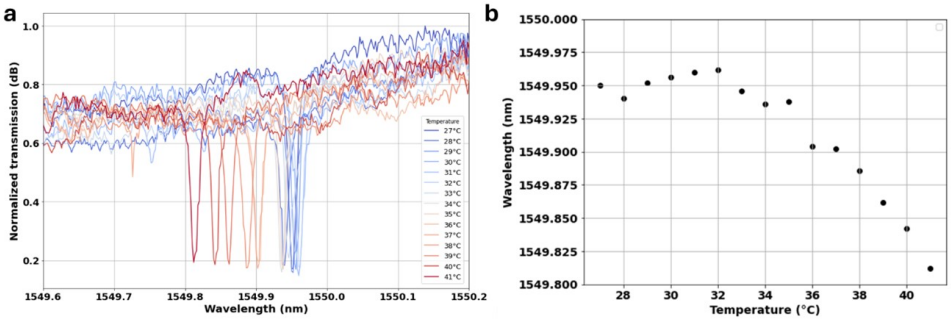

Figure S. B.13: For an a-SiC ring resonator with ICPCVD SiO2 cladding deposited at 150°C and chamber pressure of 3 mTorr shown in figure 2 of the manuscript a) Normalized spectra taken at different temperatures with steps of 1°C and b) dip position as a function of temperature.

B5.2. Silicon Nitride devices

We deposited silicon dioxide claddings on silicon nitride devices via ICPCVD and PECVD at different temperatures and the resulting wavelength spectra as a function of stage temperature is found in fig.S14. As a reference, we also included the effect of a common electron beam resist PMMA on the thermal shift, known to give negative thermo-optic tunability.

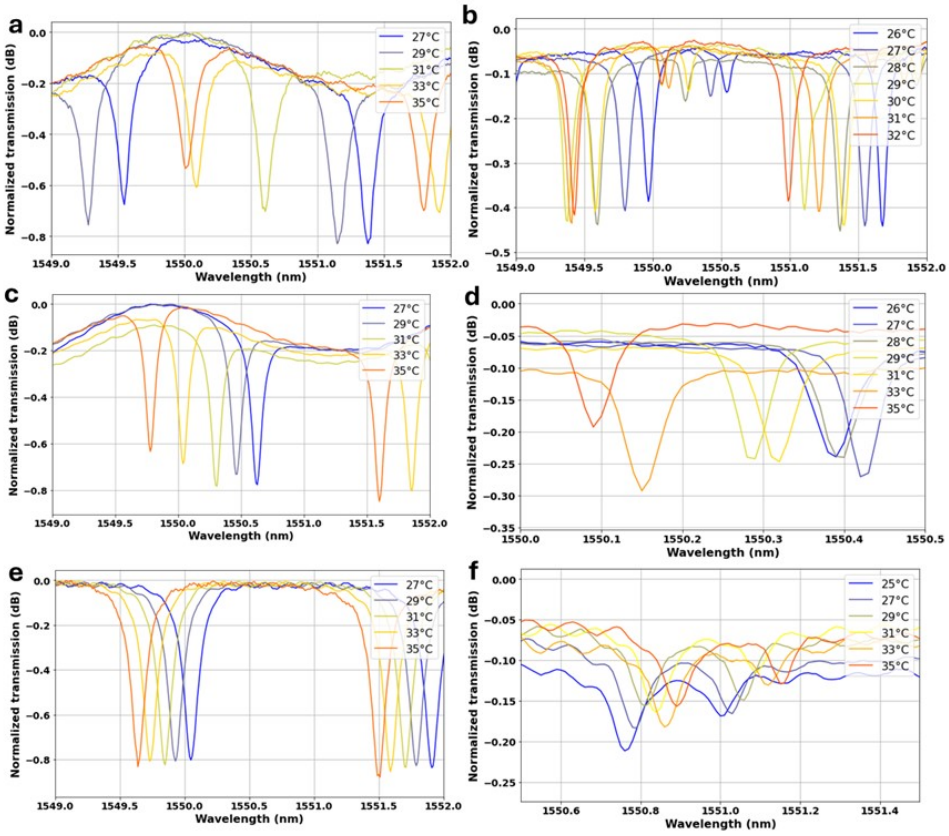

Figure S. B.14: Wavelength shift as a function of temperature for SiN device using ICPCVD SiO2 deposited at a) 30°C, b) 150°C, c) 300°C, d) 400°C, e) PMMA (-51 pm/°C) and f) PECVD SiO2 deposited at 300°C.

B5.3. SILICON-ON-INSULATOR DEVICES

We deposited SOI optical devices using PECVD at temperatures of 200°C and 300°C and ICPCVD at a temperature of 75°C (fig.S15) and the wavelength spectra as a function of temperature is shown in fig.S15. We also deposited silicon dioxide via ICPCVD at 300°C and chamber pressure of 8 mTorr resulting in a thermal tunability of 5.5 pm/°C. The wavelength spectra as a function of the temperature and the corresponding fitting for the two resonances separated one free spectral range is shown in fig.S16.

B6. COUPLED-RESONATOR OPTICAL WAVEGUIDE (CROW) DEVICES

We fabricated one sample with two CROW devices using positive and negative claddings and metal micro-heaters. We measured this devices by sweeping the voltage and recorded the spectra.

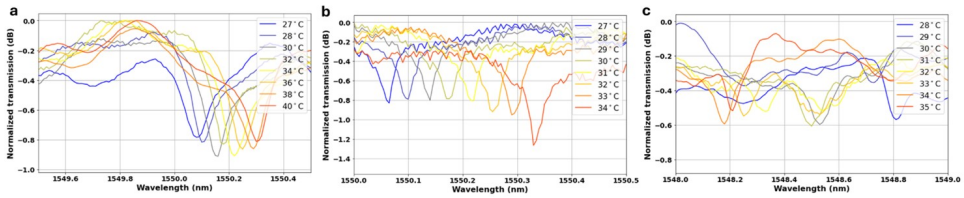

Figure S. B.15: Wavelength shift as a function of temperature for an SOI device with SiO2 claddings deposited using a) PECVD at 200°C, b) PECVD at 300°C and c) ICPCVD at 75°C.

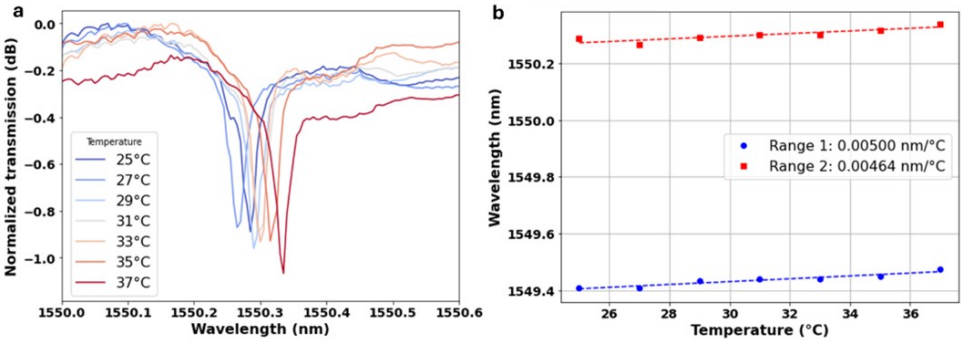

Figure S. B.16: a) Transmission spectra for a Silicon-On-Insulator device with SiO2 cladding deposited via ICPCVD at 300°C and chamber pressure of 8 mTorr and b) corresponding fitting of the two dips separated by a free spectral range.

CROW DEVICE 1

In the same configuration as the device shown in the main manuscript, we measured another device connected in parallel as depicted in fig.S17a in a voltage range of 0V to 12V in steps of 0.5V. Fig.S17b shows that the resonance condition can be achieved at a voltage of 9.5V. Fig.S17c shows wavelength spectra taken at different voltages of 0V, 7.5V and 9.5V (resonance condition).

CROW DEVICE 2

For the same device as the one shown in the manuscript (fig.3b-c) and in the same configuration (heaters connected in parallel), we did a coarse scan of the voltage in steps of 1 V from 0 to 13 V. A 2D mapping of the transmitted intensity as a function of the wavelength is shown in fig.S18 together with the specific spectra taken at different voltages of 0V, 3V and 6V.

B7. THERMAL CROSSTALK

In this section we show the corresponding spectra taken at different voltages (from 0V to 10V) to characterize the thermal crosstalk between devices using continuous PECVD (fig.S20) and ICPCVD (fig.S21) claddings as well as cladding deposited using lift-off for thermal isolation (fig.S22). Ring A depicts the device where the heater is applied while Ring B is the device that shifts due to thermal crosstalk. We also show

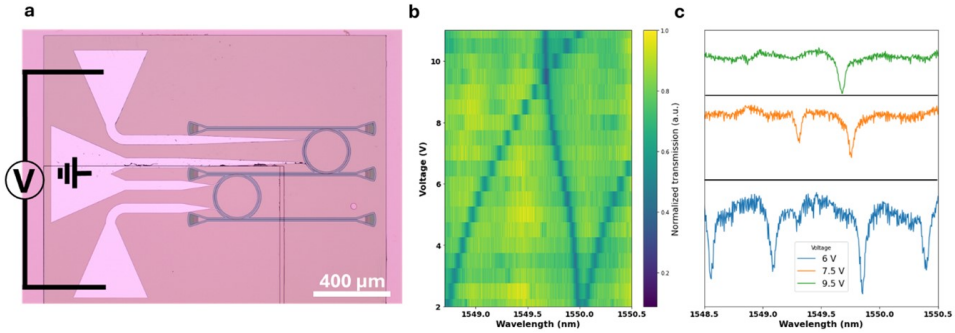

Figure S. B.17: a) Optical microscope image of device 1 with two ring resonators connected with a middle waveguide to track the resonance dips in parallel connection configuration. b) Wavelength intensity spectra as a function of voltage applied and c) Wavelength spectra for 6V (blue), 7.5V (orange) and 9.5V (green). The spectra are separate between each other.

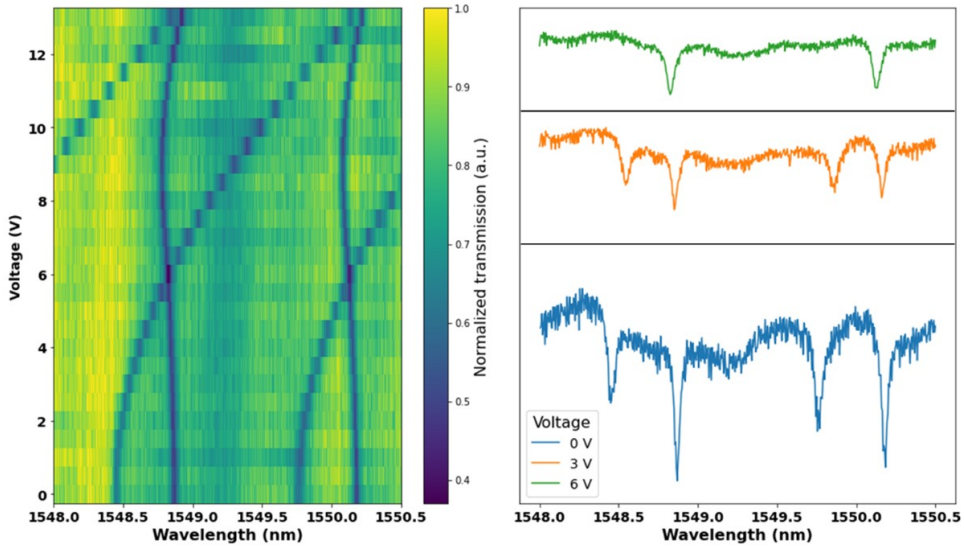

Figure S. B.18: Transmission intensity as function of the wavelength spectra for different applied voltages for the device in fig.3b-c of the main manuscript and wavelength spectra for voltages 0V, 3V and 6V taken from the 2D map. The spectra are separate between each other.

an SEM image of the region between optical devices after performing ICPCVD lift-off of the cladding (fig.S23).

We performed scanning electron microscopy (SEM) of the cladding fabricated using lift-off and the resulting image is shown in fig.S23. Depositing a cladding delimited by resist produces roughness in the region where the lift-off is performed. The main reason is that the silicon dioxide is also deposited with lower quality without continuity on the resist. When the lift-off is performed, material in the

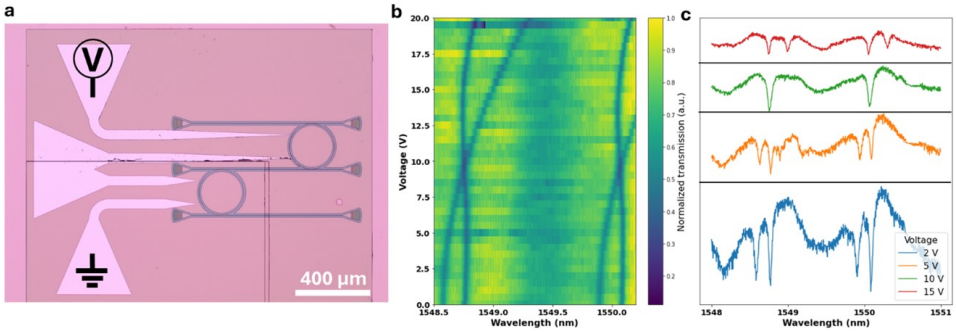

Figure S. B.19: a) Optical microscope image of device 2 (shown in the main article fig.3b-c) connected in series with two ring resonators with a middle waveguide to track the resonance dips. b) Wavelength intensity spectra as a function of the volage applied and c) Wavelength spectra for 2V (blue), 5V (orange), 10V (green) and 15V (red). The spectra are separate between each other.

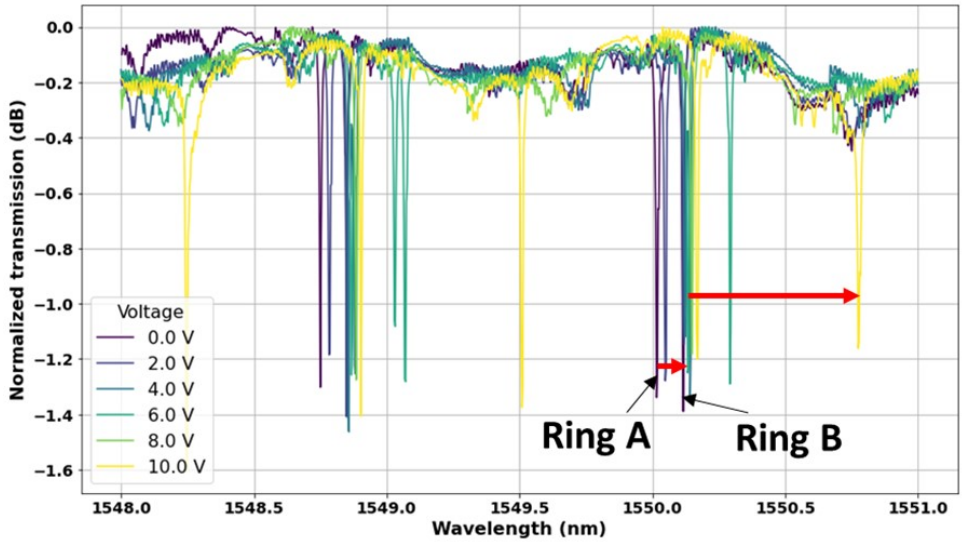

Figure S. B.20: Spectra at different voltages for the two ring resonators fabricated using continuous PECVD cladding

cladding that is also attached to the resist is also removed. It is important to notice that this does not affect the optical quality of the mode since the cladding is wide enough (cladding width of 9 μm). In the picture below is also pointed the top micro-heater width (yellow), the remaining amorphous silicon carbide film (orange), the limit of the silicon dioxide cladding (blue) and the bottom thermal silicon dioxide (red).

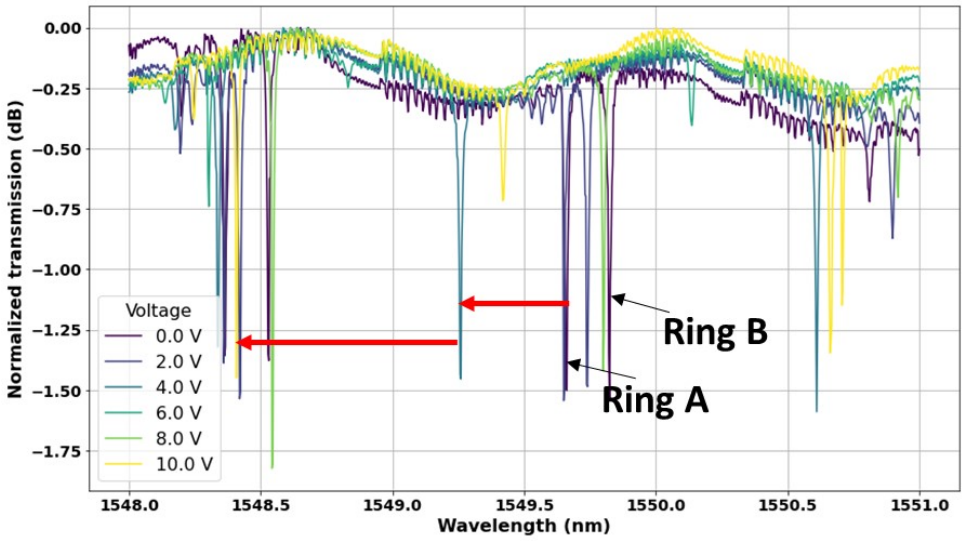

Figure S. B.21: Spectra at different voltages for the two ring resonators fabricated using continuous ICPCVD cladding.

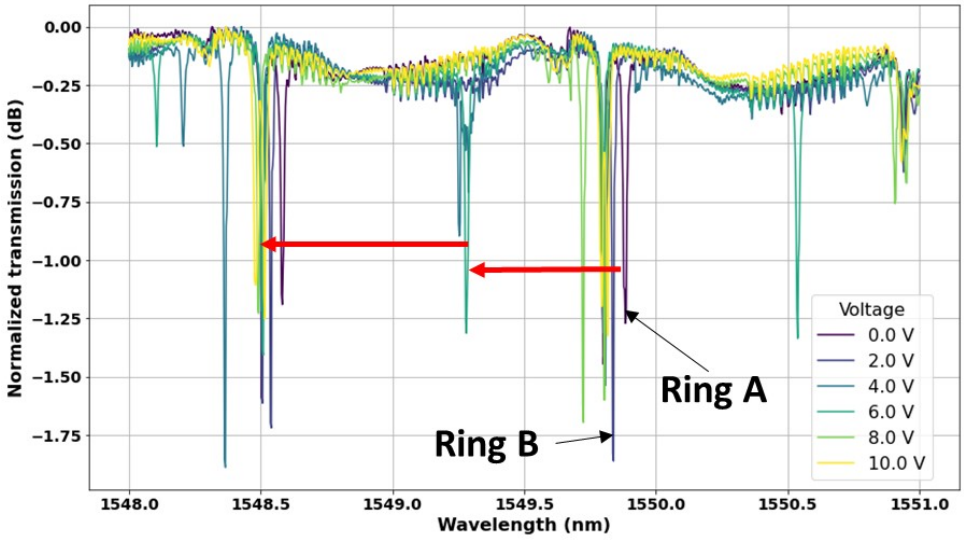

Figure S. B.22: Spectra at different voltages for the two ring resonators fabricated using the lift-off approach.

B8. RAMP-UP AND RAMP-DOWN MEASUREMENTS

To address the repeatability of the measurements using the different claddings, we performed forward and backward voltage sweeps on devices with ICPCVD and PECVD silicon dioxide. The voltage was varied between 0V and 6V. Fig.S24a

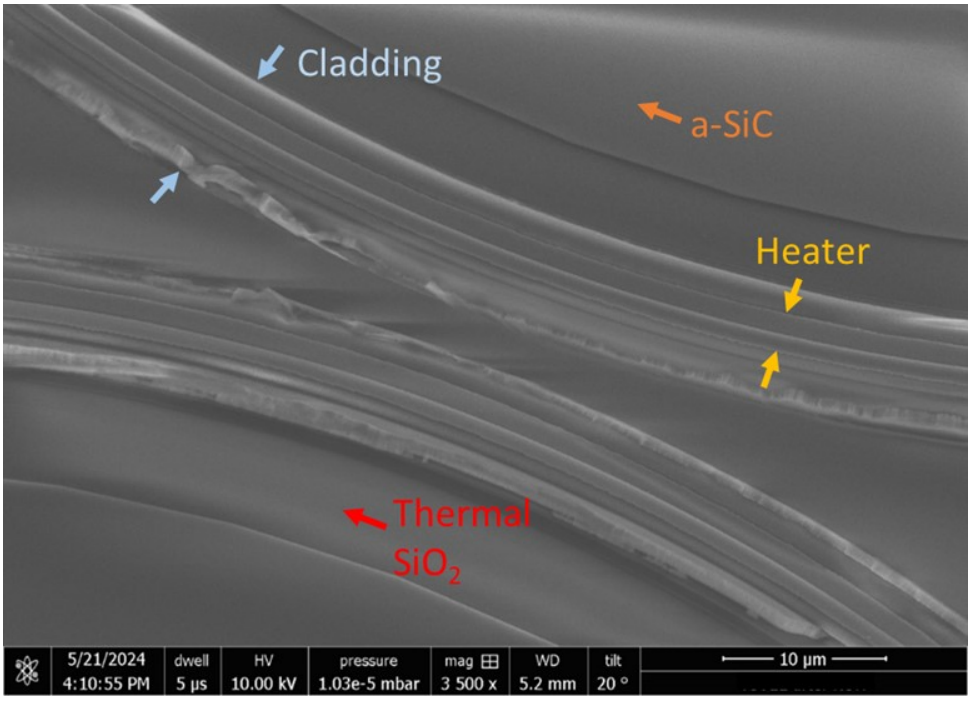

Figure S. B.23: Scanning Electron Microscope imaging of the resulting cladding after lift-off in the region between two optical ring resonators with the different elements delimited with arrows: cladding (blue), heaters, (yellow), a-SiC film (orange) and thermal silicon dioxide (red).

summarize the data for two different devices with similar ring resonator parameters as stated in the main manuscript and using ICPCVD cladding deposited at a temperature of 150°C and chamber pressure of 8 mTorr. Device 1 shows a deviation between measurements that could be related to device fabrication but also hysteresis. The second device presents a smaller variation and expected behaviour. Fig.S24b shows the wavelength shift as a function of the voltage for a device with PECVD cladding deposited at 300°C compared to the data in fig.S24a. In comparison, the measurement results using a PECVD silicon dioxide cladding show a smaller deviation between data points and no signs of hysteresis.

B9. Stability measurements of the optical setup

To assess the reproducibility of the measurements and determine the error given by the optical setup with the tunable laser, we performed four consecutive sweeps of temperature between 27°C and 31°C on a sample with ICPCVD silicon dioxide cladding deposited at 150°C and a chamber pressure of 10 mTorr. We extracted the thermal shifts with the respective errors in the fitting and determined the standard deviation of the measured resonant wavelength at a fixed stage temperature as summarized in table S12.

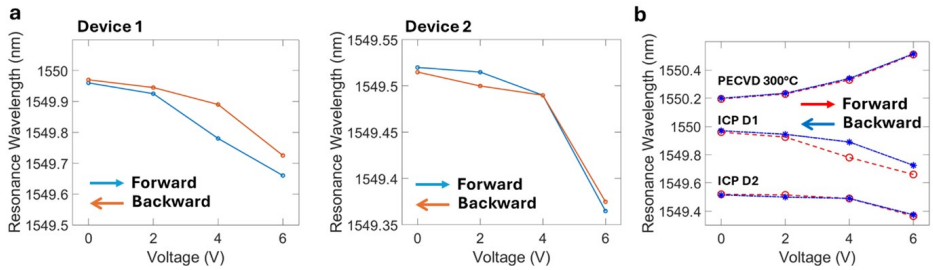

Figure S. B.24: Forward and backward voltage sweeps of a-SiC ring resonators made with silicon dioxide deposited with a) ICPCVD at 150°C and chamber pressure of 8 mTorr for two different devices and b) comparison with a cladding deposited with PECVD at 300°C.

Table S. B.12: Resonance wavelength position as a function of temperature for the four consecutive measurements together with the extracted slope and error.

	λ at 27°C (nm)	λ at 29°C (nm)	λ at 31°C (nm)	Slope (pm/°C)
Ramp 1	1549.271	1549.142	1548.887	-96 ± 18
Ramp 2	1549.276	1549.085	1548.887	-97 ± 1
Ramp 3	1549.235	1549.109	1548.902	-83 ± 12
Ramp 4	1549.319	1549.157	1548.935	-96 ± 9
Standard deviation	0.034	0.032	0.023	

ACKNOWLEDGEMENTS

A PhD in a scientific domain does not start at a certain moment but is the culmination of years of curiosity even before you start wondering why the sky is blue. The people around can fulfill the knowledge gaps or simply help understand yourself better. In any way, the person that presents the thesis is the result of all these interactions over many years that are transformed into tangible work and, in many cases, start the base of new technological advancements.

First and most important, I would like to thank my supervisor **Dr. Iman Esmaeil Zadeh** for trusting me in the complex task of building an entire new lab. The struggles that we experienced at the beginning, with empty optical tables and many boxes from Thorlabs are a good memory now rather than a stressful one. It is incredible to see all the ideas that we came up with are slowly becoming a reality. I can say with confidence that in another lab I would not have learnt as much as in this one. Most importantly, learnt from your attention to detail, the many creative ideas and making long supplementary files for the sake of completeness. I will always remember the funny moments trying to figure out a name for the company together with **Anna**. To **prof. Silvania F. Pereira** for all the invaluable comments for the articles to make the structure clearer and for the assistance with the optical setups and with the students we have had in our lab. Most important, for introducing me to your son whom I can call a friend. Thanks to **Jin Chang** for helping me at the beginning to get all the knowledge you have forged during four years. We were both starting a new adventure, yet you always had time to come to the lab and help me with the measurements and detectors. For all the help moving the setups between labs when we could not measure, the patience and the life advice. One day I will beat you at ping pong. To **Niels Los** for being a supportive colleague at the beginning of my lab journey, the "depressing" background music that I tried to change in the lab and helping me arrange all the optical setups in the lab. Also for the fun moments while bouldering and the nonsense fun we had. I hope that we can continue collaborating and that this time you deliver the measurements on time. To **Roald van der Kolk**, because you literally saved my thesis and helped to setup an entire research line in our group. If you would not have come to our office selling the ICPCVD tool and later helping us to optimize the recipe together with **Daniel van der Plaats**, my project would have failed. Thanks a lot for all the tips while bouldering, the many Schnitczels and for stopping me doing the acknowledgments section to go the bar. To **Naresh Sharma** for all the help during my second year of my PhD with the optical measurements that led to the first paper, for all the support with the experiments, optical setups and PIC designs. Quite a lot of effort during those stressful times but you provided invaluable insight. For all the conversations to see life and research with perspective. I am excited that you got a position in India and I am sure you will excel. Grateful to call you now a

collaborator. To **Hui Wang** for being my first former PhD colleague on which I could reflect about the journey. For showing me what hard work looks like and for all your help for many things in the lab that I started teaching you but you exceeded the knowledge. You are the star of the group and I am sure that you will excel in any new project that you start in life. To **Zizheng Li**, because you went from a student with no nanofabrication experience to being my mentor. For showing up everytime to check how I was doing, pushing me to work harder and having some laughs even when things were not working. For all the time we spent in the cleanroom, in the lab and outside of work. Thank you for making an outstanding contribution to my articles. I would not have achieved so much without your help and I hope we can push more exciting things in the future. To **Mischa**, the SNSPBoy, for your sarcasm, your hard work and your jokes, even when you frustrated me from time to time. I am sure you will do great in whatever group you go, but we will always be jealous. I guess I will inherit "your washers". We will miss your poster-winning SEM pictures and outstanding nanofabrication qualities but hoping that time makes you come back to our group. To **Cristina** for all the amazing work you did in our group in such a short time, for the moments of frustration because the setup was misaligned (very common in our group), for the conference trip and the fun we had in Strasbourg and for the lasting impression that you left in the group. I am sure you will achieve whatever you want after getting your PhD. Keep being updated in the field and trust yourself. To **Daniel Granados** for literally starting my career in Nanoscience. For your mentorship and patience even when I did not know what photoligraphy was or why we used photoresist. I am proud to say that much part of what I achieved was because of the trust you placed on me. I hope I am now in a position where I can return the favor. To **prof. Joydeep Dutta**, the person I consider my first mentor. For showing me how to deal with life, for taking care of me even when I was doing a mess in your lab, for encouraging me to pursue new professional experiences and for making sure that I always made the right choices. Thanks a lot for the help during my bad times. You could have forgiven me but you always made sure that everyone treated me right. Most importantly, for pushing people to achieve greater things, considering all students as part of your family and for putting in me the seeds of the entrepreneurial world. The success of your companies is an extension of your success as a human being and I am sure all of them will do well. To **Marijn**, because I already knew you from KTH and I was super happy and excited to meet you again in Delft. Thanks a lot during the time in Sweden and for recommending our group to your students. To **Jasper** for all the code you wrote to automatize the setups in the lab, the MATLAB GUIs and contributions to the design of the PICs. Also, for all the help you provided other people in the lab in a selfless way. I am sure you will do an amazing master's thesis and, hopefully, continue doing a PhD in our group. To our master students **Joey** and **Steijn** for building and improving a key optical setup in our lab with total independence and for the company in a moment where the lab was just starting. To **Luozhen Li** for building another great setup despite the struggles, characterizing many dots, and being a good colleague. I am sure you will do a great PhD in Geneva. To **Patrick**, because you tackled a problem with excellence, struggled to measure but delivered amazing data. For the many

moments where nothing was working and your setup was misaligned all the time but faced it with fun instead of frustration. To **Hugo** for all the effort that you placed not only during your thesis but afterwards. Thanks a lot for the help improving the setups, doing the measurements and all the time invested in the cleanroom. We made good progress. Let's see what your future awaits in Harvard. To **Jonas** for the perseverance despite all the problems with the imaging setup and for being a good colleague. I am sure the struggles will be worth the effort. Also to the other students, from bachelor or master, that came to our lab during these years and contributed to the overall performance of the group: **Tjeerd, Marc, Chunxiao, Jun, Ben, Thijs, Nikita, Giel, Bennie, Jos and more students from Haagse Hogeschool and TU Delft**. To **Roland** for bringing fun to a group filled with stressed PhD students and solving the many issues that appeared during the PhD, software and electrical related. For giving advice on not only professional issues but also personal ones and providing assistance selflessly. To **Thim** for literally building an entire optics lab and arranging everything related to the laser safety and chemicals. For the 3D printed stuff, the optical assemblies and general advice on how to build optical setups. For taking care of students and making sure that they succeed (without going blind). Nevertheless, the greatest part of the lab was **Thomas**. I would like to thank you for all the 3D printed stuff that we did not manage to specify the specs but you gave us a much better solution that we expected: the fiber holders, double-slit fiber v-groove holder, the PIC controller for the temperature stage, the adaptors for the many stages that we have in our setups, all the cryostat elements, the many designs for the different PCBs, the help to fix all the problems with the cryostat and piezo-stages and in general, all the input and knowledge you provided to the entire group. I am not lying when I say that you were key in all the papers of our group and I hope all the things I listed make you realize that way (even when you don't believe it). To **Lidija and Hannah** for all the help that you give to the group and sometimes goes unnoticed. For organizing everything and making sure that we, unorganized scientists, log our hours on time. Be patient with us, we are a mess. Not less important, thanks to the people in the Optics Cluster: **Shrouk, Behnoosh, Luuk, Anhubav, Sarika, Thomas van der Sijs, Thomas Kotte, Yanhui, Yifheng, Jila, Sven, Sander, Yifeng, GP, Jan (and your constant complains), Rein, Frank, Ding Ding, Dmytro and the others that joined the group.** And to the seniors: **Paul, Omar, Gao, Florian, Aurele and Jeff**.

To the people at Kavli Nanolab cleanroom and specially my first cleanroom mentor **Carel Herkeens**. Wherever you are, thanks a lot for bringing me along your duties in the cleanroom, teaching me the details, the talks about life, your trip stories, the exchanges in Spanish and your constant positivity about life. This thesis is also part yours and I believe that you would be proud to see my graduation. To **Anne**, for the many people that you have carried in your back to train and the different projects you provided input. I hope (but I am also sure) that you will have an amazing time in Barcelona. Be careful with staying there for too long ;D. To **Eugene** for sending me (literally) every Wednesday a morning message to book my suit and never losing patience. To **Charles** for the Spanish exchanges, lessons, small talk, and technical help in the cleanroom. For all the minus points I got in the tests

and the fun moments you created. But most important, for keeping all the tools up and running for our research. To **Ewan**, because "it could always be better" but you always managed to put a smile on people. For the many conversations about your football team and your many wins (and few losses). And for making sure that we had all the tools in the cleanroom to work properly and clean. And to the other staff **Anja, Arnold, Bryan, Hozanna, Lodi, Marinus, Claudia and many more.**.

To the people at KTH involved in my development during my master thesis, **Stephan Steinhauer, Val Zwiller, Theodor Staffas, Arthur Sutton, Samuel Gyger, Thomas Lettner**. To **Ali Elshaari and Jun Gao** for all the positive messages, providing stuff for us and making sure that we keep collaborations on-going. To **Adrian Iovan** for teaching me the basics in the cleanroom that led to all my knowledge developed in this thesis.

To **Matthijs**, because you were the first person I met in the Netherlands and we got along from the first time. For the bike trips that we did, even when my bike was terrible, for inviting me over your place to see football matches and the fun moments we also had with **Claudia**. To **Francesco** for the short trips, beers, watching football matches and most important, introducing me to bouldering. I expect to have more trips in the coming months. To **Ebrahim** for being the random gym bro, the amazing experience in the monkey zoo and for the trips with **George, Tanasis and Nasta**. I am very happy to have traveled with the four of you and for the dinners and drinks.

To **Albert**, because it is very difficult to put on text what it meant for me all the frienship in Stockholm, the long calls to check on me when I moved to the Netherlands and the fun trips we did. Thanks a lot for introducing me to your circle and for taking care of your "hermanito". I am quite happy that we supported each other during all our struggles and are slowly starting to see the light of the research journey. To **Josip**, because even when we did not interact a lot at the beginning, traveling together made me bond to a greater level. I had a lot of fun every time and it is very difficult to find people that adapt so easily. I am sure you will do amazing in you PhD and hoping for more trips together.

Mis cuatro años en Suecia y estos cuatro mas en Holanda no habrian sido posibles sin el apoyo constante de "los de la orquesta" de Madrid: **Javi, Alba, Bea, Irene, Alberto, Quique, Alicia y Adri.** Gracias por las quedadas a ultima hora antes de irme, viajes (que tenemos que hacer mas), scape-rooms, cervezas, cenas y regalos. A **Dani, Mario y Liza** por las tardes de juegos en el bar, cine y las muchas risas que nos hemos echado desde hace tantos años.

Pero quiza lo mas importante, dar las gracias a mi familia. **Tio Jose y Tia Pili** por enseñarme buenos restaurantes, los vaciles, los cocteles y los gin tonics. **Tia Luci**, por siempre mostrar curiosidad y no parar de hacer preguntas sobre lo que hacia, con entusiasmo y siempre apoyandome. A mi **prima Zoe** por todos los consejos que me diste cuando me fui a Suecia y durante mi tiempo en el doctorado. Gracias a mis primos **Victor** y **Werner** por todas las noches de conversaciones mientras jugabamos y las innumerables horas de risas sin sentido. A **Yu** por esas comidas que has organizado en Navidad con los primos, por sacarme de casa cuando vinisteis a Holanda y por empujarnos a salir de fiesta cuando nadie queria. A **Nuria** por

compartir tardes de juegos con los primos, comidas, cenas con la familia y por mantener a raya a mi primo ;D. A mi **abuelo Jose**, que se que estabas orgulloso de lo que estaba haciendo, y donde quieras que estes ahora, se que lo sigues estando. Gracias por contar tus experiencias de vida y por ser siempre tan positivo a pesar de las adversidades. Sin duda es algo que llevare conmigo siempre. A mi **abuela Sofia**, por tantos años que te he "hecho sufrir" pero que han merecido la pena. Gracias por preocuparte y por asegurarte que no lo pasara mal. Mi hermana **Paula**, que a pesar de que no hablamos mucho cuando estoy fuera, nos abrazamos con la misma fuerza cuando vuelvo. Gracias por los regalitos que siempre me han esperado a mi vuelta y por los sushis, cerves y cocteles con **Juan**. Lo valoro mucho mas de lo que he mostrado.

Mama y Papa: este trabajo es vuestro. Gracias por todas las conversaciones que hemos tenido a lo largo de los años que he estado fuera. Por darme perspectiva de la suerte que tengo a pesar de querer rendirme. Por venir cada vez que me encontraba mal y por las innumerables maletas llenas de tuppers y comida. Pero sobre todo por los pequeños gestos: los buenos dias, las buenas noches, las noticias diarias de España y los lanzamientos de cohetes. Gracias por compartir esos momentos.

Curriculum Vitæ

Bruno Lopez-Rodriguez

1996/04/16 Born in Madrid, Spain.

Education

2008–2014 High School Education
Colegio Montserrat-FUHEM (Madrid, Spain)

2014–2018 BSc in Physics (Applied Physics)
Complutense University of Madrid (Madrid, Spain)
2017–2018 Erasmus+ at KTH Royal Institute of Technology (Stockholm, Sweden)

2019–2021 MSc in Nanotechnology (Nanoelectronics/MEMS track)
KTH Royal Institute of Technology (Stockholm, Sweden)
Thesis Toward the detection of single photons in the mid-infrared (Supervisors: Stephan Steinhauer & Adrian Iovan
Examiner: Prof. Val Zwiller

2021–2025 PhD. Physics (Photonics)
Delft University of Technology (the Netherlands)
Thesis: High Performance Integrated Photonics with Amorphous Silicon Carbide
Promotor: Prof. Silvania F. Pereira & Dr. Iman Esmaeil Zadeh

Work Experience

2017– 2017 Research assistant (3 months)
IMDEA Nanoscience (Madrid, Spain)
Topic: Raman spectroscopy and PL of 2D Van-der-Waals materials

2018– 2020 Junior Research Engineer (2 years)
Kiselkarbid i Stockholm AB (Stockholm, Sweden)
CMP and surface characterization of SiC substrates

List of Publications

Journal papers

11. Tibiássy, A., J. Patrickson, C., Poirier, T., H. Edgar, J., **Lopez-Rodriguez, B.**, Esmaeil Zadeh, I., Ivády, V. & J. Luxmoore, I. (2025). *Coherent control of nuclear spins via the VB- center in hBN*. In preparation.

10. Erdogan, T., **Lopez-Rodriguez, B.**, Westerveld, W.J., Iskander-Rizk, S., Verbiest, G.J., Esmaeil Zadeh, I. & Steeneken, P.G. (2025). *Amorphous Silicon Carbide for Photonic Ultrasound Imaging*. In review process.

9. Z. Li, **Lopez-Rodriguez, B.**, Sharma, N., van der Kolk, R., Scholte, T., Smedes, H., Erdogan, T., Chang, J., Voncken, H., Gao, J., Elshaari, A.W., Gröblacher, S. & Esmaeil Zadeh, I. (2025). *Heterogeneous integration of silicon nitride and amorphous silicon carbide photonics*. In review process.

8. Gao, J., Chang, J., **Lopez-Rodriguez, B.**, Esmaeil Zadeh, I., Zwiller, V. & Elshaari, A.W. (2025). *From Pixels to Camera: Scaling Superconducting Nanowire Single-Photon Detectors for Imaging at the Quantum-Limit*. In review process.

7. **Lopez-Rodriguez, B.**, Sharma, N., Li, Z., van der Kolk, R., van der Boom, J., Scholte, T., Cahng, J., Gröblacher, S. & Esmaeil Zadeh, I. (2025). *Magic Silicon Dioxide for Widely Tunable Photonic Integrated Circuits*. ACS Photonics.

6. Li, Z., Sharma, N., **Lopez-Rodriguez, B.**, van der Kolk, R., Scholte, T., Voncken, H., van der Boom, J., Gröblacher, S. & Zadeh, I. E. (2025). *Heterogeneous integration of amorphous silicon carbide on thin film lithium niobate*. APL Photonics, 10(1).

5. Sharma, N., Li, Z., **Lopez-Rodriguez, B.**, Vrugt, J., van der Waal, S., Li, L., van der Kolk, R., Pool, P.J., Dalacu, D. & Zadeh, I. E. (2024). *Design and validation of a-SiC/SiN hybrid photonic platform for integrated quantum photonics*. Materials for Quantum Technology, 4(3), 035401.

4. Khoshmehr, M. T., Dashtabi, M. M., Nikbakht, H., **Rodriguez, B. L.**, Sharma, N., Zadeh, I. E., van Someren, B. & Akca, B. I. (2024). *Versatile hybrid optical waveguides in amorphous silicon carbide with enhanced functionality and performance*. Applied Physics Letters, 125(11).

3. Dashtabi, M. M., Khoshmehr, M. T., Nikbakht, H., **Rodriguez, B. L.**, Sharma, N., Zadeh, I. E., & Akca, B. I. (2024). *Real-Time Measurements of Photonic Microchips with Femtometer-Scale Spectral Precision and Ultrahigh Sensitivity*. Laser & Photonics Reviews, 18(8), 2301396.

2. Los, J. W., Sidorova, M., **Lopez-Rodriguez, B.**, Qualm, P., Chang, J., Steinhauer, S., Zwiller, V. & Zadeh, I. E. (2024). *High-performance photon number resolving detectors for 850–950 nm wavelength range*. APL Photonics, 9(6).

1. **Lopez-Rodriguez, B.**, Van Der Kolk, R., Aggarwal, S., Sharma, N., Li, Z., Van Der Plaats, D., Scholte, T., Chang, J., Gröblacher, S., Pereira, S.F. & Zadeh, I. E. (2023). *High-quality amorphous silicon carbide for hybrid photonic integration deposited at a low temperature.* ACS photonics, 10(10), 3748-3754.

CONFERENCE PAPER AND PRESENTATION

6. **Lopez-Rodriguez, B.**, Li, Z., van der Kolk, R., Sharma, N., Kolenov, D. & Zadeh, I. E. (2024, June). *Low temperature and high-quality amorphous silicon carbide photonics for hybrid photonic integration.* Invited paper pending for publication. SPIE Photonics West, San Francisco (California). (Not Presenter)

5. **Lopez-Rodriguez, B.**, Sharma, N., Li, Z., van der Kolk, R., van der Boom, J., Scholte, T., Chang, J., Pereira, S.F. & Zadeh, I. E. (2024, June). *Large, deterministic and tunable thermo-optic shift for all photonic platforms.* In Integrated Photonics Platforms III (Vol. 13012, pp. 112-114). SPIE Photonics, Strasbourg (France). (Presenter)

4. **Lopez-Rodriguez, B.**, van der Kolk, R., Aggarwal, S., Li, Z., Sharma, N., Scholte, T., Bhaskaran, H. & Zadeh, I. E. (2023, July). *Low-loss amorphous silicon carbide photonics and its heterogeneous integration with existing high performance active/passive platforms.* In Integrated Photonics Research, Silicon and Nanophotonics (pp. ITu2A-4). Optica Publishing Group. Busan, South Korea. (Not presenter)

3. Li, Z., **Lopez-Rodriguez, B.**, Sharma, N., & Esmaeil-Zadeh, I. (2023). *Heterogeneous interconnection of low-loss and dense material platforms using adiabatic tapering coupler.* In EPJ Web of Conferences (Vol. 287, p. 01014). EDP Sciences. (Not presenter)

2. **Lopez-Rodriguez, B.**, Chang, J., Los, J. W., Steinhauer, S., Zwiller, V., & Zadeh, I. E. (2022, May). *Ultra-high system detection efficiency superconducting nanowire single-photon detectors for quantum photonics and life sciences.* In CLEO US: Applications and Technology (pp. AW5P-2). San Jose, California. Optica Publishing Group. (Presenter)

1. Steinhauer, S., Gyger, S., **Rodriguez, B. L.**, Staffas, T., Lettner, T., Iovan, A., Elshaari, A. W. & Zwiller, V. (2021, April). *Superconducting single-photon detectors based on ultrathin NbTiN films.* In Quantum Optics and Photon Counting 2021 (Vol. 11771, p. 1177104). SPIE. Online. (Not presenter)

PATENTS

1. *Photonic Integrated Circuits for Nano-Lithography and Nano-Imaging: Leveraging Waveguides and Plasmonic Nanostructures*

   Naresh Sharma, **Bruno Lopez-Rodriguez**, Zizheng Li and Iman Esmaeil Zadeh.

   TU Delft reference: OCT-24-080. Dated: 25/10/2024

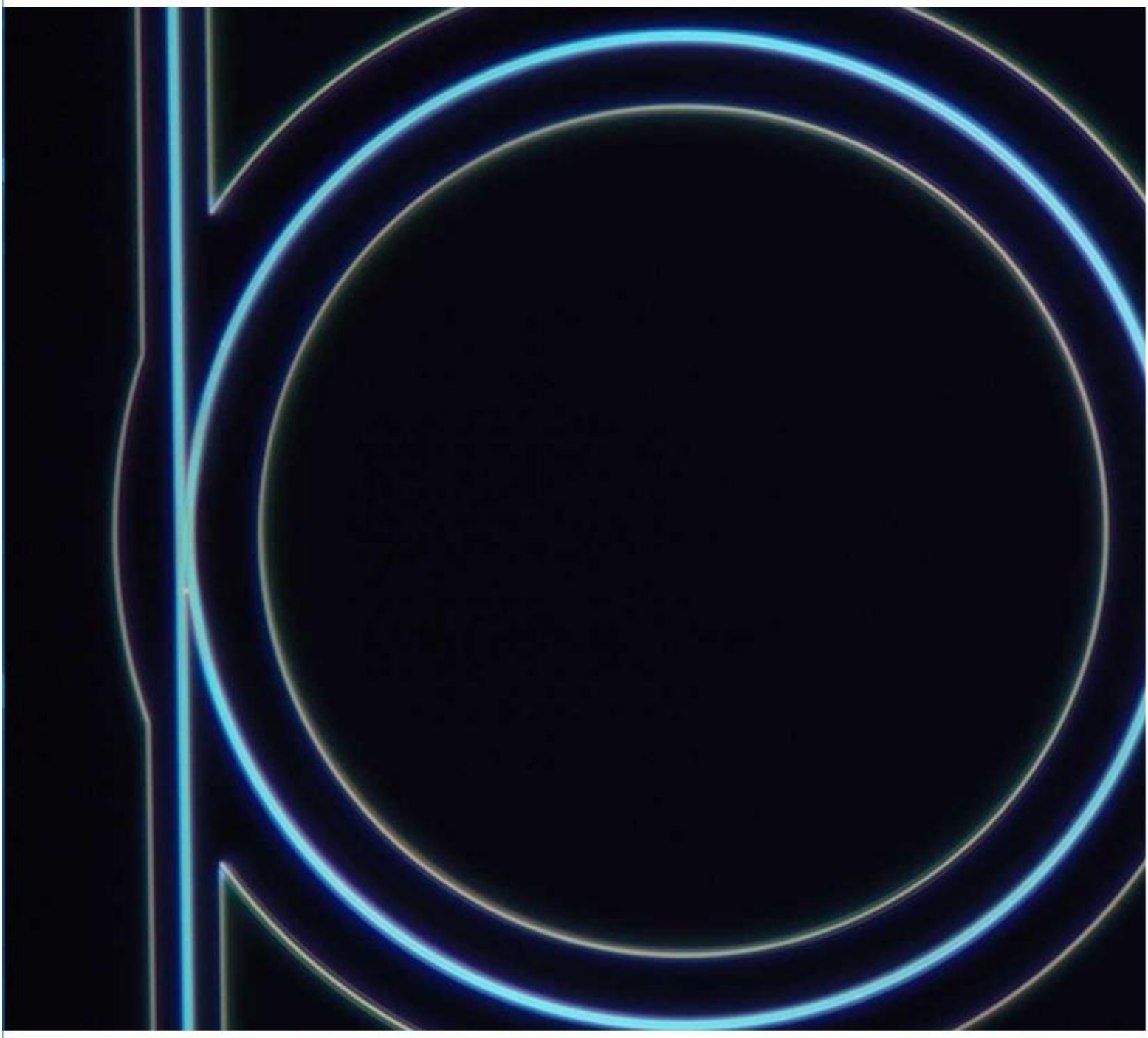

Dark-field optical microscopy image of a photonic ring resonator